ON THE REPRESENTATION OF SUBGRID-SCALE PHENOMENA AND ITS IMPACT ON CLOUD PROPERTIES AND CLIMATE

A Thesis
Presented to
The Academic Faculty

by

Ricardo Morales Betancourt

In Partial Fulfillment
of the Requirements for the Degree
Doctor of Philosophy in the
School of Earth and Atmospheric Science

Georgia Institute of Technology
December 2013

ON THE REPRESENTATION OF SUBGRID-SCALE PHENOMENA AND ITS IMPACT ON CLOUD PROPERTIES AND CLIMATE

Approved by:

Professor Athanasios Nenes, Advisor
School of Chemical & Biomolecular Engineering and School of Earth and Atmospheric Science
Georgia Institute of Technology

Professor Mike Bergin
School of Earth and Atmospheric Science
Georgia Institute of Technology

Professor Judy Curry
School of Earth and Atmospheric Science
Georgia Institute of Technology

Professor Yi Deng
School of Earth and Atmospheric Science
Georgia Institute of Technology

Professor Armisted Russell
School of Civil and Environmental Engineering
Georgia Institute of Technology

Date Approved: 13 November 2013

ACKNOWLEDGEMENTS

I would like to thank Prof. Athansios Nenes for all his support throughout the entire PhD. process, and for providing excellent opportunities to interact with other outstanding scientists both in NASA and PNNL. Special thanks to all the people whose work or support contributed to the completion of this thesis including current and former members of the Nenes Research Group.

TABLE OF CONTENTS

LIST OF TABLES

LIST OF FIGURES

SUMMARY

This work addresses a series of questions related to the problem of achieving reliable and physically consistent representations of aerosol-cloud interaction in global circulation models (GCM). The problem is approached by using in-situ data and modeling tools to develop and evaluate novel parameterization schemes for the process of aerosol activation for applications in GCM simulations. A variety of modeling tools are used in the process, ranging from detailed Lagrangian parcel model simulations of the condensational growth of droplets, to one-dimensional single column model with a aerosol and cloud microphysics, and finally GCM simulations performed with the Community Atmosphere Model (CAM).

Chapter 2 addresses an issue that has been generally overlooked in GCM cloud microphysical schemes, i.e., accounting for the impact of subgrid scale variability of in-cloud droplet number concentration. A simple approach is developed to demonstrate that neglecting the variability of in-cloud droplet number induces considerable biases in gridcell average values of microphysical processes, particularly, the autoconversion of cloud water to rain. The underlaying principle of this formulation is to exploit the relation between updraft velocity and droplet number to estimate SGS variability of N_d from that of updraft velocity. Chapter 3 shows the application of this idea in the Community Atmosphere Model, version 5.1 (CAM5.1), which is used to evaluate the global impacts of subgrid scale variability of droplet number. Important differences are found when these impacts are considered, particularly a reduction in simulated LWP and N_d.

In Chapter 4 in-cloud observations of droplet size distributions are used to evaluate the ability of an aerosol activation parameterization, which includes the effects

of entrainment and mixing, to reproduce in-situ observations of droplet number concentrations. A method to determine entrainment rates that effectively reproduce the reduction of N_d in shallow cumulus clouds is formulated. It was found that inclusion of entrainment and mixing in the computation of droplet number concentrations corrected a systematic bias when an adiabatic parameterization was used.

Chapter 5 describes a comprehensive comparison and evaluation of two widely used, physically-based activation parameterizations performed in the framework of CAM5.1. This is achieved by utilizing a new approach, in which the first order derivatives of the parameterization are evaluated using both analytical expressions and a numerical adjoint sensitivity. The adjoint sensitivities are then incorporated in the CAM framework to comprehensively investigate their response under the wide range of aerosol and dynamical conditions encountered in GCM simulations. As a result of this, the specific variables responsible for the observed differences in the physical response across parameterizations are encountered. Furthermore, pathways for the potential use of this type of analysis are outlined. The discrepancies observed in the sensitivity analysis of Chapter 5 allowed to identify areas were the performance of the parameterization could be improved improvement. Motivated by these findings, Chapter 6 presents a new formulation in the activation parameterization of *Nenes and Seinfeld* [2003], which the water uptake by the largest particles in the CCN population is described in a more consistent way, leading to more precise and accurate predictions of in-cloud supersaturation and droplet number.

Chapter 7 contains a brief account of my contribution to a group-wide effort in which detailed instrument modeling techniques combined with a large set of measurements of CCN activity world wide, lead to new constrains for the effective accommodation coefficient relevant for cloud formation. The CAM5.1 global circulation model was used to assess the global impact of potential kinetic limitations on cloud droplet formation. It was found that although N_d and the main radiation parameters are highly sensitive to the selected value of α_c, the estimates of aerosol indirect effects do not vary considerably.

Besides the main thesis work presented in Chapters 2 to 7, a study assessing the impact of different heterogenous ice nucleation parameterizations was performed using the McRAS microphysical scheme of the GEOS5 global circulation model and, and the results of such analysis are presented in Chapter 8. The impact of aerosols in the availability of IN is still a poorly understood and difficult to measure process, which is reflected in the 2 - 3 orders of magnitude discrepancies between the simulated crystal number predicted with the different parameterizations considered.

CHAPTER I

INTRODUCTION

The exponential increase in fossil fuel burning associated with human industrial activities since the industrial revolution has caused nearly a 2-fold increase in CO_2 concentration since the time prior to the industrial revolution. This modification of the atmospheric constituents at a molecular level, has had an important effect on the radiative balance of the Earth, believed to be of $2.5\mathrm{Wm}^{-2}$ when the contributions from N_2O, CH_4 and other gases are included [*Intergovernmental Panel on Climate Change*, 2007].

In addition to the increase in greenhouse gases concentration, human activities have affected the climate system in rather unexpected ways. Such is the case of the climatic impact of the large amounts of anthropogenic particulate matter injected in the atmosphere. The first of these *aerosol effects* on climate to be identified was their *direct effect* on shortwave scattering, i.e., the recognition that atmospheric aerosols, which reflect and absorb radiation, could thereby modify the planetary albedo and play an important role in the radiative budget of the Earth. Later on, attention was called towards the potential impact of atmospheric aerosols on clouds. In his foundational papers [*Twomey*, 1974, 1977], Twomey established the basis for the study of the so-called *indirect aerosol effects.* He identified the linking physical principles that controls the interactions between aerosols and clouds, i.e., "that pollution gives rise to whiter cloud, by increasing the droplet concentrations and thereby the optical thickness of clouds". A direct connection between pollution and the number of drops in a cloud and hence, the influence of aerosols on the optical thickness and reflectance of the clouds (cloud albedo) was then established.

The relationships linking atmospheric aerosol to clouds, and ultimately to cloud albedo, are each individually well-established. The relationship between cloud nuclei and cloud droplet number concentration (which inevitably affects optical thickness) has been confirmed experimentally (e.g., *Lu et al.* [2007, 2008]). The dominant role of cloud reflectance in determining the planetary albedo is well-recognized; it has been estimated that a 2 per cent reduction in the earth's input of solar energy would produce a catastrophic change in climate, implying that even small changes of either cloud cover or optical thickness, can have large impacts on the energy budget. Therefore, even though aerosol induced effects are small, they cannot be considered insignificant.

Twomey also anticipated the formidable challenge associated with estimating the magnitude of the albedo effect at a global scale: "Only the magnitude of the effect is uncertain, the greatest uncertainty being in the estimation of global nucleus production rates from relatively few measurements" [*Twomey*, 1974]. In fact, first estimates of aerosol indirect effect both from simple arguments [e.g., *Charlson et al.*, 1992] and GCM simulations [e.g., *Boucher and Lohmann*, 1995] produced a radiative forcing range of -0.5 to -1.5 Wm^{-2}, not too distant from current estimates [*Intergovernmental Panel on Climate Change*, 2007]. However, estimates performed with state-of-the-art climate models include many more physical processes, and incorporate valuable lessons learned from the increased availability of in-situ and sattelite observation of aerosols and clouds. Nevertheless, the magnitude of aerosol indirect effects continues to be uncertain, and it remains as one of the most difficult tasks for climate models. The heterogeneous nature of aerosols sources, the many natural and anthropogenic processes that generate them, their spatial heterogeneity, unknown optical properties, mixing state, their interaction with cloud systems, among others, largely contribute to this difficulty. Furthermore, prognostic cloud schemes for non-convective clouds (e.g, *Sundqvist* [1978]; *DelGenio et al.* [1996]), represent themselfes a formidable challenge for climate models, more over if these complex schems are to be interactive with aerosol modules.

Another complicating factor in this already complex picture is that the interaction of aerosols with clouds, is not of a static nature. The effect described by Twomey, i.e., albedo increase due to smaller droplets, is expected to occur to any cloud when formed under conditions of increased aerosol loading. However, the many other effects, termed *lifetime* effects, are of a dynamical nature, and therefore harder to represent. Attention has been called recently towards the many feedbacks that can can take place in this interaction, sometimes producing outcomes contrary to the conventional wisdom established by just simple reasoning (e.g., *Stevens and Feingold* [2009]; *Koren and Feingold* [2011]). It has also been noticed that aerosol-induced cloud *lifetime* effects might strongly depend on the cloud regime. For instance, it has been suggested that entrainment and mixing of cloudy and subsaturated air under polluted conditions might alter the cloud dynamics ultimately reducing its lifetime and cloud cover [e.g., *Jiang et al.*, 2006; *Small et al.*, 2009]. Similarly, it has been proposed that under certain conditions aerosol can invigorate rather than suppress precipitation [e.g., *Koren et al.*; *Li et al.*, 2011].

This brief (and necessarily incomplete) account of the study of aerosol indirect effects nevertheless conveys a sense of the difficulty of the problem. Firstly, the fact that atmospheric aerosols are produced by a wide range of different processes, with diverse sources. Aerosol optical properties vary considerably across aerosol species, from strongly absorbing aerosols to highly efficient scatterers of radiation. The mixing state, which determines the chemical composition of ambient aerosol, affects not only its optical properties, but their ability to act as cloud condensation nuclei.

These requirements to realistically represent aerosol indirect effects have pushed climate models to include new processes and to couple them in ways that were unthinkable just a few years ago. For instance, some of the first GCM estimates of aerosol indirect effects [*Boucher and Lohmann*, 1995], used a simple empirical expression to relate the mass of sulfate aerosol to the concentration of mass droplets. Although this approach captures the main idea, i.e., that more aerosol generate more numerous droplets, its quantitative accuracy is far from satisfactory and its physics are oversimplified. Current GCMs include many more natural and anthropogenic aerosol species, incorporating the changes in organic aerosol, black carbon, dust, and primary organic matter. Instead of prescribing the relationship between aerosol mass and droplet number, current GCMs use mechanistic parameterizations that account for the details of the activation process, i.e., they consider the impacts of aerosol size distribution, chemical composition, as well as the cloud-scale vertical velocity causing the formation of clouds. Since this processes involves some representation of the mass transfer process during condensation, not only thermodynamic relations are sufficient to describe it, but the kinetics of the process are also important. Substances that might reduce the rate of condensation might also impact aerosol activation.

The strong dependency that GCM estimates of aerosol indirect effect has on the specifics of the representation of aerosol-cloud interactions, and overall, in the parameterizations used to describe it, implies that in order to rely on the climate model results, this parameterizations must be physically based, and physically consistent. This thesis addresses some of these long-standing problems and proposes physically consistent answers to some of these issues.

When mechanistic representation of aerosol activation replaced the prescribed treatment, the updraft velocity became a crucial quantity determining the fraction of aerosols that activate in cloud droplets. However, the vertical motions responsible for aerosol activation are not resolved by GCMs. Cloud scale vertical motions in large-scale atmospheric models are uncertain, and will remain so since the relevant scales of the mechanism that produce such motions are still far smaller than the resolved scales. It is still important to have physically consistent treatment of vertical velocity.

Its impact on microphysics can help us represent these subgrid scale processes in a manner more consistent with our understanding of it.

The effects of entrainment and mixing on the droplet number concentration, which in observational studies and cloud resolving simulations have been shown to deeply impact liquid water path and cloud droplet numbers (therefore, its optical thickness), must somehow be taken into account. In this thesis we address this problem by using in-situ observation of cloud droplet size distribution to decide a method to apply a realistic parameterization of the activation process in climate models. Despite the growing evidence that aerosol can profoundly impact shallow and deep-convective clouds, these are typically not allowed to interact with the microphysics in climate models. Therefore, devising parameterization capable of representing aerosol-cloud interactions in convective clouds is an important step in achieving a more comprehensive treatment of indirect effects across cloud regimes.

It is also known that the representation of the activation step can be of crucial importance. The complexity of the parameterization schemes that are used in climate models, and the many inputs necessary to compute droplet numbers, has made it difficult to determine the physical consistency of its response to different perturbations. How can we understand their accuracy in responding to changes? how important are differences across parameterizations? We address this questions by performing a detailed sensitivity analysis of the most commonly used parameterizations. Newly developed tools, the adjoint sensitivities, are used to scrutinize the response of different parameterizations schemes to perturbations in the input variables. The physical consistency of those responses are evaluated by comparing them against detailed numerical simulations of the process. This analysis allowed us to understand the specific sources of discrepancies across parameterizations, and point in the direction of possible issues to be resolved. This analysis led to a new formulation of the activation parameterization of *Nenes and Seinfeld* [2003], and indicated the strong regional impact that small inaccuracies in the activation step can have on the simulated aerosol indirect effects.

The use of mechanistic representations of aerosol activation has opened the door for the representation of many, potentially important, chemical and kinetic effects affecting aerosol-cloud interactions. Since the mass transfer of water vapors determines to a large extent the cloud droplet number concentration, any kinetic limitations in this process have a large impact on simulations of droplet activation. The evaluation of these impacts in a climate model is also reported in this thesis.

CHAPTER II

CHARACTERISTIC UPDRAFTS FOR COMPUTING DISTRIBUTION-AVERAGED CLOUD DROPLET NUMBER, AND STRATOCUMULUS CLOUD PROPERTIES

2.1 Summary

A computationally-effective framework is presented that addresses the contribution of subgrid-scale vertical velocity variations in predictions of cloud droplet number concentration (CDNC) in large-scale models. Central to the framework is the concept of a "characteristic updraft velocity", $w^{\star}$, which yields CDNC value representative of integration over a probability density function (PDF) of updraft (i.e., positive vertical) velocity. Analytical formulations for $w^{\star}$ are developed for computation of average CDNC over a Gaussian PDF using the Twomey droplet parameterization. The analytical relationship also agrees with numerical integrations using a state-of-the-art droplet activation parameterization. For situations where the variabilities of vertical velocity and liquid water content can be decoupled, the concept of $w^{\star}$ is extended to the calculation of cloud properties and process rates that complements existing treatments for subgrid variability of liquid water content. It is shown that using the average updraft velocity, $\bar{w}$, (instead of $w^{\star}$) for calculations of N_d, r_e and A (a common practice in atmospheric models) can overestimate PDF-averaged N_d by 10%, underestimate r_e by $10\% - 15\%$, and significantly underpredict autoconversion rate

---

This chapter appears as reference *Morales and Nenes* [2010] between a factor of 2 to 10. The simple expressions of $w^\star$ presented here, can account for an important source of parameterization "tuning" in a physically-based manner.

2.2 Introduction

The direct microphysical link between aerosol and clouds is the process of activation *Köhler* [1936] during which a fraction of aerosol particles (termed Cloud Condensation Nuclei; CCN) experience unconstrained growth and form cloud droplets. Increases in precursor aerosol concentration can augment cloud droplet number concentration (CDNC), cloud albedo *Twomey* [1977] and lifetime *Albrecht* [1989], with important implications for climate. Even though droplet activation is well understood (e.g., *Pruppacher and Klett* [1997]; *Conant et al.* [2004]; *Fountoukis et al.* [2007]), its representation in global climate models (GCMs) is far from trivial. The current practice is to use "mechanistic parameterizations" (simplified but accurate relationships based on ascending cloud parcel theory) that provide CDNC as a function of the precursor aerosol and the parcel (cloud-base) updraft velocity w. Since the pioneering work of Twomey *Twomey* [1959], a number of prognostic, physically based parameterizations of aerosol activation have been developed and implemented in GCMs (e.g., *Abdul-Razzak et al.* [1998]; *Nenes and Seinfeld* [2003]; *Fountoukis and Nenes* [2005]; *Ming et al.* [2006]), some of which have been evaluated against observations of CDNC in stratocumulus and cumulus clouds (e.g., *Fountoukis et al.* [2007]; *Meskhidze et al.* [2005]).

CDNC predicted by mechanistic parameterizations is sensitive to updraft velocity; this poses a challenge in their implementation in GCMs, because cloud-scale updraft velocity is not resolved. This issue is currently addressed by either prescribing the updraft velocity from observations (e.g., *Sotiropoulou et al.* [2007]; *Pringle et al.* [2009]), or, diagnosing it from grid-resolved quantities, such as the grid-cell scale turbulent kinetic energy (K), $w^\star = \hat{w} + 0.7\sqrt{K}$ *Lohmann et al.* [1999], where $\hat{w}$ is the average (resolved) vertical velocity. CDNC is then computed from this "characteristic velocity" and applied to all cloud processes, mainly calculation of cloud optical depth, effective radius and autoconversion rate of cloud water to rain. These treatments for updraft velocity carry an important assumption: that a single updraft can be used to compute the "representative" CDNC for all cloud processes in the grid cell. In reality, a distribution of updrafts exist in each grid cell, each of which could be associated with its own droplet number. To account for this sub-grid variability, a probabilistic approach towards cloud properties can be used, in which each cloud forms in a grid cell with a characteristic updraft w occurring with a probability $P(w)$. Assuming that a continuous probability distribution function (PDF) can be used to describe $P(w)$, grid-averaged cloud properties can be derived. For example, the average droplet number in the grid cell is given by $\bar{N}_d = \int_0^\infty N_d(w)P(w)\mathrm{d}w / \int_0^\infty P(w)\mathrm{d}w$, where $N_d(w)$ denotes the CDNC that corresponds to w.

The probabilistic approach has been shown to successfully predict cloud-base CDNC in warm clouds in a number of field studies (e.g., *Conant et al.* [2004]; *Peng et al.* [2005]; *Meskhidze et al.* [2005]; *Fountoukis et al.* [2007]). Despite its conceptual strength, numerically integrating droplet number over a PDF is computationally expensive. *Peng et al.* [2005], *Meskhidze et al.* [2005] and *Fountoukis et al.* [2007] explored the possibility of replacing $\bar{N}_d$ with a single CDNC calculation at a "characteristic" updraft velocity, $w^\star$, so that $N_d(w^\star) = \bar{N}_d$. These studies found that, within measurement uncertainty, $w^\star$ is given by the PDF-average updraft velocity, $\bar{w} = \int_0^\infty wP(w)\mathrm{d}w / \int_0^\infty P(w)\mathrm{d}w$.

Although insightful, the aforementioned studies focused on a limited range of aerosol types and updraft velocity spectra, so the general applicability of $w^\star$ needs to be established. Furthermore, calculation of CDNC in climate models is not an endpoint, but rather an intermediate step for computing cloud processes (e.g., autoconversion rate) and radiative properties (e.g., effective radius) that impact the simulated hydrological cycle and climate. Given that cloud properties depend nonlinearly on N_d and the cloud liquid water content, q_c, correctly accounting for their subgrid variability is crucial for unbiased representation of clouds in large-scale models. GCM schemes have been developed to account for subgrid-scale variability in q_c (e.g., *Morrison and Gettelman* [2008]), as using grid-scale values of q_c were known to induce biases in nonlinear cloud processes (e.g., *Pincus and Klein* [2000]). Climate models however do not account for the subgrid-scale (SGS) variability of N_d. This is an especially important oversight for indirect effect studies, since the aerosol-N_d link (and its subgrid variability) is at the heart of the aerosol-cloud-climate interactions.

This study aims to provide a computationally-effective framework to address the issue of PDF-averaging of CDNC that arise from subgrid scale variations in vertical velocity. The optimum characteristic velocity, $w^\star$, is determined for computation of average droplet number concentration over a Gaussian PDF of updraft velocity. For situations where the joint distribution of q_c and w can be decoupled, we develop expressions of characteristic velocity that accounts for sub-grid variability of CDNC in processes such as autoconversion rate and effective radius, that complement existing treatments for subgrid variability of liquid water content.

2.3 Probability Distributions

2.3.1 The problem of joint PDFs between q_c and w.

Cloud microphysical processes depend on several quantities (the two most important being cloud liquid water content, q_c and CDNC, N_d) that exhibit large sub-grid scale (SGS) variations. The functional form of the PDFs that express their SGS variability has been the subject of intense study (e.g., *Pincus and Klein* [2000]; *Golaz et al.* [2002]; *Morrison and Gettelman* [2008]; *Cheng and Xue* [2009]; *Zhu and Zuidema* [2009]). The problem of determining these distributions is usually approached by prescribing a joint PDF of the variables under consideration. Although a number of PDF functions have been proposed with a wide range of complexity, a universally-accepted form remains elusive. The parameters of the PDFs are either prescribed (obtained by fits to observational data or cloud-resolving models), diagnosed from resolved quantities in the GCM simulation (e.g., turbulent kinetic energy) or determined from prognostic equations that describe the higher-order moments of the distribution (e.g., *Golaz et al.* [2002]).

The joint-distribution approach can be described as follows. Consider a cloud microphysical property or process rate (e.g., effective radius, CDNC, autoconversion rate), $F(q_c, N_d)$, that depends on q_c and N_d. If the joint probability distribution $\mathcal{P}(q_c, N_d)$ is known, the average property, $\bar{F}$, is given by

$$\bar{F} = \iint \mathcal{P}(q_c, N_d) F(q_c, N_d) \mathrm{d}q_c \, \mathrm{d}N_d \tag{1}$$

Using mean values of N_d ($\bar{N_d}$) and q_c ($\bar{q_c}$) to estimate $\bar{F}$ is equivalent to neglecting their SGS variability, as it implies that $\mathcal{P}(q_c, N_d) \simeq \delta(q_c - \bar{q_c})\delta(N_d - \bar{N_d})$, where δ is the well-known Dirac function. This approach induces biases in calculations of $\bar{F}$, because in general $\bar{F} \neq F(\bar{q_c}, \bar{N_d})$.

Some GCMs cloud schemes (e.g., *Pincus and Klein* [2000]; *Morrison and Gettelman* [2008]) partially overcome the subgrid variability problem by accounting for variations in q_c. This is equivalent to assuming $\mathcal{P}(q_c, N_d) = Q(q_c)\delta(N_d - N_0)$, where $Q(q_c)$ is a PDF describing the SGS variability of liquid water content (e.g., a gamma distribution; *Morrison and Gettelman* [2008]). N_0 is a "characteristic" value of droplet number in the grid, typically assumed to correspond to $N_d(\bar{w})$ or prescribed to a fixed value (e.g., *DelGenio et al.* [1996]). *Morrison and Gettelman* [2008] proposed using a characteristic $q_c^\star$, such that the integration over $Q(q_c)$ is equivalent to evaluating F at $q_c^\star$, i.e.,

$$\overline{F} = F(q_c^\star, N_0) = F_0 N_0^x \int q_c^y Q(q_c) \mathrm{d}q_c \tag{2}$$

where we have assumed that $F(q_c, N_d)$ has a power law dependence on N_d and q_c, i.e., $F(q_c, N_d) = F_0 N_d^x q_c^y$, where F_0, x, y are coefficients. From Equation 2, $q_c^\star = \left[\int q_c^y Q(q_c) \mathrm{d}q_c\right]^{1/y}$

This kind of approach, although in the right direction of addressing the issue of SGS variability, still neglects the variability of cloud properties on N_d hence will induce biases in the computation of $\bar{F}$. This is particularly important for indirect effect assessments, given that a key sensitivity (i.e., of cloud processes to changes in N_d) is not resolved correctly.

2.3.2 Joint PDF for stratocumulus in well-mixed boundary layers

Despite many conceptual advantages of the joint PDF approach, its main limitation is the need to predict the distribution moments (*Pincus and Klein* [2000]), often from a set of prognostic equations that need to be solved at much higher temporal resolution that of the parent model (*Golaz et al.* [2002]; *Zhu and Zuidema* [2009]). As a result, explicit dynamic PDF resolution requires significant computational resources. However, in-situ observations and re-analysis of large-eddy simulations of clouds suggest that simpler, prescribed forms of PDFs may capture much of the q_c-w variability for specific cloud regimes.

For cumulus clouds, q_c and w are correlated so that the functional form of the joint PDF is complex (e.g., *Golaz et al.* [2002]; *Guo et al.* [2008]). Stratocumulus clouds in well-mixed boundary layers however exhibit a single mode updraft velocity PDF with little skewness that often be described with a Gaussian distribution (*Golaz et al.* [2002]; *Kogan* [2005]; *Guo et al.* [2008]). Another important characteristic is that the distribution of updrafts tends to be weakly-coupled with the distribution of thermodynamic variables (e.g., q_c or equivalent potential temperature θ_l) (e.g., *Curry* [1985]). Because of this, we can assume that the distribution of q_c is (to first order) decoupled from the distribution of w, or, $\mathcal{P}(q_c, w) = Q(q_c)P(w)$, where $Q(q_c)$, $P(w)$

are the respective PDFs of q_c and w. It is interesting to note that each of the Gaussian distributions in the double-Gaussian cloud scheme proposed in *Golaz et al.* [2002] also exhibit a similar decoupling between dynamic and thermodynamic variables within each Gaussian.

If $P(w)$ is known, the one-to-one correspondence between w and N_d (e.g., provided by cloud drop parameterizations) suggests that $P(w)$ can be remapped onto the N_d domain to provide a PDF of N_d, $p(N_d)$. This means that the decoupling between q_c, w variabilities implies a decoupling between q_c, N_d variabilities, hence $\mathcal{P}(q_c, N_d) = Q(q_c)p(N_d)$. Accounting for SGS variability in cloud processes can therefore be addressed as follows. Assuming $F = F_0 N_d^x q_c^y$, and $\mathcal{P}(q_c, N_d) = Q(q_c)p(N_d)$, Equation 1 becomes

$$\bar{F} = F_0 \int N_d^x p(N_d) \mathrm{d}N_d \int q_c^y Q(q_x) \mathrm{d}q \tag{3}$$

Equation 3 allows the definition of characteristic values of q_c and N_d such that $q_c^\star = \left[\int q_c^y Q(q_c)\mathrm{d}q_c\right]^{1/y}$, $N_d^\star = \left[\int N_d^x p(N_d)\mathrm{d}N_d\right]^{1/x}$. Equation 3 then becomes

$$\bar{F} = F(q_c^\star, N_d^\star) = F_0 q_c^{\star y} N_d^{\star x} \tag{4}$$

Existing approaches for SGS variability of q_c can be used to compute $q_c^\star$ (e.g., *Morrison and Gettelman* [2008]). $N_d^\star$ can then be related to a characteristic velocity, $w^\star$, so that an application of a cloud droplet parameterization can give $N_d^\star = N_d(w^\star)$. The value of $w^\star$ will depend on the cloud process parameterization, and is detailed in sections 3,4. If $w^\star$ is known however, application of Equation 4 constitutes a *substantial* acceleration of calculating PDF-averaged properties, as a numerical integration over the joint PDF (Equation 1) is replaced with a single function evaluation (Equation 4).

2.3.3 PDFs for calculating CDNC

PDF-averaged CDNC is an important quantity useful for evaluating GCM simulations. Its calculation, compared to other cloud microphysical properties and processes (e.g., autoconversion and effective radius) is also much simpler, given that it requires only knowledge of the PDF of vertical velocity $P(w)$ (it also depends on aerosol properties, but these are assumed known). For the purpose of this work, we will assume that $P(w)$ follows a Gaussian distribution, $P(w) = (\sqrt{2\pi}\sigma)^{-1} \exp\{-(w - \hat{w})^2/(2\sigma^2)\}$, where $\hat{w}$ is the mean (resolved) vertical velocity, and σ is the standard deviation of the velocity PDF. Given the scale of GCM grid cells ($\sim 100km$), $\hat{w}$ is very small compared to the magnitude of fluctuations, so that $P(w) \approx (\sqrt{2\pi}\sigma)^{-1} \exp\{-w^2/(2\sigma^2)\}$. In boundary layers, velocity fluctuations are mainly associated with turbulence, so that the turbulent kinetic energy, K, scales with the sub-grid velocity fluctuations, $K \sim \sigma^2$. Therefore, from the grid-scale resolved K, a Gaussian PDF can be diagnosed (with $\sigma \sim K^{1/2}$) that is consistent with the large-scale simulation and suitable for computing velocity averaged cloud processes and properties. Outside of the boundary layer, a distribution can still be diagnosed from other sources of variability (such as gravity wave breaking) but is outside of the scope of this study. For a Gaussian distribution with $\hat{w} \approx 0$, the average updraft velocity, $\bar{w}$, (i.e., the average over the positive part of the vertical velocity distribution) is given by $\bar{w} = (2/\pi)^{1/2}\sigma \approx 0.79\sigma$ *Fountoukis et al.* [2007].

2.3.4 Impact of CDNC variability on cloud processes and properties

Let $F(w)$ denote any cloud microphysical property that depends on the updraft velocity w. F averaged over the positive vertical velocities, $\bar{F}$, is then given by

$$\bar{F} = \int_0^\infty F(w)P(w)\mathrm{d}w \Big/ \int_0^\infty P(w)\mathrm{d}w \tag{5}$$

Often, $F(w)$ can be approximated with a power law, $F(w) = aw^b$, where a, b are coefficients that do not depend on w. In this case, $\bar{F}$ for a Gaussian $P(w)$ is computed from Equation 5,

$$\bar{F} = \frac{a}{\sqrt{\pi}} 2^{b/2} \sigma^b \Gamma\left(\frac{b+1}{2}\right) \tag{6}$$

where $\Gamma(z) \equiv \int_0^\infty t^{z-1} e^{-t} \mathrm{d}t$ is the Gamma function.

The only natural velocity scale present in a Gaussian distribution $P(w)$ is σ; a non-dimensional velocity, λ, can therefore be defined as $\lambda \equiv w/\sigma$. $\bar{F}$ (Equation 6) normalized with $F(\lambda\sigma) = a\lambda^b\sigma^b$ is given by

$$\frac{\bar{F}}{F(\lambda\sigma)} = \frac{2^{b/2}}{\sqrt{\pi}} \lambda^{-b} \Gamma\left(\frac{b+1}{2}\right) \tag{7}$$

which only depends on b and λ. Equation 7 can be used to determine the characteristic non-dimensional velocity, $\lambda^\star$, for which $F(\lambda^\star\sigma) = \bar{F}$,

$$\lambda^\star = 2^{1/2} \pi^{-1/2b} \Gamma\left(\frac{b+1}{2}\right)^{1/b} \tag{8}$$

which depends solely on b.

2.4 Application of PDF to calculation of droplet number

The extensively used *Twomey* [1959] parameterization was developed assuming a power law expression for the CCN spectrum (i.e., the number of CCN at supersaturation s), given by,

$$N_{CCN}(s) = c(s/s_0)^k \tag{9}$$

where c is the concentration of CCN at supersaturation s_0. From this expression, it can be shown that N_d has a power law dependence on updraft velocity, $N_d(w) = f(c,k)w^{3k/(2k+4)}$, where

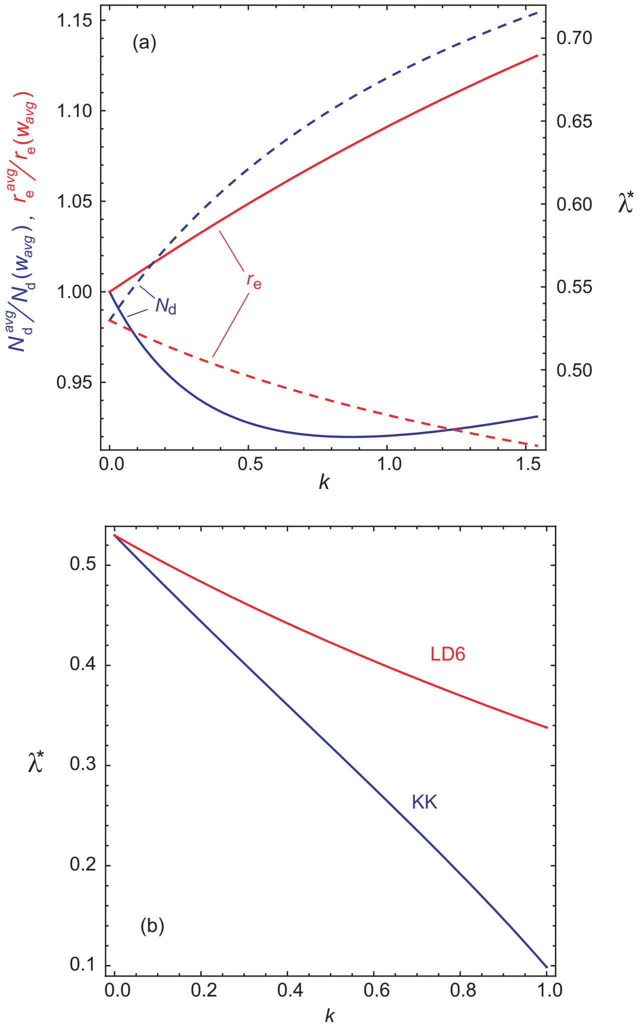

Figure 1: (a) $\bar{N}_d/N_d(\bar{w})$ (solid blue line) and $\bar{r_e}/r_e(\bar{w})$ (solid red line) and respective characteristic non-dimensional velocity $\lambda^\star = w^\star/\sigma$ (dashed lines) as a function of the CCN spectrum steepness parameter k. (b) $\lambda^\star$ for KK (blue) and LD6 (red) parameterization as a function of the parameter k. CDNC is computed from *Twomey* [1959] parameterization.

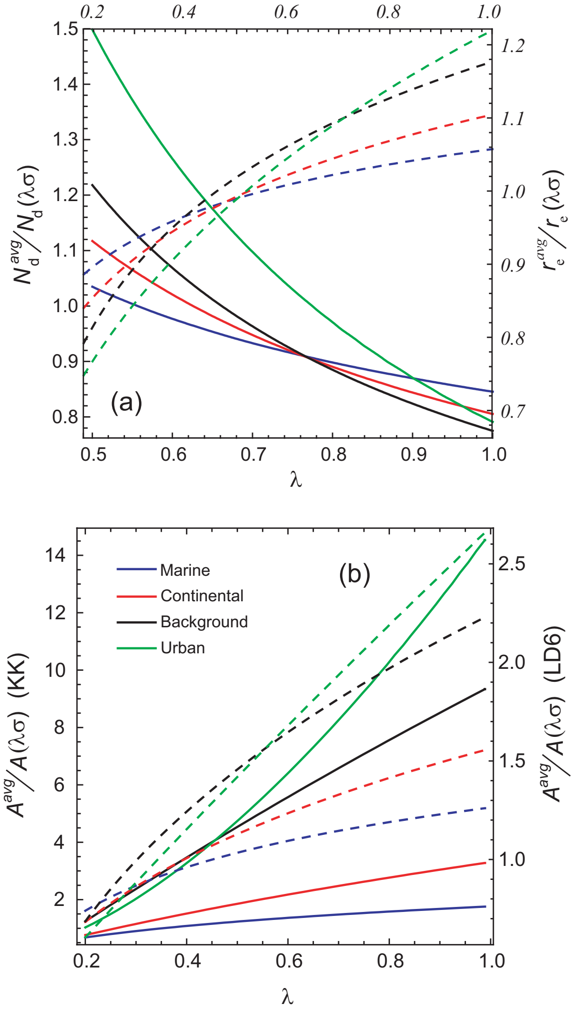

Figure 2: (a) $\bar{N}_d/N_d(\lambda\sigma)$ (solid lines) and $\bar{r_e}/r_e(\lambda\sigma)$ (dashed lines) computed with the *Fountoukis and Nenes* [2005] parameterization as a function of λ. (b) $\bar{A}/A(\lambda\sigma)$ using N_d computed with *Fountoukis and Nenes* [2005], as a function of λ for the four types of aerosol considered. Solid lines correspond to the *Khairoutdinov and Kogan* [2000] (KK) parameterization, and, dashed lines show calculations for *Liu and Daum* [2004] (LD6) expression.

$$f(c,k) = (cs_0)^{2/(k+2)} \left[\frac{4\rho_a}{\gamma\pi\rho_w} \left(\frac{\alpha}{G}\right)^{3/2} \frac{1}{k\mathrm{B}(3/2,k/2)} \right]^{k/(k+2)} \tag{10}$$

and $\mathrm{B}(a,b) = \Gamma(a)\Gamma(b)/\Gamma(a+b)$ is the Euler beta function. Using this simple parameterization, the PDF-averaged droplet number $\bar{N_d}$ over the CDNC computed at $w = \lambda\sigma$, $N_d(\lambda\sigma)$, is given by setting b equal to $3k/(2k+4)$ in Equation 7,

$$\frac{\bar{N_d}}{N_d(\lambda\sigma)} = \frac{1}{\sqrt{\pi}} 2^{\frac{3k}{4k+8}} \lambda^{-\frac{3k}{2k+4}} \Gamma\left(\frac{5k+4}{4k+8}\right) \tag{11}$$

The characteristic updraft, $\lambda^\star\sigma$, so that $N_d(\lambda^\star\sigma) = \bar{N_d}$, is given by Equation 8

$$\lambda^\star = 2^{1/2}\pi^{\frac{k+2}{3k}} \Gamma\left(\frac{5k+4}{4k+8}\right)^{\frac{2k+4}{3k}} \tag{12}$$

Therefore the characteristic updraft $w^\star = \lambda^\star\sigma$ is solely determined by the steepness of the CCN spectrum (i.e, k) and σ. Over the atmospherically relevant values of k (0.1-1.5) [*Twomey and Wojciechowski*, 1968], $\lambda^\star$ ranges between 0.55 for $k = 0.1$ (clean conditions) and 0.74 for $k = 1.5$ (polluted). An average value for $\lambda^\star$, $\lambda^\star_{avg} = 0.65$, is 17% lower than the average updraft ($\lambda = 0.79$). $\bar{N_d}/N_d(\bar{w})$ is numerically close to unity, ranging between 0.92 and 1 (Figure 1a). All together, this implies that using $\bar{w}$ to estimate average droplet number would tend to overestimate $\bar{N_d}$ by at most 10%.

More sophisticated activation parameterizations also exhibit a power-law like dependence on w, hence we expect $\lambda^\star$ to be closely approximated by Equation 12. To assess this, we use the *Fountoukis and Nenes* [2005] parameterization, which is based on the framework of an air parcel rising at constant speed. Droplets are classified by the proximity to their critical diameter ("population splitting"), allowing calculation of the cloud maximum supersaturation from the numerical solution of the balance of water vapor availability from cooling and depletion from the condensational growth. The CDNC is then equal to the CCN that activate at the cloud maximum supersaturation. The parameterization allows for the accurate treatment of complex aerosol size

Table 1: Dry aerosol size distributions used in this study (*Whitby* [1978]). D_{pgi}, σ_{gi}, N_i is the geometric mean diameter (μm), spectral width, and number concentration (cm^{-3}), respectively, of mode "i".

Aerosol Type	D_{pg1}	σ_{g1}	N_1	D_{pg2}	σ_{g2}	N_2	D_{pg3}	σ_{g3}	N_3
Marine	0.010	1.6	340	0.070	2.01	60	0.620	2.70	3.1
Continental	0.016	1.6	1000	0.068	2.10	800	0.920	2.20	0.7
Background	0.016	1.7	6400	0.076	2.01	2300	1.020	2.16	3.2
Urban	0.014	1.8	106000	0.054	2.16	32000	0.860	2.21	5.4

distribution, chemical composition and droplet growth kinetics. It has been expanded to treat entrainment effects on CDNC (*Barahona and Nenes* [2007]), adsorption activation (*Kumar et al.* [2009]) and Giant CCN (*Barahona et al.* [2010a]). The accuracy of the parameterization has been evaluated with detailed numerical simulations *Nenes and Seinfeld* [2003]; *Fountoukis and Nenes* [2005]; *Barahona and Nenes* [2007]; *Barahona et al.* [2010a] and in-situ data for cumuliform and stratiform clouds of marine and continental origin *Meskhidze et al.* [2005]; *Fountoukis et al.* [2007].

The *Fountoukis and Nenes* [2005] parameterization provides a numerical relation $N_d(w)$ rather than a explicit functional form; PDF averaging is therefore done numerically. Calculations are carried out for ammonium sulfate aerosol with size distribution characteristics of marine, clean continental, average background and urban environments given by *Whitby* [1978] (listed in Table 1). PDF averages of N_d are computed for a set of Gaussian vertical velocity distributions with $\hat{w} = 0$, and σ ranging from 0.05 to 0.75 ms^{-1}. Since the $N_d(w)$ relation provided by this parameterization does not follow a strict power law dependence, $\lambda^\star$ calculated with these parameterization will exhibit some dependence on the parameter σ defining the PDF. Therefore, $\bar{N_d}$ calculated with *Fountoukis and Nenes* [2005] is averaged over the range of σ under consideration in this study.

Figure 2a presents the resulting $\bar{N_d}/N_d(\lambda\sigma)$ (solid lines) as a function of λ for all aerosol considered. When $\bar{w}$ is used (i.e., $\lambda = 0.79$), $\bar{N_d}$ is overestimated on average by 9.8%. The average $\lambda^\star$ for all aerosol distributions and σ considered is $\lambda \approx 0.676$ (close to the Twomey value of 0.65), which if used for calculating N_d, overestimates $\bar{N_d}$ by as little as 0.03%. Using the characteristic λ derived from the *Twomey* [1959] parameterization ($\lambda = 0.65$) gives N_d that approximates $\bar{N_d}$ to within 2.2%.

2.5 CDNC variability effects on Autoconversion rate and Effective radius

2.5.1 Autoconversion rate

Assuming that the joint distribution of q_c and w can be expressed as in Equation 3, characteristic values of q_c and N_d (w) can be defined that allow evaluation of cloud processes and properties (with a single function evaluation) that are representative of their PDF-averaged values (Equation 4). *Morrison and Gettelman* [2008] have already determined $q_c^\star$ assuming that $Q(q_c)$ follow a gamma distribution. Here we determine $w^\star$ that can be used for computing $N_d^\star$ in Equation 4.

Most autoconversion parameterizations sensitive to CDNC exhibit a power-law dependence on N_d; $w^\star$ thus would depend on how autoconversion rate, A, scales with N_d. This is demonstrated with two autoconversion parameterizations, by *Khairoutdinov and Kogan* [2000] (denoted KK hereafter), where $A \sim N_d^{-1.79}$, and, the R_6 formulation of *Liu and Daum* [2004] (denoted here LD6), where $A \sim N_d^{-1}$. Application of Equation 7 to each parameterization provides the updraft-average autoconversion rate.

For KK, $A = 1350 q_c^{2.47} N_d^{-9/5}$, with q_c being the cloud water mixing ratio. Introducing the *Twomey* [1959] relation for $N_d(w)$,

$$A(q_c, w) = 1350 q_c^{2.47} f(c,k)^{-9/5} w^{-27k/(10k+20)} \tag{13}$$

Thus, if $A(w, q_c)$ is evaluated at a characteristic $q_c^\star$ that account for the integration over the PDF of q_c (Equation 4), then autoconversion follows a power law dependence on w; the formalism developed in section 2.3.4 can then be applied to calculate the PDF-average A, where $a = 1350(q_c^\star)^{2.47} f(c,k)^{-9/5}$ and $b = -27k/(10k+20)$.

For LD6, $A = 3\rho_a^3 \kappa_2 \beta_6^6 q_c^3 N_d^{-1} H(R_6 - R_{6c})/(4\pi\rho_w)$, where $\kappa_2 = 1.0 \times 10^{17} m^{-3} s^{-1}$, H is the Heaviside function, R_6 is the 6th moment of the size distribution, R_{6c} is the "critical" threshold radius, and β_6 is a non-dimensional parameter depending on the spectral shape of the cloud droplet size distribution *Liu and Daum* [2004]. LD6 is a product of two functions: a collection function that gives the total coalescence rate, and, a threshold function that expresses the fraction of coalescence attributed to autoconversion. LD6 implement the Heaviside threshold function, which may introduce biases (e.g., *Whitby* [2005]; *Liu and Daum* [2005]). *Liu et al.* [2006a] addressed this issue by developing a kinetically-defined threshold function of the form $T(q_c, N_d) = 1 - exp\left[-(1.03 \times 10^{16} N_d^{-3/2} q_c^2)^\mu\right]$ where $\mu \sim 0.36$ (e.g., *Hsieh et al.* [2009a]) is an empirical parameter. Autoconversion rates using this threshold function exhibits two regimes: i) one where the argument in the exponential of $T(q_c, N_d)$ is large, so that $T(q_c, N_d) \simeq 1$, and A scales with N_d^{-1}, and, ii) one where the argument in the exponential of $T(q_c, N_d)$ is small, so that upon expansion yields $T(q_c, N_d) \simeq 1 - \left[1 - (1.03 \times 10^{16} N_d^{-3/2} q_c^2)^\mu\right] = (1.03 \times 10^{16} N_d^{-3/2} q_c^2)^\mu$. Therefore, A scales with $q_c^{3+2\mu} N_d^{-(1+3\mu/2)}$, which for $\mu \sim 0.36$ carries a strong $N_d^{-1.54}$ dependence, close that seen for the KK parameterization. Given this, we carry out calculations only with the N_d^{-1} dependence, to determine an "upper" limit in $w^\star$ (the lower given by KK), knowing that it lies somewhere between the two limits defined by the parameterizations.

After introducing the Twomey relation for $N_d(w)$ into LD6,

$$A(q_c, w) = \frac{3\kappa_2 \beta_6^6 \rho_a^3}{4\pi\rho_w f(c,k)} H(R_6 - R_{6c}) q_c^3 w^{-3k/(2k+4)} \tag{14}$$

hence A follows a power-law dependence on updraft with $a = 3\kappa_2 \beta_6^6 \rho_a^3 q_c^3 H(R_6 - R_{6c})/\{4\pi\rho_w f(c,k)\}$ and $b = -3k/(2k+4)$.

Equation 8 can then be applied to $A(q^\star, w)$, and from Equations 13 and 14 determine the characteristic updraft $\lambda^\star$, for autoconversion (i.e, $\lambda^\star$ for which $A(q_c^\star, \lambda^\star\sigma) = \bar{A}$). This is presented in Figure 1b, which shows $\lambda^\star$ for KK (blue line) and LD6 (red line) as a function of k. Averaging $\lambda^\star$ over the atmospheric range of k gives $\lambda^\star_{avg} = 0.33$ for KK and $\lambda^\star_{avg} = 0.44$ for LD6. These characteristic λ values are about 50% smaller than the characteristic updraft for estimating $\bar{N}_d$.

$\bar{A}/A(q_c^\star, \lambda\sigma)$ is also numerically computed with respect to λ using the *Fountoukis and Nenes* [2005] parameterization (for the same aerosol types and σ as of section 2.4) and presented in Figure 2b. $\lambda^\star$ ranges between 0.2 and 0.35 for KK (with $\lambda^\star_{avg} = 0.26$ for the aerosol considered), and, from 0.3 to 0.45 for LD6 (with $\lambda^\star_{avg} = 0.37$). These values are on average between 33% to 45% of the average updraft. If CDNC computed at $\bar{w}$ is used (instead of $\lambda^\star\sigma$) for autoconversion rate calculations (a current practice in climate models), A will be substantially underestimated. The worst underestimation occurs for the Urban aerosol, where the factor is ~ 10 for KK and ~ 2 for LD6 (Figure 2). The deviation seen for KK is related to the strong sensitivity of A to N_d; given that the parameterization was developed for “clean” drizzling clouds (i.e., N_d <150 cm^{-3}), it is possible that its usage for polluted clouds may be outside of its region of applicability. This agrees with *Hsieh et al.* [2009a], whom found that deviation of KK from observation-derived autoconversion was largest when clouds were far from a drizzling state. Averaged over all aerosol types considered, the underestimation factor is 5.5 for KK, and 1.7 for LD6.

2.5.2 Effective radius

The droplet effective radius, r_e, is a key parameter of the cloud droplet distribution used for calculating cloud optical depth. r_e depends on N_d as,

$$r_e = \beta \left(\frac{3\rho_a}{4\pi\rho_w}\right)^{1/3} q_c^{1/3} N_d^{-1/3} \tag{15}$$

where β is a spectral dispersion parameter ranging from 1.1 to 1.6 (*Y.G. and Daum* [2005]). β exhibits a weak dependence on q_c and N_d (i.e., w) (*Y.G. and Daum* [2005]; *Liu et al.* [2006b, 2008]). We will therefore first consider β as a constant during the PDF integration (equal to the value for $q_c = q_c^\star$ and $N_d = N_d(w^\star)$).

By substituting N_d into Equation 15 with the Twomey parameterization, r_e and w are related by a power law, $r_e = \{3\beta\rho_a q_c/(4\pi\rho_w f(c,k))\}^{1/3} w^{-k/(2k+4)}$. Equation 8 can then be used, with a and b equal to $\{(3\beta\rho_a q^\star)/(4\pi\rho_w f(c,k))\}^{1/3}$ and $-k/(2k+4)$ respectively, to determine the dependence of the relevant characteristic velocity (such that $r_e(\lambda^\star\sigma) = \bar{r_e}$) on the slope of the CCN spectrum. Figure 1a shows that $\lambda^\star$ for r_e ranges between 0.46 and 0.52; averaged over the atmospherically relevant range of k, $\lambda^\star_{avg} = 0.48$, corresponding to 60% of $\bar{w}$.

Numerically calculating $\lambda^\star$ with the *Fountoukis and Nenes* [2005] parameterization (Figure 2a, dashed line) indicates that $\lambda^\star$ ranges between 0.50 and 0.70 (with $\lambda^\star_{avg} = 0.54$). Using $N_d(\bar{w})$ to estimate effective radius leads to an average 10% underestimation (13% for urban aerosol) relative to r_e^{avg}. When the Twomey-derived $\lambda^\star_{avg} = 0.48$ is used, r_e^{avg} is underestimated on average by only 2%.

Liu et al. [2008] proposed an empirical parameterization to account for the dependence of β on q_c and N_d, in which β scales with $(q_c/N_d)^{-0.14}$. The r_e expression still maintains its power law dependence on q_c and w, but the exponent in the latter changes from $-k/(2k+4)$ to $-0.57k/(2k+4)$. With this modification, $\lambda^\star_{avg} = 0.50$ using the Twomey parameterization and 0.62 with the *Fountoukis and Nenes* [2005] parameterization.

2.6 Summary - Conclusions

This study presents a computationally-effective framework to address the issue of PDF-averaging of CDNC that arise from subgrid scale variations in vertical velocity. Central to the framework is the concept of a “characteristic velocity”, $w^\star$, which if introduced into a mechanistic CDNC parameterization provides a droplet number concentration characteristic of the value averaged over a PDF of updraft velocity. The concept of characteristic velocity is then extended for calculation of cloud properties and process rates, such as autoconversion and effective radius.

The approach of using characteristic values of q_c and N_d in place of integrating over a PDF requires knowledge of its functional form; this may be possible for certain climatically important cloud types, such as stratocumulus in well-mixed boundary layers. Based on the weak correlation between w and q_c for these cloud, we propose the usage of a joint PDF that is the product of two functions, each representing the PDF of q_c and w, respectively. This, together with the power-law dependence on q_c and N_d (often characterizing cloud process parameterizations) allows the determination of $w^\star$ that complement existing treatments for subgrid variability of liquid water content.

Analytical expressions for $w^\star$ (or its equivalent non-dimensional form $\lambda^\star = w^\star/\sigma$) are determined assuming a Gaussian PDF of updrafts and CDNC from the parameterization of *Twomey* [1959]. $\lambda^\star$ was also numerically determined with the *Fountoukis and Nenes* [2005] parameterization for a wide range of aerosol size and updraft velocity distributions. Both approaches give $\lambda^\star$ that are in close agreement (e.g., for N_d, both agree to within 3%), ensuring that the analytical expressions are accurate approximations of $\lambda^\star$. For CDNC, $\lambda^\star$ is $\approx$ 15% lower than $\bar{w}$, but within the 20% experimental uncertainty associated with the "optimal" $\lambda = 0.8$ determined using in-situ cloud observations (*Peng et al.* [2005], *Conant et al.* [2004], *Meskhidze et al.* [2005] and *Fountoukis et al.* [2007]). Using $\bar{w} = 0.79\sigma$ to compute N_d overestimates $\bar{N}_d$ by about 10%. In calculations of effective radius, using $\bar{w}$ underestimates PDF-averaged values by $10 - 15\%$ ($\sim 1 - 2\mu$m); $\lambda^\star$ for this microphysical parameter is on average 68% of the average updraft. Owing to its strongly nonlinear dependence on N_d, $\lambda^\star$ for autoconversion rate calculation is $\sim 30 - 40\%$ of $\bar{w}$; depending on the parameterization used, estimating autoconversion rate with $\bar{w}$ underestimates A on average by a factor of $2-5$.

This study presents a methodology that maps, in a simple way, the subgrid-scale variability of w onto subgrid-scale variability of N_d. We demonstrate that using $\bar{w}$ for calculations of N_d, r_e and A (a common practice in GCMs) leads to biases which are especially significant for autoconversion rates. This bias can be corrected if an appropriate $w^\star$ (specific to each cloud property or microphysical parameterization) is used. Before it is implemented however in large-scale models, the method still needs to be evaluated against detailed cloud simulations and in-situ observations. Future work will focus on this and derivation of $w^\star$, q_c for a wide range of cloud process parameterizations. Nevertheless, the method of characteristic properties carries much potential, as it addresses parameterization "tuning" in a physically-based way. More importantly, the approach may present an important step forward for GCM studies of the aerosol indirect effect, which ignore any treatment of subgrid-scale variability of N_d.

2.7 Acknowledgments

We acknowledge support form NASA-ACMAP and NSF-CAREER. We would also like to thank Anne Chen, three anonymous reviewers and the Associate Editor Dr. Steve Ghan for comments that have substantially improved the manuscript.

CHAPTER III

ON THE IMPACT OF SUBGRID VARIABILITY OF CLOUD DROPLET NUMBER ON CLOUD MICROPHYSIC IN THE COMMUNITY ATMOSPHERE MODEL

3.1 Introduction

The scale at which aerosol-cloud interactions occur is much smaller that those resolved by Global Circulation Models (GCM), with horizontal grid spacing of the order of 200 km. Because of this important gap between the resolved scales and those relevant for cloud microphysics, the small-scale processes and properties in the cloud-schemes of GCMs must be parameterized.

Liquid-cloud microphysical schemes in earlier generations of GCMs included only the mass mixing ratio of liquid water, q_l as a prognostic variable (e.g., *Sundqvist* [1978]). However, the need to realistically represent aerosol-cloud interactions has pushed these models to add new microphysical variables (e.g., concentration of liquid and ice hydrometeors) and processes that couple them. Accordingly, newer generations of GCM now feature two moment cloud microphsyical schemes, where prognostic equations for hydrometeor amount (e.g, droplet number concentration of droplets, N_d, and ice, N_i) and mass mixing ratios (e.g., *Salzmann et al.* [2010]; *Dentener et al.* [2011]; *Lohmann et al.* [2007]) are considered. The most direct of these links between aerosols and liquid clouds, is the process of aerosol activation. This is the step at which a subset of atmospheric aerosol gets activated into cloud droplets, and represents the source term for N_d. The number of activated aerosol particles is a strong function of aerosol size distribution, aerosol composition, and updraft velocity, w. The treatment of the cloud-scale relevant updraft velocity, which is unresolved, has been discussed in other studies [e.g., *Morales and Nenes*, 2010] and its sensitivity tested in climate models [e.g., *West et al.*, 2013; *Zhao et al.*, 2013].

Stratiform clouds in GCM cloud-schemes are often assumed to be uniformly and homogeneously distributed horizontally in a given grid cell. However, it has been shown that inhomogeneities in the horizontal structure of clouds (for instance, in their liquid water content) can profoundly affect processes that have strong non-linear dependency with respect to the variable in question (e.g., *Pincus and Klein* [2000]; *Larson et al.* [2000]; *Rotstayn* [2000]). Microphysical schemes in GCMs account for the horizontal inhomogeneities in cloud liquid water content, assuming a probability distribution (PDF) function to describe the variations (e.g., *Tompkins* [2001]; *Golaz et al.* [2002]; *Cheng and Xue* [2009]). The 2-moment microphysical scheme of *Morrison and Gettelman* [2008] assumes that the in-cloud liquid water content follows a gamma distribution, and all the microphysical process rates that depend on q_c, are represented by average values obtained after integration over the PDF. This approach has two advantages. First, it accounts for the non-linear dependence of each process rate separately, and therefore, each process rate is affected by a specific 'enhancement factor'. Second, the simple PDF chosen allows to compute the integrations analytically. Despite of the importance of inhomogeneities in other cloud variables (e.g., droplet number), they have not been included.

Representing the subgrid scale (SGS) variability in physically consistent ways is important to ensure that cloud microphysical processes and properties are consistently expressed at the grid scale. *Morales and Nenes* [2010] proposed the use of a similar approach for the in-cloud droplet number concentration, N_d. Unlike the treatment of SGS variability of q_l, which often uses observed distributions of cloud optical thickness [*Baker*, 1996; *Pincus et al.*, 1999], *Morales and Nenes* [2010] proposes a physical link to determine the in-cloud distribution of N_d. The corresponding PDF distribution of N_d was proposed to emerge as a consequence of the SGS variability in updrafts. Since the droplet number of activated cloud droplets from activation parameterizations is a strong function of w, SGS variability in updraft translated into a probability density function of activated N_d. Therefore, SGS variability in N_d could be addressed in this way.

Following this idea, *Tonttila et al.* [2013] investigated the impact of SGS variability of N_d on the autoconversion rate using the ECHAM5-HAM GCM. The autoconversion rate, A, is the rate of conversion of cloud water to rain. It was found that the impact of accounting for SGS variability on N_d produced a reduced CDNC and enhanced autoconversion rates. Their study showed that application of this scheme lead to a reduction of the amount of tunning required to achieve radiation balance at the top of the atmosphere. Nevertheless, their implementation of SGS of droplet number uses a Monte-Carlo approach in the framework of the Independent Column Approximation [*Pincus et al.*, 2003], which is computationally expensive.

In this study, we test and implement the impact of SGS variability of updraft velocity on autoconversion rate, through its impact on the droplet number concentration, following the scheme of *Morales and Nenes* [2010], in the framework of the CAM5.1 model. The differences in the main cloud related variables are computed and discussed.

3.2 Cloud microphysics in CAM5

A detailed description of the cloud microphysics in CAM5.1 is available at (http://www.cesm.ucar.edu/models /cesm1.0/cam/). Here we briefly describe the most important processes linked to aerosol activation. We used the 3-mode version of the modal aerosol module (MAM3) [*Liu et al.*, 2012], which provides the necessary information for the aerosol activation routines. The geometric standard deviation σ_{gi} of each mode is prescribed, but aerosol number concentration (n_{ai}) and mode diameter (d_{gi}) for each mode are allowed to vary to accommodate the corresponding mass.

Aerosol activation is computed with the parameterization of *Abdul-Razzak and Ghan* [2000], which is a function of the aerosol size distribution, chemical composition, and updraft velocity. The number of activated droplets for a given updraft, w, is denoted here $N_a(w)$. The subgrid vertical velocity used in the aerosol activation process, w_{sub}, is computed from the turbulent kinetic energy as $w_{sub} = \sqrt{TKE}$, with $0.2 \leq w_{sub} \leq 10$ ms^{-1}. The number of aerosols activated into cloud droplets is then given by $N_a(w_{sub})$. The aerosol in CAM interacts with stratiform clouds using the double moment cloud microphysics scheme of *Morrison and Gettelman* [2008]. The aerosol activation process is the source term for the gridbox CDNC equation balance. The fraction of aerosols activated into cloud droplets can be removed by wet scavenging or regenerated to the interstitial aerosol population after cloud evaporation.

Among the process rates included in the *Morrison and Gettelman* [2008] microphysics, autoconversion of cloud water to rain has the strongest non-linear dependence on droplet number concentration. This process is described by the *Khairoutdinov and Kogan* [2000], i.e.,

$$A_q(q_c, N_d) = \left(\frac{dq_c}{dt}\right)_a = -Kq_c^{2.47}N_d^{-1.79} \tag{16}$$

where K is a dimensional constant, equal to $K = 1350$ when N_d is in cm^{-3} and q_c in kg kg^{-1}. The corresponding term accounting for autoconversion of droplet number, N_d, to rain is given by,

$$A_N(q_c, N_d) = \left(\frac{dN_d}{dt}\right)_a = \frac{N_d}{q_c}A_q \tag{17}$$

In this work we explore the impact that subgrid variability in N_d has on these two microphsyical process rates.

3.3 Implementation of SGS variability

Here we describe the necessary assumptions made in the implementation of the *Morales and Nenes* [2010] scheme into the *Morrison and Gettelman* [2008] cloud microphysics performed in the CAM5.1 model.

The first assumption is to consider that there is a distribution of in-cloud droplet number concentration, denoted $P_n(N_d)$, assumed to be independent of the PDF of in-cloud liquid water content, $P_q(q_c)$. This is expected to apply only for the large scale stratiform clouds *Morales and Nenes* [2010]. This assumption allows to decouple the PDF of in-cloud q'_c from that of N'_d, so the joint PDF of both variables is given simply by their product. Therefore, the gridcell average autoconversion $\bar{A}_q$ is given by (see Equation (3)),

$$\bar{A}_q = -K \int P_q(q'_c) q'^{2.47}_c \mathrm{d}q'_c \int P_n(N'_d) N'^{-1.79}_d \mathrm{d}N'_d \tag{18}$$

The second assumption is to consider that all subgrid variability of N_d is produced by the SGS updraft variability at activation. More precisely, if we assume that there is a Gaussian PDF of updraft velocities, $P_w(w')$, characterized by a standard deviation σ_w, then $P(N'_d)$ is computed as the distribution induced by the activation parameterization $N_a(w)$ (Appendix B). Furthermore, we assume that the droplet number produced at activation, $N_a(w_{sub})$, is equal to $\bar{N}_a$, i.e., the PDF averaged value of $N_a(w)$. In this way it is possible to isolate the impact of SGS N_d variability on autoconversion. According to the *Morales and Nenes* [2010] scheme, this approach implicitly defines the width σ_w of the PDF of updrafts in terms of w_{sub}. Since $w_{sub} = \lambda_N \sigma_w$, the width of the Gaussian distribution, σ_w, is given by $\sigma_w = w_{sub}/\lambda_N$. Here, λ_A and λ_N denote the near constant factors of *Morales and Nenes* [2010] that define the characteristic velocities for autoconversion and droplet number respectively. Given these stipulations, the gridcell averaged autoconversion rate is given by,

$$\bar{A}_q = -K \int P_q(q_c') q_c'^{2.47} \mathrm{d}q_c' \int P_w(w') N_a(w')^{-1.79} \mathrm{d}w' \tag{19}$$

The first integral, can be easily computed since $P(q_c')$ is assumed to be a gamma distribution characterized by the mean q_c and by the relative variance ν_q [*Morrison and Gettelman*, 2008]. The second integral is not as straight forward, as in-cloud droplet number N_d is not explicitly a function of w. To overcome this issue, we adopt the approach of *Morales and Nenes* [2010] where the PDF average droplet number from activation can be computed by a single evaluation of the activation parameterization. This formalism can be easily written in terms of an enhancement factor for the autoconversion process, i.e.,

$$\int P(w') N_a(w')^{-1.79} \mathrm{d}w' = N_a(\lambda_A \sigma_w)^{-1.79} = E_N N_a(\lambda_N \sigma_w)^{-1.79} \tag{20}$$

with

$$E_N = \left[\frac{N_a(\lambda_A \sigma_w)}{N_a(\lambda_N \sigma_w)} \right]^{-1.79} \tag{21}$$

Given that A_q depends on the current in-cloud droplet number, we evaluate A_q at N_d, but assume that the enhancement factor can be computed using equation (21). With these modifications, the average autoconversion rate, $\bar{A}_q$, is given by

$$\bar{A}_q = E_q \, E_N \, A_q(q_c, N_d) \tag{22}$$

where E_q is the enhancement factor computed with the *Morrison and Gettelman* [2008] scheme, and E_N is the enhancement resulting from the application of the SGS variability of N_d given by equation (21). Autoconversion rates are often tunned by a an arbitrary factors to achieve reasonable radiative balance in the model [e.g., *Chen et al.*]. The factors E_N and E_q effectively replace this arbitrary tunning. A rough estimate of a typical value of E_N can be made by applying the power law approximation of *Morales and Nenes* [2010], $N_a \sim w^b$. Assuming a value of $b = 0.3$, $E_N \approx 1.6$. Therefore SGS should produce a moderate increase in autoconversion, with the exact impact depending on the underlaying aerosol, which determines the value of the exponent b.

Inclusion of this N_d SGS variability scheme, which results in autoconversion enhancement compared to the autoconversion computed at the average N_d of the grid-cell, is expected to produce a more efficient removal of cloud water, therefore decreasing the liquid water content in locations where autoconversion plays an important role in precipitation production. Equation (17) suggests that the enhanced A_q should also more efficiently remove droplets, decreasing N_d. This modifications are expected to cause a redistribution of the vertical structure of stratiform clouds simulated in CAM. However, the net impact on total precipitation is constrained by the relative contribution of autoconversion to precipitation production [*Gettelman et al.*, 2013].

3.4 Simulations considered

Two sets of simulations were performed to investigate the impact of N_d SGS variability on the simulated cloud fields in CAM. Simulations using emissions of aerosols, aerosol precursors, and atmospheric oxidants from the *Lamarque et al.* [2010] corresponding to year 2000 are termed PD, while those with aerosol emissions corresponding to year 1850 are termed PI. All the simulations used climatological sea surface temperature and greenhouse gases concentrations corresponding to year 2000. Present day (PD) and pre-industrial (PI) simulations where performed with the default configuration of the model (BASE), as well as with the modifications proposed in this study (AUTO). Table 2 list the the simulation setup for each numerical experiment.

The set of simulations was chosen so the impact of the SGS variability could be explored for PD and PI conditions, as well as to examine the potential impact of

Table 2: Summary and nomenclature of simulations

Experiment ID	SGS-variability	Aerosol Emissions
BASE-PD	No	Year 2000
BASE-PI	No	Year 1850
AUTO-PD	Yes	Year 2000
AUTO-PI	Yes	Year 1850

this treatment on aerosol indirect effect estimates, given by the difference in shortwave cloud forcing (SWCF) and longwave cloud forcing (LWCF) between PD and PI simulations.

3.5 Results and Discussion

The summary of annual mean all-sky and clear sky radiation fluxes, and column integrated cloud properties are included in Table 3. When comparing PD against PI simulations, it can be seen that both the BASE case and AUTO case have similar aerosol indirect effect metrics, with a 40% increase in column integrated droplet number and close values for ΔSWCF and ΔLWCF. The annual average precipitation rates also exhit almost identical values, showing close to no variation. A similar situation is observed for cloud cover, and ice water path.

The PD-PI indirect forcing and LWP differences were found to be similar for BASE and AUTO simulations, but the absolute values of some key cloud variables are markedly different. Simulations performed with the SGS variability treatment of autoconversion consistently exhibit lower SWCF, LWCF, LWP, and CDNUMC. Particularly strong is the difference in LWP, which on average is 14% larger for BASE simulations compared to AUTO. The spatial distribution of the difference in LWP are shown in Figure 3. Zonal mean LWP and SWCF are depicted in Figure 4. The difference in CDNUMC can be also substantial between BASE and AUTO cases (Figure 5).

Table 3: Summary of column integrated variables from the simulations in this study. Low cloud cover (CLDLOW), total cloud cover (CLDTOT), long wave (LWCF) and shortwave cloud forcing (SWCF), all-sky (FLUT) and clear-sky (FLUTC) longwave upwelling flux at TOA, all-sky (FSNTOA) and clear sky (FSNTOAC) net shortwave flux at top of the atmosphere

	BASE-PD	BASE-PI	AUTO-PD	AUTO-PI
CLDLOW (%)	0.455	0.447	0.45	0.449
CLDTOT (%)	0.640	0.640	0.638	0.636
IWP (gm^{-2})	17.81	17.69	17.73	17.56
LWP (gm^{-2})	44.47	40.46	38.73	35.52
PRECL (mm day^{-1})	0.868	0.870	0.877	0.885
PRECT (mm day^{-2})	2.961	2.982	2.963	2.983
CDNUMC ($10^{10}m^{-2}$)	1.33	0.95	1.15	0.82
ACTREL (μm)	8.64	8.88	8.53	8.74
ACTNL (cm^{-3})	70.80	53.22	66.91	50.26
FLUT (Wm^{-2})	235.08	235.87	235.39	236.32
FLUTC (Wm^{-2})	259.27	259.68	259.30	259.78
FSNTOA (Wm^{-2})	239.52	240.94	241.42	242.99
FSNTOAC (Wm^{-2})	291.40	290.84	291.56	291.04
LWCF (Wm^{-2})	24.18	23.81	23.90	23.46
SWCF (Wm^{-2})	-51.87	-49.90	-50.13	-48.04
ΔLWCF (Wm^{-2})	+0.37		+0.44	
ΔSWCF (Wm^{-2})	-1.97		-2.08	

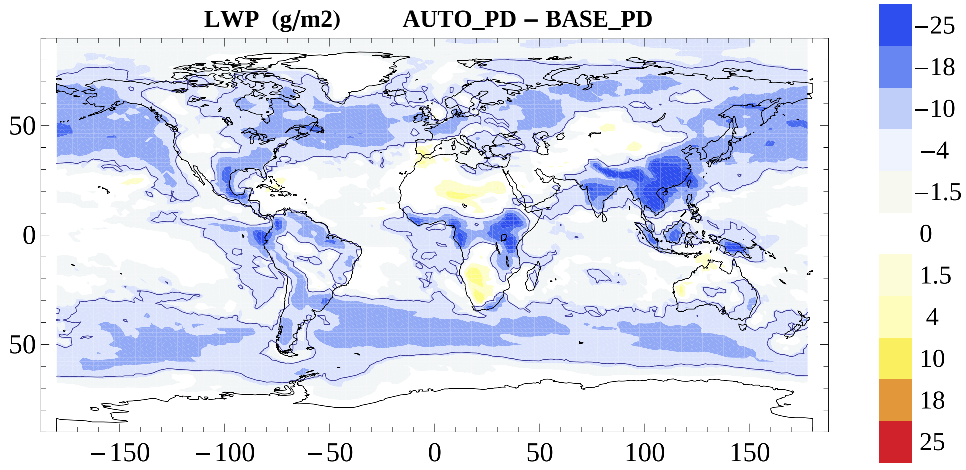

Figure 3: Difference between the liquid water path (LWP in $g\,m^{-2}$) for the AUTO-PD and BASE-PD simulations

The decrease in LWP when SGS variability of N_d is accounted for, is consistent with the enhanced A_q. More efficient removal of in-cloud water into rain water leads to an overall reduction in q_c, hence in LWP. Similarly, as implied by equation (17), when A_q is enhanced, the removal of N_d is also enhanced, and smaller overall cloud droplet number concentration should be expected.

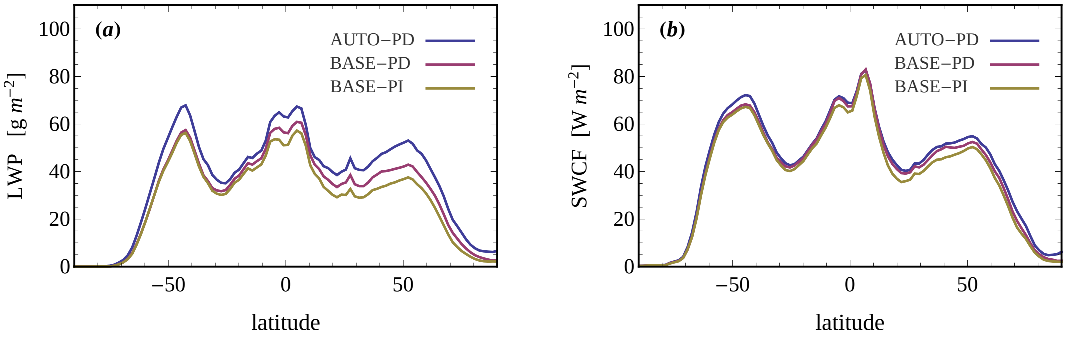

Figure 4: Zonal annual mean **(a)** liquid water path (LWP) and **(b)** short-wave cloud forcing (SWCF) in Wm^{-2}

Annual average precipitation is negligibly affected by the N_d SGS treatment of the autoconversion. This suggest that despite the more efficient rain generation (and in-cloud water removal), this does not translate into increased ground precipitation, but rather in modifications in the vertical structure of precipitation production and evaporation. Figure 6 show zonal means for some field directly related to precipitation production via autoconversion. Figure 6b, which depicts the rate of precipitation production including all mechanisms, shows that the response to autoconversion enhancement is not monotonic, and exhibits regions of increases and decreases in the net precipitation production. The largest changes in this field tend to occur at higher latitudes (where the net precipitation is low), and at medium heights. Some feedbacks in the other microphysical rate processes considered in *Morrison and Gettelman* [2008] can be responsible for this behavior. For instance, the rate of accretion of cloud water by rain, given by

$$\left(\frac{dq_c}{dt}\right)_{acr} = -K_{_a}(q_c\, q_r)^{1.15} \tag{23}$$

in this expression, q_r is the mixing ratio of rain produced in that time step. Therefore, a reduction in the in-cloud water q_c due to enhanced autoconversion, leads to a less efficient rain production through accretion, therefore, reducing the rate of removal of q_c.

3.6 Conclusions

A physically-based treatment of the droplet number subgrid scale (SGS) variability from vertical velocity SGS variations, was implemented in the Community Atmospheric Model CAM5.1. The impact of this scheme on the simulated autoconversion of liquid water to rain, was compared to the default model configuration, finding to cause an important reduction of the simulated liquid water path (14%), cloud droplet number (13%) and shorwave cloud frocing ($\sim$ 3%) where found when the enhancement of autoconversion was included. The resulting enhancement of autoconversion was on average 1.35 for the lowest model levels, it was shown to strongly impact the

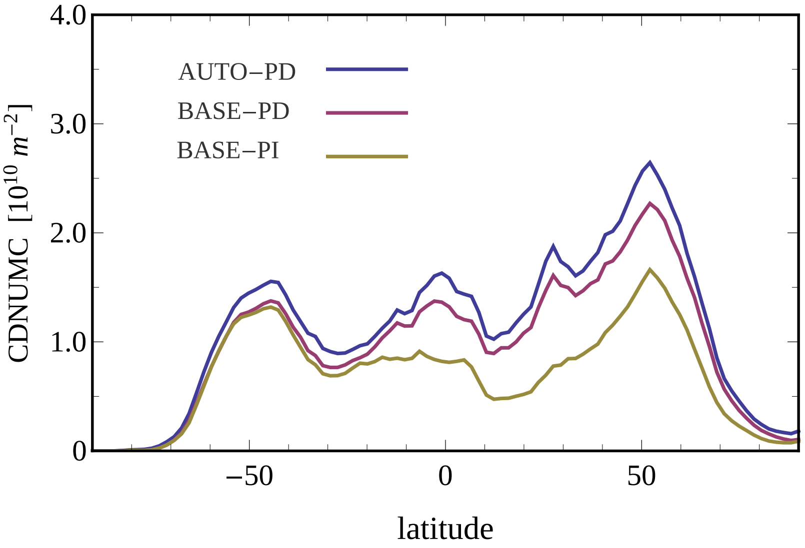

Figure 5: Zonal annual mean column integrated cloud droplet number (CDNUMC) for the AUTO-PD, BASE-PD, and BASE-PI simulations

structure of clouds in CAM.

These modification were found not to have a significant impact on the ΔSWCF between PD and PI simulations. Despite this, the results obtained in this study suggests that neglecting the impact of subgrid-scale variability can have important implications in the model physics. Future research efforts should be dedicated to the validation of this results by comparing radiation and cloud fields to satellite observations.

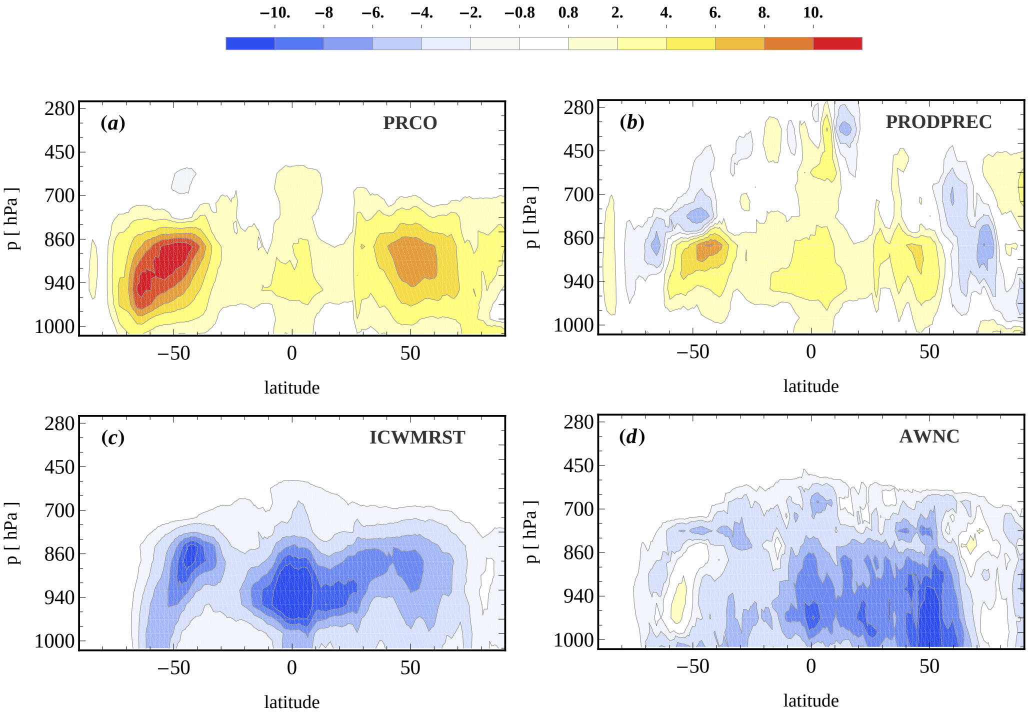

Figure 6: Zonal annual mean difference between AUTO-PD and BASE-PD simulations for: **(a)** Autoconversion rate (PRCO) in $kg\,kg^{-1}s$ **(b)** Precipitation production rate (PRECPROD) in $kg\,kg^{-1}s$ **(c)** in-cloud water mixing ratio for stratiform clouds (ICWMRST) in $g\,kg^{-1}$, and **(d)** in-cloud droplet number concentration (AWNC) in cm^{-3}.

CHAPTER IV

EVALUATION OF AN ENTRAINING DROPLET ACTIVATION PARAMETERIZATION USING IN-SITU CLOUD DATA

4.1 Summary

This study investigates the ability of a droplet activation parameterization (which considers the effects of entrainment and mixing) to reproduce observed cloud droplet number concentration (CDNC) in ambient clouds. Predictions of the parameterization are compared against cloud averages of CDNC from ambient cumulus and stratocumulus clouds sampled during CRYSTAL-FACE (Key West, Florida, July 2002) and CSTRIPE (Monterey, California, July 2003), respectively. The entrainment parameters required by the parameterization are derived from the observed liquid water content profiles. For the cumulus clouds considered in the study, CDNC is overpredicted by 45% with the adiabatic parameterization. When entrainment is accounted for, the predicted CDNC agrees within 3.5%. Cloud-averaged CDNC for stratocumulus clouds is well captured when entrainment is not considered. In all cases considered, the entraining parameteriztion compared favorably against a statistical correlation developed from observations to treat entrainment effects on droplet number. These results suggest that including entrainment effects in the calculation of CDNC, as presented here, could address important overprediction biases associated with using adiabatic CDNC to represent cloud-scale average values.

This chapter appears as reference *Morales et al.* [2011]

4.2 Introduction

Activation of atmospheric particles (termed cloud condensation nuclei, or CCN) by condensation of water vapor to form cloud droplets is the direct microphysical link between aerosols and clouds. Modifications in either the concentration or composition of atmospheric CCN can affect cloud microphysical properties. An increase in aerosol concentration, for example, generally leads to an increase in cloud droplet number concentration (CDNC), with subsequent impacts on cloud thickness, cloud albedo and precipitation [*Intergovernmental Panel on Climate Change*, 2007]. Aerosol-cloud interactions are amongst the most challenging of atmospheric processes to predict, because of the dynamical, microphysical and macrophysical feedbacks that occur across a wide range of temporal and spatial scales (which often operate at the subgrid scale in global climate models, GCMs) [*Stevens and Feingold*, 2009]. Nevertheless, a realistic representation of aerosol-cloud interactions is necessary for improved assessments of climate change.

Cloud microphysical properties in most GCM studies are determined based on the resolved liquid water content (q_l, kg kg^{-1}) and a parameterization of CDNC (N_d, cm^{-3}). These two variables are used to express the cloud microphysical characteristics relevant for cloud processes and radiative forcing calculations, such as effective radius of the droplet population, dispersion of the droplet size distribution (DSD) (e.g. *Liu et al.* [2008]), and autoconversion rate (e.g., *Khairoutdinov and Kogan* [2000]). Cloud schemes that include two-moment microphysics are based on solving prognostic equations for q_l and N_d, which relate both variables to an assumed droplet size distribution, the first and third moments of which are constrained by N_d and q_l, respectively (e.g. *Morrison and Gettelman* [2008]).

The need for accurate but computationally efficient representations of the droplet activation process in GCMs has lead to a large body of work (e.g., *Twomey* [1959]; *Abdul-Razzak et al.* [1998]; *Nenes and Seinfeld* [2003]; *Fountoukis and Nenes* [2005];

Ming et al. [2006]). These activation parameterizations are based on approximate solutions of the coupled mass and energy balances for an ascending Lagrangian cloud parcel, during which a population of particles activates to cloud droplets. This framework allows the calculation of water vapor supersaturation; a maximum value, s_m, is reached when the availability of water vapor from expansion cooling is equal to the loss from condensation onto the nucleated droplets. Knowledge of s_m is then used to determine the nucleated droplet number (that is, the number concentration of particles with critical supersaturation less than s_m). A thorough review and evaluation of activation parameterizations is provided by *Ghan et al.* [2011].

Entrainment has been long recognized as an important process shaping the droplet number concentration and size distribution of cloud droplets (e.g., *Warner* [1973]; *Lehmann et al.* [2009]). Mixing of cloud-free air in cloud is thought to occur in entrained "pockets" with a characteristic length scale of the order of the cloud itself, driven by the convective circulation in the cloud. The entrained air is then turbulently mixed with the cloudy air in a cascade of eddies down to the Kolmogorov scale, where molecular diffusion dominates transport [*Krueger et al.*, 1997]. The ratio of evaporation and turbulent mixing timescales has been found to determine the impact of the mixing process on the droplet size distribution and the CDNC [e.g., *Latham and Reed*, 1977; *Baker et al.*, 1980]. When the timescale of evaporation is much longer than that of turbulent mixing, all droplets are effectively exposed to the same supersaturation, partially evaporate, and then decrease in size at more or less constant CDNC ("homogeneous mixing"). Conversely, if the mixing process is slower than the evaporation process and well-defined interfaces between cloudy and clear air "pockets" are maintained sufficiently long, droplets surrounded by entrained air completely evaporate, while those surrounded by saturated cloudy air remain largely unaffected ("Inhomogeneous mixing"). At the inhomogeneous mixing limit, CDNC is depleted, while the shape of the droplet size distribution is essentially unchanged. Observations suggest that both entrainment mechanisms occur (e.g., *Burnet and Brenguier* [2006]). For a particular cloud, a length scale exists below which mixing is predominantly homogeneous, and above which mixing is inhomogeneous [*Lehmann et al.*, 2009]. Both mixing limits have been explored in modeling studies (e.g., *Krueger et al.* [1997]; *Lasher-Trapp et al.* [2005]). Modeling studies also suggest that entrainment-mixing effects may substantially affect the simulated albedo of clouds [*Chosson et al.*, 2006].

Cloud schemes in GCMs are often one-dimensional representations of clouds (i.e., with homogeneous characteristic across a horizontal section of the cloud), often based on the entraining plume concept that adopt the model of lateral entrainment and mixing (e.g., *Tiedtke* [1989]; *de Rooy and Siebesma* [1985]). They do not however account for entrainment impacts on droplet number, which is generally considered beyond the reach of GCM cloud schemes. Empirical approaches based on observations, which inherently include entrainment effects, have been proposed to circumvent this issue. *Leaitch et al.* [1996] derived such a correlation from marine stratus cloud observations, that link adiabatic to cloud-average CDNC. The relationship has seen application in the ECHAM model to represent entrainment effects on convective cloud microphysics [*Lohmann*, 2008]. Apart from such empirical approaches, other GCM schemes use adiabatic CDNC to represent the cloud-scale average CDNC, hence are subject to overprediction biases. *Barahona and Nenes* [2007] explored the implication of continuous, homogeneous mixing during the activation process, and developed a mechanistic parameterization (hereafter BN07) that includes the effects of entrainment on the number of nucleated cloud droplets. Assuming that droplet concentrations predicted with BN07 represents cloud-scale average CDNC, *Barahona et al.* [2011] applied the parameterization within a global model simulation (using a variety of approaches to represent entrainment) and was found to improve the representation of spatial patterns of CDNC and cloud droplet effective radius. BN07 however has not been tested against in-situ measurements, particularly in combination with approaches to

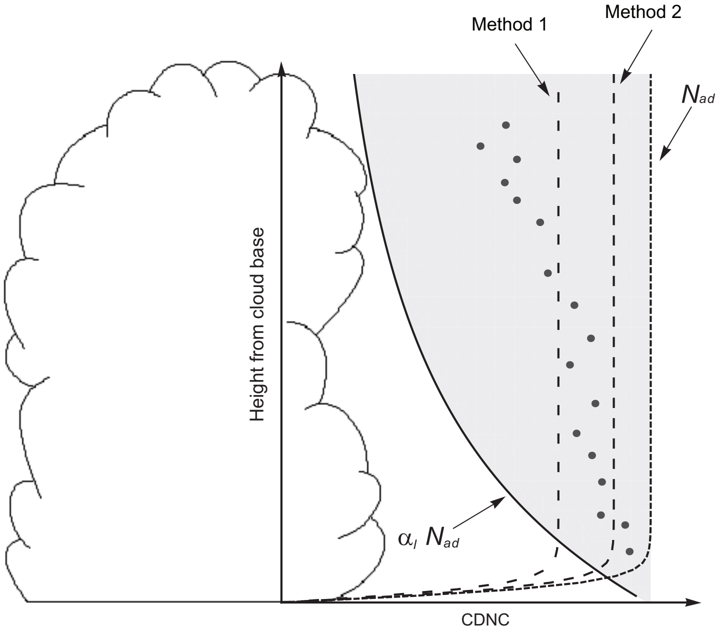

Figure 7: Schematic of the expected impact of predicted CDNC with the different approaches discussed in the text. The points represent actual observed CDNC, while the shaded area represents the region bounded by the adiabatic (N_{ad}) and inhomogeneous mixing limits ($\alpha_l N_{ad}$). Dashed lines represent CDNC predicted with BN07 when: $(1 - \mu/\mu_c) \sim \alpha_{l,avg}$, and, $(1 - \mu/\mu_c)$ derived from least square fits to observed α_l profiles.

determine entrainment rates that are consistent with observed liquid water content profiles.

The focus of this work is to investigate the ability of the BN07 activation parameterization to reproduce cloud-scale average CDNC observed in ambient clouds. We focus on two major types of warm clouds, cumulus and stratocumulus. Unlike previous studies that evaluate parameterizations with observations at cloud-base or for near-adiabatic parcels, closure is assessed for cloud-average values of CDNC (which is what is required in GCM simulations). To avoid biases in the observed CDNC resulting from droplet collision and coalescence, the study is carried out for clouds in the absence of substantial amounts of drizzle.

4.3 The conceptual framework

Entrainment and mixing is likely to deplete the liquid water content and the CDNC through the entire cloud column; this implies that at the cloud scale, neither variable will be adequately represented by adiabatically calculated values (although the latter can closely approximate values near cloud base; *Meskhidze et al.* [2005]). CDNC predicted with an entraining parameterization could however more realistically represent the cloud scale-average CDNC, especially if the entrainment rate applied is consistent with the vertical profile of cloud liquid water. This conceptual framework presented in Figure 7; assuming adiabatic CDNC throughout the cloud column tends to overpredict the quantity on average when compared against observations (symbols). Using BN07 to predict the average cloud-column CDNC can lead to better agreement with observations (given the appropriate entrainment rate).

BN07 adopts the continuously entraining, homogeneous mixing model [*Pruppacher and Klett*, 1997] to compute droplet number; it involves a Lagrangian parcel of cloudy air which is allowed to exchange mass with the environment at a per unit length entrainment rate μ (m^{-1}). The environmental air is characterized by its temperature and water vapor mixing ratio, T' and q'_v respectively. As the parcel ascends, supersaturation is initially generated and cloud droplets nucleate until mixing and water condensation dominate over water availability from expansion cooling. The resulting activated CDNC is subsequently applied uniformly in the vertical (Figure 7).

The entrainment model adopted in BN07 was developed for cumulus convection; we therefore expect the predicted CDNC with this formulation to better reproduce observations of small cumulus clouds than the stratocumulus cloud cases, where the entrainment process has a different structure and cloud microphysical impacts. For completeness however we test the entraining parameterization for both cloud types. In the following sections we describe the activation parameterization and its application to represent the average CDNC in ambient clouds. Different strategies to diagnose the effective entrainment rate from observed liquid water content profiles are developed. Quantitative implications of entrainment on the predicted CDNC and effective radius are provided and discussed within the context of published literature.

4.3.1 The entraining activation parameterization

BN07 is an extension of the work of *Nenes and Seinfeld* [2003] and *Fountoukis and Nenes* [2005] (FN05 hereafter); it can treat the effects of externally-mixed aerosol, CCN containing partially-soluble compounds and surfactants that affect surface tension and facilitate activation, and delays in activation kinetics from the presence of film-forming compounds and slowly-dissolving compounds. The parameterization has also been extended to include droplet formation from adsorption activation of insoluble aerosol (e.g., dust) [*Kumar et al.*, 2009] and a detailed consideration of water vapor depletion from large and giant CCN *Barahona et al.* [2010a]. BN07 accurately reproduces detailed parcel model simulations. Its adiabatic counterpart, FN05, has been shown to reproduce CDNC for nearly adiabatic conditions in cloud-base transects sampled in ambient cumulus and stratocumulus clouds [*Meskhidze et al.*, 2005; *Fountoukis et al.*, 2007].

BN07 is based on the rate of change of the supersaturation, s, in the entraining cloud parcel [*Pruppacher and Klett*, 1997; *Barahona and Nenes*, 2007],

$$\frac{ds}{dt} = \alpha w \left[1 - \frac{\mu}{\alpha} \left(\frac{q_v - q_v'}{q_v} - \frac{M_w L_v \Delta T}{RT^2} \right) \right] - \gamma \left(\frac{dq_l}{dt} \right)_c \tag{24}$$

where $(dq_l/dt)_c$ is the condensation rate of water into the droplets, $\alpha = \frac{gM_wL_v}{c_pRT^2} - \frac{gM_a}{RT}$, $\gamma = \frac{pM_a}{e_s(T)M_w} + \frac{M_wL_v}{c_pRT^2}$, w is the updraft velocity of the parcel, M_a and M_w are the molecular weights of air and water, respectively, L_v is the heat of vaporization of water, c_p is the specific heat capacity of air, g is the gravitational acceleration, p is the pressure, $e_s(T)$ is the saturation vapor pressure, and R is the universal gas constant. The terms in brackets represent the effects of the entrainment in the parcel supersaturation, where q'_v is the water vapor mixing ratio of the entrained air, and $\Delta T = T - T'$ is the difference between the parcel and environmental temperatures.

Fundamental to BN07 is the concept of the *critical entrainment rate*, μ_c, defined as the entrainment rate above which cloud formation is prevented by excessive dilution of the ascending parcel by environmental air *Barahona and Nenes* [2007]. Under aerosol mass concentrations $\leq 100\,\mu\mathrm{g\,m^{-3}}$, where the water condensed on the aerosol before saturation can be neglected, μ_c was shown to be $\mu_c = \alpha q_{vs}\left(q_{vs} - q'_v - \frac{L_v M_w q_{vs} \Delta T}{RT^2}\right)^{-1}$, where q_{vs} is the saturation mixing ratio (i.e., μ_c is equal to the reciprocal of the factor multiplying μ in equation (24) evaluated at saturation). With these definition, and near cloud base, equation (24) can be written as

$$\frac{ds}{dt} = (1 - \mu/\mu_c)\alpha w - \gamma\left(\frac{dq_l}{dt}\right)_c \tag{25}$$

This expression describes how the mixing during the droplet activation process can decrease the maximum supersaturation (and therefore the CDNC) compared to activation under adiabatic conditions. Most physically-based droplet activation parameterizations calculate the adiabatic CDNC by determining the maximum supersaturation, s_m, that develops in the cloudy parcel (thus solving $(ds/dt) = 0$ in Equation (25) for $\mu = 0$). Based on Equation (25) BN07 showed that any adiabatic activation parameterization (based on equation (25) for $\mu = 0$) can account for the effects of entrainment on CDNC if the updraft velocity w is replaced with $(1-\mu/\mu_c)w$ in an adiabatic calculation. This operational modification does not imply that the physical updraft w is decreased, but accounts for the decrease in the water vapor availability as expressed in the first term of the right hand side of Equation (24) or (25).

Different methods to infer the entrainment parameter $(1-\mu/\mu_c)$ from cloud observations are discussed in section 4.3.2, and a quantitative description of the expected effects of this modification in the predicted CDNC, N_d, is provided in section 4.3.3.

4.3.2 Determination of the entrainment parameters

Application of BN07 requires specification of $(1-\mu/\mu_c)$; this quantity can be estimated from liquid water content (LWC) profile observations if a relation between $q_l(z)$ and the entrainment parameter $(1-\mu/\mu_c)$ can be established. Assuming that all the water vapor in excess of saturation condenses in the ascending parcel (appropriate for warm clouds where supersaturation rarely exceeds 1%), s and ds/dt in-cloud are identically zero. The vertical distribution of (subadiabatic) liquid water can then be determined from Equation (25). This is done by setting $ds/dt = 0$, solving the resulting equation for $(dq_l/dt)_c$, and noticing that the total change in the liquid water content (dq_l/dt) includes the sum of the condensation rate $(dq_l/dt)_c$ and the dilution from entrainment of non-cloudy air, $(dq_l/dt)_{dil} = -\mu w q_l$. Finally, considering that $w(dq_l/dz) = (dq_l/dt)$, the resulting expression is

$$\frac{dq_l}{dz} = \Gamma_{l,ad}(1-\mu/\mu_c) - \mu q_l \tag{26}$$

where z is the vertical coordinate and $\Gamma_{l,ad} = \alpha/\gamma$ is the adiabatic liquid water content lapse rate (given by Equation (25) for $\mu = 0$). If $\Gamma_{l,ad}$ and μ/μ_c are assumed constant with height, Equation (25) can be analytically integrated from cloud base height z_{cb} (the height where saturation is reached, such that $q_l(z) > 0$ for $z \geq z_{cb}$) to a height z. The integrated solution can be expressed in terms of the *dilution ratio*, α_l, the ratio of $q_l(z)$ to the adiabatic liquid water mixing ratio, $q_{l,ad} = \Gamma_{l,ad}(z - z_{cb})$,

$$\alpha_l(z) = \frac{q_l(z)}{q_{l,ad}(z)} = (1-\mu/\mu_c)\frac{1-\exp\big[-\mu(z-z_{cb})\big]}{\mu(z-z_{cb})} \tag{27}$$

Despite its simplifications, Equation (27) qualitatively reproduces some characteristics of observed α_l profiles. For all in-cloud heights $z \geq z_{cb}$, $\alpha(z) \leq 1$, and in particular, $\alpha(z) \leq (1-\mu/\mu_c)$. Equation (27) also implies that for small in-cloud heights (i.e., $\mu(z-z_{cb}) \ll 1$), $\alpha_l(z) \approx (1-\mu/\mu_c)$, while higher up in the cloud

$\alpha_l \sim (z - z_{cb})^{-1}$. This is consistent with observational studies that show a decrease in α_l with height (e.g., *Warner* [1970]; *Peng et al.* [2002]; *Lu et al.* [2008]).

Equation (27) also suggests that measurements of α_l could provide the basis for inferring $(1 - \mu/\mu_c)$. In principle, observations of α_l near cloud base (i.e., $\mu(z - z_{cb}) \ll 1$) are approximately equal to $(1 - \mu/\mu_c)$. However, such measurements are sensitive to the choice of z_{cb} (which exhibits significant variability), so that $z - z_{cb}$ is subject to considerable uncertainty for low in-cloud heights (e.g., *Arabas et al.* [2009]). This makes it impractical to use measurements of α_l near cloud base as a proxy for $(1 - \mu/\mu_c)$. Given these considerations, we use two methods to constrain $(1 - \mu/\mu_c)$ with observations. "Method 1" is to use cloud averages of the observed $\alpha_l(z)$ profile ($\alpha_{l,avg}$). This method is expected to provide a lower bound for $(1 - \mu/\mu_c)$ because the height dependent factor in Equation (27) is always less than unity. In "Method 2", a two-parameters least-squares fit of Equation (27) (to determine μ and $(1 - \mu/\mu_c)$) to the observed $\alpha_l(z)$ profile is performed. The two fitting parameters chosen for this procedure were μ and (μ/μ_c), subject to the constraints $\mu \geq 0$ and $0 \leq (\mu/\mu_c) \leq 1$. The details of the empirical determination of z_{cb} and of the observed α_l profiles is given in Section 4.4.

4.3.3 Impact of entrainment parameters on CDNC and effective radius

The inferred entrainment parameters, necessary input for the BN07 parameterization, should be such that the predicted CDNC is representative of the observed cloud average CDNC. However, the different methods proposed to estimate this entrainment parameter, have different impacts on the predicted CDNC (as well as in related variables such as the effective radius of the droplet population, r_e). The likely impact of these different approaches in the predicted droplet concentration with BN07 are discussed here and compared against the limits of mixing.

Under adiabatic conditions ($\mu = 0$), BN07 and FN05 predict the same adiabatic

CDNC, denoted N_{ad}. This value is likely to represent an overprediction of the true average CDNC since it does not take into account depletion of CDNC by mixing. N_{ad} exhibits an approximate power-law dependence on the updraft velocity, i.e., $N_{ad} \approx aw^b$, (with a, b positive parameters independent of w *Morales and Nenes* [2010]). According to BN07, entrainment effects on CDNC can be included by replacing w in the calculation of N_{ad} with $(1 - \mu/\mu_c)w$, so the corresponding predicted droplet number concentration under the entrainment rate μ, N_e, is $N_e(w) \approx (1-\mu/\mu_c)^b N_{ad}(w)$. Since $(1 - \mu/\mu_c) \le 1$, and $b \le 1$ for atmospheric aerosol [*Morales and Nenes*, 2010], we obtain the expected $N_e \le N_{ad}$. The inhomogeneous mixing process, in which all the LWC depletion results from decrease in CDNC (i.e., $N_d \approx \alpha_{l,avg} N_{ad}$), should constitute a lower bound on the actual CDNC. While this inhomogeneous mixing scenario could occur in certain regions in the cloud, it will most likely not be the case for a cloud-scale average CDNC [*Lu et al.*, 2008]. Finally, since $\alpha_{l,avg} \le (1 - \mu/\mu_c)$, the following inequalities for CDNC apply,

$$(\alpha_{l,avg})N_{ad} \le (\alpha_{l,avg})^b N_{ad} \le (1 - \mu/\mu_c)^b N_{ad} \le N_{ad} \tag{28}$$

Equation (28) illustrates the expected impact of both methods of introducing entrainment in the BN07 parameterization (i.e., $N_e \approx (\alpha_{l,avg})^b N_{ad}$ for Method 1, and $N_e \approx (1 - \mu/\mu_c)^b N_{ad}$ for Method 2). Each method has the desirable property of being bounded by the inhomogeneous mixing scenario and the adiabatic CDNC. Figure 7 shows schematically how CDNC predicted with these different methods likely compares to observed values.

Observations of cloud-scale averages of microphysical properties in shallow cumulus by *Lu et al.* [2008] are consistent with the above analysis. The cloud-scale ratio of observed to adiabatic CDNC was always greater than the dilution ratio, and for non-precipitating clouds never exceeds unity, i.e., $(\alpha_{l,avg})N_{ad} < N_{obs} < N_{ad}$.

The discussion above is also consistent with changes in effective radius, r_e, as observed at the cloud scale. Assuming that entrainment effects on the relative dispersion of the droplet size distribution are second order, $r_e/r_{e,ad} \sim (\alpha_l)^{1/3}(N_{ad}/N_e)^{1/3}$ *Kim et al.* [2008], where $r_{e,ad}$ is the effective radius computed from N_{ad} and $q_{l,ad}$. In the limit where homogeneous mixing occurs and neglecting the dilution of CNDC due to entrainment it is observed that $N_{ad}/N_e \to 1$, and $(r_e/r_{e,ad})$ becomes proportional to $\alpha_l^{1/3}$ (e.g., *Kim et al.* [2008]). In the inhomogeneous mixing limit, $\alpha_l \approx N_e/N_{ad}$, and r_e will, to first order, remain unaffected. If the departure of both N_d and q_l from adiabatic values is accounted for following the formulation previously discussed, then the expected impact on the calculated effective radius would depend on the dilution ratio as, $(r_e/r_{e,ad}) \sim \alpha_l^{(1-b)/3} \leq 1$. These predictions are consistent with the cloud-scale observations of *Lu et al.* [2008], and also fall in between the result under any of the two extreme cases of mixing. All together this suggests that using a entrainment rate diagnosed from the dilution ratio will give q_l profiles, N_d, and r_e consistent with observations. Furthermore, the treatment proposed here allows for a nonlinear relation between α_l and N_d.

4.4 Cloud observations used for the evaluation

The data sets used in this study were collected using the CIRPAS Twin Otter aircraft during the CRYSTAL-FACE (Key West, Florida, July 2002) and CSTRIPE (Monterey, California, 2003) field campaigns. CRYSTAL-FACE focused on cumulus clouds, while CSTRIPE addressed stratocumulus clouds off the California coast. These sets have been used in several studies of cloud microphysics and aerosol-cloud interactions, including an aerosol-CCN closure (*VanReken et al.* [2003]), aerosol-CDNC closure (*Conant et al.* [2004]; *Meskhidze et al.* [2005]), autoconversion parameterization evaluation (*Hsieh et al.* [2009a]) and comparisons between observed and predicted droplet size distributions (*Hsieh et al.* [2009b]). Descriptions of the instrumentation, sampling techniques and analysis are provided in the aforementioned studies; only a brief description of the data relevant for evaluation of the activation parameterization is given here.

A total of 8 stratocumulus decks sampled during the CSTRIPE campaign (including the 52 in-cloud transects considered in *Meskhidze et al.* [2005]), and 18 cumulus clouds (143 in-cloud transects) observed during CRYSTAL-FACE are considered in this study. Cloud microphysical properties were sampled at 1 Hz frequency using a Forward Scattering Spectrometer Probe (FSSP) in a series of horizontal in-cloud transects. The horizontal sampling transects were performed at heights ranging from near cloud base to cloud top, spanning most of the cloud depth. Vertical profiles of CDNC and liquid water content were then reconstructed from the FSSP measurements. Examples of the typical LWC profiles observed in these clouds are included in Figure 8. Updraft velocity measurements were performed with a five-hole turbulence probe. The cloud-scale average CDNC reported in this study was calculated as an average over the total number of CDNC data points for each cloud as derived from the FSSP measurements.

The entrainment parameter, $(1-\mu/\mu_c)$, is constrained using the methods described in Section 4.3.2, both requiring observed values of α_l at different in-cloud heights. The adiabatic liquid water content lapse rate, $\Gamma_{l,ad}$, was calculated from the measured temperature and pressure. Cloud base height, z_{cb}, was estimated by extrapolating the LWC measured at the lower cloud penetrations, assuming those points followed the linear profile given by adiabatic condensation, $q_{l,ad} = \Gamma_{l,ad}(z - z_{cb})$. Estimation of cloud base with this method has been used in other studies (e.g., *Peng et al.* [2002]). Once z_{cb} is determined, estimation of the dilution ratio α_l at the observation height z, was done by dividing the observed liquid water content $q_{l,obs}(z)$ at height z, with the expected adiabatic value, i.e., $\alpha_l(z) \approx q_{l,obs}(z)/q_{l,ad}(z)$ for each observed LWC data point. After completing these steps, near cloud-base data points were discarded and only the remaining data points were used in the calculations of $\alpha_{l,avg}$ (Methdod

Table 4: Cloud average cloud droplet number concentration (N_d) and dilution ratio ($\alpha_{l,avg}$) for the CSTRIPE stratocumulus clouds considered in this study. Uncertainties for each parameter correspond to one standard deviation from the mean. Cloud identifiers follow *Meskhidze et al.* [2005].

Cloud	Date	N_d (cm^{-3})	$\alpha_{l,avg}$
CS1	18 July	432 ± 112	0.62 ± 0.12
CS2	21 July	299 ± 116	0.75 ± 0.17
CS3	22 July	401 ± 129	0.76 ± 0.08
CS4	23 July	316 ± 113	0.54 ± 0.19
CS5	24 July	399 ± 152	0.76 ± 0.37
CS6	25 July	293 ± 112	0.29 ± 0.09
CS7	26 July	394 ± 162	0.53 ± 0.12
CS8	27 July	429 ± 134	0.50 ± 0.16

1, applied to both data sets), or for the fittings to equation (27) of Method 2 (which was only applied to the CRYSTAL-FACE cumulus). This was done to minimize the impact of cloud-base uncertainty in estimation of α_l and $(1 - \mu/\mu_c)$.

Figure 8 presents examples of typical LWC profiles observed for clouds in CRYSTAL-FACE and CSTRIPE. Also shown are the estimated $q_{l,ad}(z)$ and the fitted $q_l(z)$ for the cumulus case. The frequency distribution of α_l in the stratocumulus layers was observed to consist of a single mode with the peak very close to the mean value (inset of Figure 8a). In cumulus clouds, the distribution was much broader, characterized by frequent mixing and relatively infrequent adiabatic parcels. Tables 4 and 5 summarize the observed and inferred parameters for all the clouds included in this study.

4.5 Parameterization evaluation

Prediction of CDNC with physically based parameterizations such as FN05 or BN07 requires input from observations of the conditions under which activation takes place. This input consist on below-cloud thermodynamic data (pressure and temperature), aerosol size distribution and chemical composition, updraft velocity, and in the case of

Table 5: Cloud average cloud droplet number concentration (N_d), dilution ratio ($\alpha_{l,avg}$) and $(1 - \mu/\mu_c)$ (estimated with Method 2) for the CRYSTAL-FACE clouds considered in this study. Uncertainties for each parameter correspond to one standard deviation from the mean. Cloud identifiers follow *Meskhidze et al.* [2005].

Cloud	N_d (cm^{-3})	$\alpha_{l,avg}$	$(1 - \mu/\mu_c)$
H04-1	568 ± 222	0.71 ± 0.38	1.00
H04-2	617 ± 293	0.59 ± 0.36	1.00
H04-3	377 ± 79	0.57 ± 0.27	0.51
C06-1	207 ± 101	0.39 ± 0.33	0.60
C06-2	250 ± 117	0.33 ± 0.28	0.64
C06-3	274 ± 154	0.29 ± 0.23	0.73
C08-1	766 ± 420	0.31 ± 0.23	0.33
C08-2	586 ± 325	0.27 ± 0.21	0.42
C10-1	1158 ± 681	0.43 ± 0.44	0.43
C11-1	1147 ± 517	0.38 ± 0.24	0.68
C11-2	1745 ± 1129	0.62 ± 0.69	1.00
C12-1	305 ± 154	0.31 ± 0.24	0.54
C12-2	349 ± 177	0.33 ± 0.25	0.36
C16-1	219 ± 96	0.53 ± 0.39	1.00
C16-2	197 ± 93	0.44 ± 0.38	0.64
C17-1	325 ± 140	0.63 ± 1.11	1.00
C17-2	262 ± 130	0.36 ± 0.33	0.38
C17-3	284 ± 189	0.37 ± 0.35	1.00

BN07, the entrainment parameter $(1-\mu/\mu_c)$. The aerosol size distributions were fitted to four-mode lognormal distributions, assuming a composition of pure ammonium sulfate *Meskhidze et al.* [2005]. Following one of the methods suggested in *Meskhidze et al.* [2005], a probability density function (PDF) of updraft velocities, $p(w)$, constructed from the turbulence probe measurements in the stratocumulus decks was used to predict an average $N_d = \frac{\int_0^\infty wp(w)N_e(w)\mathrm{d}w}{\int_0^\infty wp(w)\mathrm{d}w}$, where $N_e(w)$ is the CDNC predicted with BN07 for the updraft$w$. A single updraft velocity (equal to the average updraft at cloud base) was used in the calculation of CDNC for CRYSTAL-FACE cumulus clouds. Finally, we also compared BN07 against the *Leaitch et al.* [1996] statistical correlation (given by $N_e = 0.1N_{ad}^{1.27}$), using FN05 to predict N_{ad}.

4.6 Analysis and discussion of results

For some of the CSTRIPE stratocumulus cloud layers, LWC exhibited significant deviations from adiabatic values; this however did not occur frequently enough to strongly impact CDNC. Figure 9a presents the predicted adiabatic CDNC against the cloud-scale average observed CDNC. No significant bias was observed (relative error of 4.2 ± 19%), and most of the 8 stratocumulus decks sampled were predicted within the ±20% uncertainty of the FSSP measurements. Conversely, applying BN07 with Method 1 (Figure 9b) exhibits modest underprediction of CDNC, with a relative error of $-15 \pm 17\%$. The vertical error bars were estimated as the variance in CDNC expected from the variability in vertical velocity, i.e., $\sigma^2 = \int wp(w)(N_d(w) - N_d)^2\mathrm{d}w / \int wp(w)\mathrm{d}w$.

When the adiabatic CDNC was compared to the cloud-scale average CDNC for the CRYSTAL-FACE cumulus clouds, a significant overprediction $(31 \pm 39\%)$ of CDNC was observed (Figure 10a). Application of BN07 substantially improves the predictions, with an average error of $-3.5 \pm 23\%$, using $(1-\mu/\mu_c)$ calculated from Method

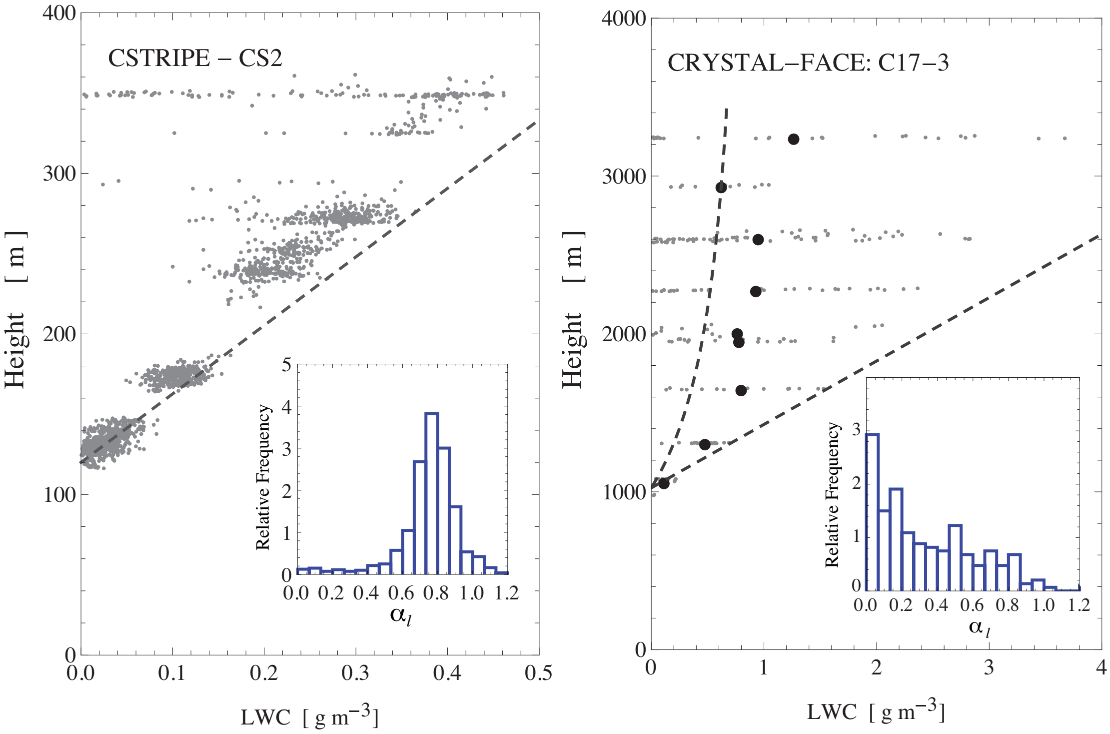

Figure 8: Typical liquid water content profiles observed during the CSTRIPE and CRYSTAL-FACE campaigns for (a) Stratocumulus deck (CS2), and, (b) Cumulus cloud (C17-3). Dashed straight lines correspond to adiabatic liquid water profile $q_{l,ad}(z)$. For the cumulus case (right panel), the curved dashed line is the Equation (27) fit to the observed 1Hz $q_l(z)$ (gray dots). Black dots are the transect average $q_l(z)$. The inset in each figure is the relative frequency distribution of α_l.

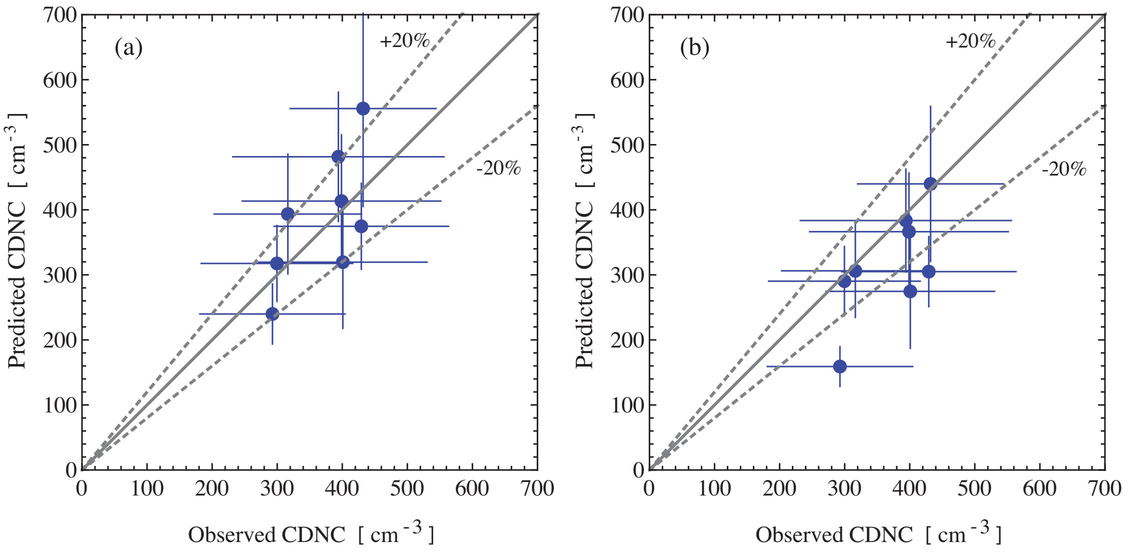

Figure 9: Comparison between observed cloud-scale average CDNC and predicted CDNC for CSTRIPE clouds with (a) FN05 parameterization and, (b) BN07 parameterization with $(1-\mu/\mu_c)$ estimated as the cloud average α_l (Method 1). Horizontal error bars represent one standard deviation of 1Hz FSSP data. Vertical error bars are one standard deviation in predicted CDNC, as calculated from the observed PDF of updraft velocities.

1 (Figure 10a). If Method 2 is used, the relative error between predictions and observations is equal to $14 \pm 31\%$. For a comparison with observations assuming inhomogeneous entrainment (IH), in which all the liquid water depletion (from the adiabatic expected values) is attributed to reduction of the total CDNC, i.e., $N_d \approx \alpha_{l,avg} N_{ad}$, CDNC was significantly underpredicted, on average by $-45 \pm 15\%$. Compared to the statistical approach of *Leaitch et al.* [1996], BN07 provided a much better representation of cloud-scale average CDNC, as the former underpredicted N_d by -24% for CRYSTAL-FACE and $-45\% \pm 13\%$ for CSTRIPE clouds.

Following *Burnet and Brenguier* [2006], the volume mean diameters, D_v, and CDNC derived from the 1Hz FSSP measurements were analyzed with their proposed D_v-N_d diagram to establish the extent to which the data follow a clear preferential type of mixing (either homogeneous or inhomogeneous). The data from the CSTRIPE stratocumulus tended to align along the constant α_l lines (consistent with the observed

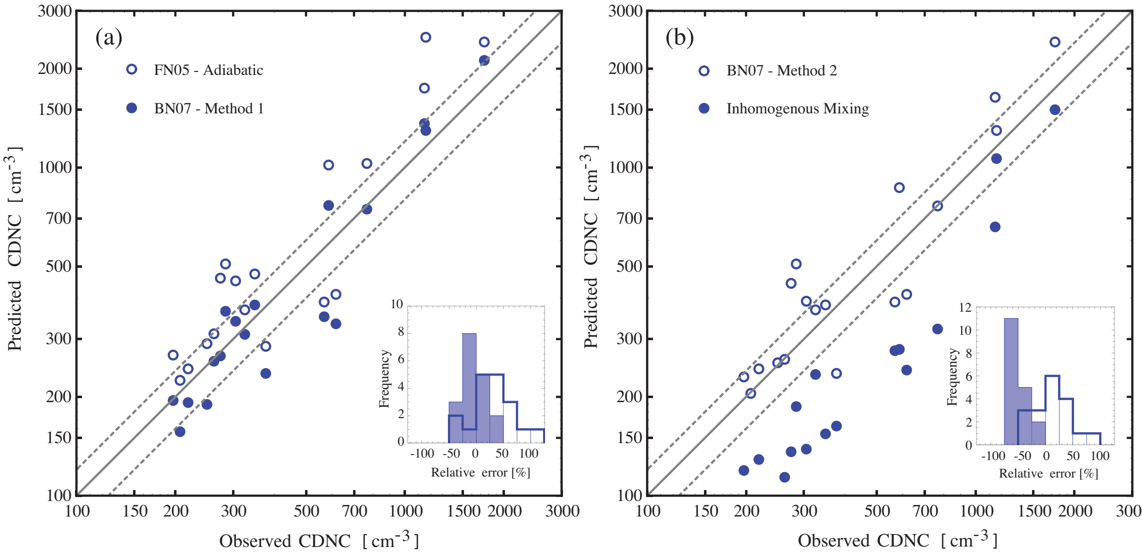

Figure 10: Comparison between cloud-average observed CDNC and predicted CDNC for 18 clouds sampled during CRYSTAL-FACE. Shown are predictions of CDNC using (a) FN05 and BN07 with $(1-\mu/\mu_c)$ estimated as the column average α_l (Method 1), and, (b) BN07 parameterization with $(1-\mu/\mu_c)$ estimated from Method 2, and IH scenario where $N_d \approx (\alpha_{l,avg})N_{ad}$. The insets are the frequency histograms for the relative error between predictions and observations.

frequency distributions showed in Figure 8 and $\alpha_{l,avg}$ presented in Table 4), while the CRYSTAL-FACE cumulus data points spanned the entire thermodynamically allowed space in the diagram, not exhibiting any specific trend (not shown). Since this study is concerned only with cloud-scale averages of CDNC, $\alpha_{l,avg}$ inferred from the observations expresses a convolution of homogeneous and inhomogeneous mixing across multiple scales.

4.6.1 CSTRIPE data

The entrainment and mixing process in the cloud-topped marine boundary layer is highly concentrated in the vicinity of the overlaying inversion, away from the activation zones near cloud base. Generally, the most dilute parcels are distributed in the upper part of the cloud adjacent to the temperature inversion, where they are exposed to cloud top entrainment, and represent a relatively small fraction of the cloudy air mass volume (Figure 8a). Therefore, the good agreement between observed cloud averaged CDNC with the adiabatic parameterization (Figure 9a) is not surprising. Furthermore, since the marine boundary layer is generally well mixed, and the cloud base for all the cases occurred between 150 and 300 m above sea level, the below-cloud layer was near saturation; thus minimizing entrainment effects near cloud base.

4.6.2 CRYSTAL-FACE data

The small and moderately-sized cumulus clouds sampled during the CRYSTAL-FACE campaign were observed to have highly diluted parcels throughout the cloud column (Figure 8b). This is consistent with the model of clouds growing in a dryer environment, with stronger vortical motions that engulf cloud-free air. Contrary to the marine stratocumulus clouds of the CSTRIPE campaign, a strong correlation between CDNC and α_l is observed. Since entrainment is more likely to deplete the CDNC throughout the entire cloud column in a cumulus cloud, significant overprediction of CDNC with the adiabatic parameterization is expected (as the adiabatically predicted CDNC represents an upper bound on the expected CDNC).

As discussed in section 4.3.3, agreement between predicted and observed CDNC for the CRYSTAL-FACE cumuli using BN07 is expected if the observed CDNC results from a balance between the two extremes of mixing. The assumption that cloud-scale averaged CDNC is equal to the adiabatically predicted value, N_{ad}, constitutes an upper limit and most likely is an overestimate of N_d (because of neglect of the diluting effect of entrainment and mixing), and the inhomogeneous mixing limit is unlikely to be representative of cloud-scale averages of CDNC. This is confirmed by the closure calculations, as N_{ad} overpredicts the observed CDNC by 31% (Figure 9a), and $\alpha_{l,avg}N_{ad}$ underestimates CDNC by 45% (Figure 9b).

Figure 10 supports the inequalities presented in Equation 28, since the respective biases of both methods are much smaller than for both the IH mixing and the adiabatic scenario. It is also possible that the overestimation of μ/μ_c with Method

1 partially compensates for increased entrainment and mixing at cloud top (unaccounted for under the assumption of constant μ used in Equation 3), explaining the better closure when this method is employed. The simplified approach presented here does not include a detailed analysis of the nature of the entrainment process itself, but it appears capable of effectively correcting the overprediction of the average CDNC in ambient clouds when N_d is assumed to be equal to the number of adiabatically activated droplets. The results presented here are also consistent with other observations of microphysical properties at the cloud-scale [*Peng et al.*, 2002].

4.7 Conclusions

Cloud droplet number concentration predicted with the BN07 activation parameterization was evaluated against measurements of CDNC in cumulus and stratocumulus clouds sampled during the CSTRIPE and CRYSTAL-FACE campaigns. It was shown that BN07 performed better than adiabatically predicted CDNC (with FN05) for the cloud-averaged CDNC in cumulus clouds, correcting a systematic overprediction bias of 31%. In stratocumulus clouds, inclusion of entrainment effects did not further improve the CDNC closure; this is consistent with the conceptual model of a well-mixed boundary layer capped by a strong temperature inversion. In all cases considered, BN07 compared favorably against a statistical correlation developed from observations to treat entrainment effects on droplet number.

Different methods to estimate the impact of entrainment and mixing on the CDNC were explored, finding that BN07 predicts CDNC within the limits imposed by the inhomogeneous mixing lower limit and the adiabatic upper limit. The agreement between observed and predicted CDNC when entrainment effects are included (by setting $(1 - \mu/\mu_c)$ equal to the average dilution ratio, α_l) suggest that the simple scheme presented here is a possible way to effectively account for the impact of entrainment on average cloud microphysical properties.

An evaluation such as that in the present study should be repeated with other field campaign data, especially under clean conditions (where the dependence of N_d on w could be substantially different from the conditions considered here). Nevertheless, the results presented here strongly support that BN07 can correct an important source of CDNC overprediction bias in large-scale atmospheric models, and are in good agreement with observational studies of continental cumulus.

4.8 Acknowledgments

We acknowledge support from NASA-ACMAP, NSF-CAREER and ONR (grant N00014−10 − 1 − 0200). We also thank Dr. Donifan Barahona, Prof. Jeff Snider, and two anonymous reviewers for comments that improved the manuscript.

CHAPTER V

UNDERSTANDING THE CONTRIBUTIONS OF AEROSOL PROPERTIES AND PARAMETERIZATION DISCREPANCIES TO DROPLET NUMBER VARIABILITY IN A GLOBAL CLIMATE MODEL

5.1 Summary

Aerosol indirect effects in climate models strongly depend on the representation of the aerosol activation process. In this paper, we assess the process level differences across activation parameterizations that contribute to droplet number uncertainty by using the adjoint of the *Abdul-Razzak and Ghan* [2000] and *Fountoukis and Nenes* [2005] droplet activation parameterizations in the framework of the Community Atmospheric Model version 5.1 (CAM5.1). The information from the sensitivities is used to: i.) unravel the spatially resolved contribution from aerosol number, mass, and chemical composition to changes in N_d between present day and pre-industrial simulations; ii.) identify the key variables responsible for the differences in N_d fields and aerosol indirect effect estimates when different activation schemes are used within the same modeling framework. The sensitivities are computed online at minimal computational cost. Changes in aerosol number and aerosol mass concentrations were found to contribute to N_d differences much more strongly than chemical composition effects. The main sources of discrepancy between the activation parameterization considered were the treatment of the water uptake by coarse mode particles, and the sensitivity of the parameterized N_d accumulation mode aerosol geometric mean

---

This chapter appears as reference *Morales and Nenes* [Submitted] diameter. These two factors explain the different predictions of N_d over land and over oceans when these parameterizations are employed. Discrepancies in the sensitivity to aerosol size are responsible for an exaggerated response to aerosol volume changes over heavily polluted regions. Because these regions are collocated with areas of deep clouds their impact on short wave cloud forcing is amplified through liquid water path changes. With a simple application of the adjoint-sensitivities it was shown the importance of primary organic matter emissions in controlling the droplet number concentration changes in several areas. The same framework is also utilized to efficiently explore droplet number uncertainty attributable to hygroscopicity parameter of organic aerosol (primary and secondary). Comparisons between the parameterization-derived sensitivities of droplet number against predictions with detailed numerical simulations of the activation process were performed to validate the physical consistency of the adjoint sensitivities.

5.2 Introduction

The impact of atmospheric aerosols on the energy budget of the Earth and on cloud microphysical properties is a major contributor to climate prediction uncertainty and estimates of anthropogenic climate change [*Intergovernmental Panel on Climate Change*, 2007]. Due in part to the computational complexity of the models used for climate projections, quantification of uncertainty has often been reported in terms of model diversity [e.g., *Kinne et al.*, 2006; *Quaas et al.*, 2009; *Myhre et al.*, 2013], rather than by analyzing the uncertainty associated with specific parameters and processes. This approach, although useful, does not always allows to identify the process level differences causing these discrepancies. As a result the identification of the specific parameters and processes that contribute the most to the uncertainty in simulated aerosol-cloud interactions remains elusive.

Atmospheric aerosols can influence the radiative properties of the atmosphere by directly scattering and absorbing light (*aerosol direct effect*) or indirectly by modifying the optical properties of clouds by serving as nuclei for cloud droplets and ice crystals. The latter is known as *aerosol indirect effect* (AIE). In order to make quantitative estimates of AIE in global circulation models it is therefore necessary to realistically represent both, the availability of atmospheric aerosol that can act as cloud condensation nuclei (CCN), as well as the activation process by which a subset of CCN activate into cloud droplets.

Because the ability of an aerosol particle to act as a CCN depends strongly on its size and chemical composition [e.g., *McFiggans et al.*, 2006], accurately simulating the availability of CCN requires knowledge of the aerosol size distribution and the mixing state of the different species in the aerosol phase. For this reason, state-of-the-art climate models include either modal or sectional representations of aerosol size distributions, and have conservation equations for the number and mass concentration for the main aerosol species, including sulfate, sea salt, dust, and carbonaceous aerosols [e.g., *Stier et al.*, 2005; *Dentener et al.*, 2011; *Liu et al.*, 2012]. Inclusion of detailed aerosol modules, which allows a more physically consistent description of atmospheric aerosols, has increased the computational burden of climate models and introduced more, sometimes uncertain, parameters to describe the extra processes. For instance, aerosol species that are emitted directly, such as black carbon (BC), primary organic matter (POM) or sulfate aerosol, for which emission inventories provide their mass fluxes to the atmosphere, require information on the size distribution of the emitted particles. The assumed distribution, which is often uncertain or unknown, largely controls the number concentration of emitted particles, playing an important role on the simulated CCN concentrations [e.g., *Adams and Seinfeld*, 2003; *Pierce and Adams*, 2009].

The incorporation of carbonaceous aerosols and their inclusion in AIE estimates has been an important part of GCM development. Owing to the plethora of compounds involved in the make up of organic aerosols, the parameters describing their hygroscopicity are less well constrained than those of inorganic aerosol species [*Petters and Kreidenweis*, 2007]. Uncertainty in these parameters can affect AIE estimates, since organic species are known to contribute an important fraction of atmospheric aerosols and can affect the number concentration and hygroscopicity of accumulation mode aerosol (e.g, *Novakov and Penner* [1993]; *Jimenez et al.* [2009]). Overall, the apportionment of uncertainty is sometimes obscured by the increased complexity of climate models with detailed aerosol-cloud interactions.

A variety of methods to assess the problem of uncertainty in CCN number have been employed. Evaluation of the impact of parametric uncertainty in climate model simulations has been typically done by performing model integrations with one parametric value perturbed to then do a finite difference computation. Such approach has been used, for example, to quantify the sensitivity of CCN and cloud droplet number (CDNC) to the assumed hygroscopicity of secondary organic aerosol [*Liu and Wang*, 2010]. Many studies have used similar approaches to asses the importance of the assumed split between primary and secondary organic emissions (e.g, *Trivitayanurak and Adams* [2013]).

Statistical emulators of chemical transport models with detailed aerosol microphysics [e.g., *Lee et al.*, 2012a, 2013] have been used to establish a hierarchy of parameters based on their impact on CCN number uncertainty, using a Gaussian multivariate approach [*Lee et al.*, 2011]. These studies have shown that parameters related with emissions carry a large proportion of the uncertainty in CCN concentrations [*Lee et al.*, 2013], since these parameters have a direct impact on the CCN population. The statistical approach has also been used in a GCM framework to evaluate the impact of aerosol parameter in the radiative budget at the top of the atmosphere [*Zhao et al.*, 2013]. These works have pointed out to the importance of accurate emission inventories, but also to the parameters describing emission size distributions and the hygroscopicity of organic species. Nevertheless, this approach requires a large number of model integrations to build an accurate emulator within a given parameter space, with the number of runs growing together with the dimensionality of the parameter space.

However, the availability of CCN alone is not enough to describe the link between aerosol properties and cloud microphysics, and is therefore insufficient to compute AIE estimates. The process of aerosol activation, is a dynamical process that involves the competition between the sink of water vapor (represented by the CCN availability) as well as the dynamical forcing provided by cloud-scale vertical motions. Both these factors are necessary to compute the cloud droplet number concentration. Several physically-based activation schemes are used in climate models [e.g., *Abdul-Razzak and Ghan*, 2000; *Fountoukis and Nenes*, 2005; *Ming et al.*, 2006; *Shipway and Abel*, 2010]. These schemes require the knowledge of the CCN availability at a given water supersaturation s, which can be determined from the aerosol size distribution and chemical composition. Different activation parameterization implemented in the same modeling framework can produce important differences in the radiative forcing even when the physics they represent are very similar [*Ghan et al.*, 2011]. The uncertainty associated with the activation scheme used should also be evaluated and quantified.

The adjoint sensitivity approach is an efficient method to investigate process sensitivity to input parameters in complex models. The method involves the construction of numerical routines that compute, with analytical precision, the first-order derivative of a processes parameterization with respect to a set of input variables. The computation of sensitivities is achieved without the need of invoking the subroutine several times to perform finite difference computations. The adjoint-sensitivity approach has been recently used in different applications involving aerosol activation schemes. *Karydis et al.* [2012a] used the adjoint approach to compute the impact of aerosol precursor emissions on cloud droplet number (CDNC) over North America using the GEOS-Chem chemical transport model. *Saide et al.* [2012] used the adjoint of an activation scheme in the WRF model, coupled with satellite derived retrievals of CDNC to infer aerosol concentrations below clouds, inaccessible to satellite sensors. To our knowledge, this tool has yet to be implemented in a GCM framework.

Here we report the implementation of the adjoint sensitivities of commonly used, physically based activation parameterizations in the Community Atmosphere Model, version 5.1 (CAM5.1). We compare the sensitivity of droplet number to aerosol characteristics to determine the variables responsible for the discrepancies in CDNC among the parameterizations considered here. The information provided by first-order derivatives is also used to elucidate the spatially-resolved impact of parametric uncertainty, illustrated here with the hygroscopicity of secondary and primary organic aerosol.

The paper is organized as follows. In the first section, we describe the implementation of the adjoint sensitivities in the CAM-5.1 AGCM. The second section studies the different responses of the FN-adjoint and ARG-adjoint under identical model conditions, and identifies the underlaying cause for their divergent response. The final two sections are devoted to the application of the adjoint in the quantification or organic aerosol parametric uncertainty, by exploring the adjoint sensitivity to the assumed hygroscopicity of SOA, POM and BC.

5.3 Model Framework Description

5.3.1 AGCM simulations with CAM5.1

Simulations were performed with the Community Atmosphere Model version 5.1 (CAM5.1) atmospheric general circulation model (AGCM). CAM is the atmospheric component of the Community Earth System Model (CESM1.0), and is described in full detail in (http://www.cesm.ucar.edu/models /cesm1.0/cam/). Here we focus on the description of the physical processes most directly involved in the aerosol-cloud linkage.

The aerosol module of CAM5.1, which provides the aerosol characteristics necessary for the calculation of droplet activation, is the 3-mode version of the modal aerosol module (MAM3) [*Liu et al.*, 2012]. This aerosol module considers eight aerosol species (sulfate, ammonium, nitrate, primary organic matter (POM), secondary organic aerosol (SOA), black carbon, sea salt, and dust) partitioned into three log-normally distributed modes (accumulation, Aitken, and coarse modes). The species in each mode are assumed to be internally mixed. The geometric standard deviation σ_{gi} of each mode is prescribed, but aerosol number concentration (n_{ai}) and mode diameter (d_{gi}) for each mode are allowed to vary to accommodate the corresponding mass. Characteristics of the MAM3 aerosol are summarized in Table (6). The cloud-scale vertical velocity used to drive the activation process is computed from the turbulent kinetic energy, TKE, as $w = \sqrt{\frac{2}{3}TKE}$. Lower and upper bounds of 0.2 ms^{-1} and 10 ms^{-1} respectively are imposed on w. The aerosol direct and indirect effects using the default configuration of MAM3 have been studied in detail by *Ghan et al.* [2012]. The aerosol in CAM interacts with stratiform clouds using the double moment cloud microphysics scheme of *Morrison and Gettelman* [2008]. The aerosol activation process is the source term for the gridbox CDNC equation balance. The fraction of aerosols activated into cloud droplets can be removed by wet scavenging or regenerated to the interstitial aerosol population after cloud evaporation.

Table 6: Aerosol species and size distribution parameters in MAM3 used as input for the cloud droplet number activation parameterizations. d_{g_i}, is the geometric mean diameter (μm), and σ_{gi} the geometric standard deviation for each mode "i". *Liu et al.* [2012]

Aerosol Mode	Aerosol Species	Hygroscopicity κ_α	Density (g cm^{-3})	σ_{g_i}	d_{g_i}-range (μm)
Accumulation	Sulfate	0.507	1.77	1.8	0.053 - 0.44
	POM	0.10	1.00		
	SOA	0.14	1.00		
	Black Carbon	1×10^{-10}	1.70		
	Sea Salt	1.160	1.90		
	Dust	0.068	2.60		
Aitken	Sulfate	0.507	1.77	1.6	0.0087 - 0.052
	SOA	0.14	1.00		
	Sea Salt	1.160	1.90		
Coarse	Sulfate	0.507	1.77	1.8	1.0 - 4.0
	Sea Salt	1.160	1.90		
	Dust	0.068	2.60		

The simulation results reported here were obtained by integrating the model for a period of 6 years, using climatological sea surface temperature (SST) corresponding to year 2000. Greenhouse gases concentrations where also set to values corresponding to year 2000. Annual and seasonal averages correspond to the last 5 years of integration, with the first year discarded as spin-up. Simulations were performed with present day (year 2000) and pre-industrial (year 1850) emissions of aerosols, aerosol precursors, and atmospheric oxidants from the *Lamarque et al.* [2010] inventory. Injection heights and emission sizes follow *Dentener et al.* [2006]. To isolate the impact of aerosol load changes between present day and pre-industrial times, the concentration of greenhouse gases was maintained at present day levels.

5.3.2 Adjoint sensitivities of N_d to aerosol properties

We consider the sensitivity of N_d to a set of ten variables: the cloud-scale vertical velocity, w, aerosol number concentration per mode, n_{a_i}, the mode diameter, d_{g_i}, and the hygroscopicity parameter of each lognormal mode, κ_{a_i}. The hygroscopicity parameter accounts for the effect of the chemical composition in the water uptake ability of aerosol particles. Because each mode is assumed internally mixed, κ_{a_i} is the volume-weighted average of the assumed hygroscopicity parameter of each constituent species [*Petters and Kreidenweis*, 2007] (Table 6), i.e.,

$$\kappa_{a_i} = \sum_{\alpha \in i} v_{\alpha,i} \kappa_\alpha \tag{29}$$

where $v_{\alpha,i}$ is the volume fraction of species α in the ith-mode. Greek subindices will be used throughout the manuscript to indicate aerosol constituents, while latin subindices are reserved for aerosol modes. The adjoint sensitivity of these parameterizations was implemented such that each call to the activation routine produces N_d, together with the set of derivatives $\partial N_d / \partial \chi_j$, to each of the ten parameters χ_j. Since d_{g_i} is not an independent variable, but is computed from the volume (v_{a_i}) and number concentration of each mode (n_{a_i}), the adjoint sensitivities are expressed in terms of the independent variables v_{a_i} and n_{a_i} alone.

The parameterizations considered in this study include two within the ARG parameterization framework [*Abdul-Razzak and Ghan*, 2000; *Ghan et al.*, 2011], and two from within the FN parameterization framework [*Fountoukis and Nenes*, 2005; *Barahona et al.*, 2010a]. We used the default activation scheme used in CAM5.1, which is the ARG parameterization [*Abdul-Razzak and Ghan*, 2000], and a revised version, ARGα, that includes the effects of the mass accommodation coefficient in the condensation process [*Ghan et al.*, 2011]. Similarly, we used the FN activation scheme [*Fountoukis and Nenes*, 2005], and an updated version, FN-IL, that includes terms to better account for the water uptake by inertially limited CCN [*Barahona et al.*, 2010a]. These parameterizations are based on a similar set of physical principles and assumptions [*Ghan et al.*, 2011].

There are methodological differences in the calculation of the sensitivities for each parameterization framework. In the case of ARG, sensitivities can be computed analytically, as shown by *Rissman et al.* [2004], and is the approach used in this work (see Section 5.8). The FN parameterization uses instead a set of numerical routines to compute N_d, which prevents the use of explicit equations. Therefore, efficient computation of the sensitivities in the FN framework required the development of a corresponding adjoint code. For this, we implemented the newly developed adjoint sensitivity of the FN and FN-IL [*Karydis et al.*, 2012b], which uses automatic differentiation software to build the necessary subroutines.

5.4 Results

5.4.1 Overview of the Simulations

Among the activation parameterizations included in this study, ARGα, FN, and FN-IL, include the effect of non-continuum effects in the condensation process through an explicit dependence on the accommodation coefficient, α_c [*Pruppacher and Klett*, 1997]. For the simulations performed with those parameterizations the value of α_c was set equal to 0.1, which is within the observed range of α_c in various locations [*Raatikainen et al.*, 2013]. Simulations with the ARG parameterization are included as a reference, since this is the activation scheme used in the release version of CAM5.1. A summary of the model integrations performed is included in Table 7.

Annual mean values for radiation and cloud parameters are shown in Table 8. The strongest short wave cloud forcing difference between PD and PI simulations (ΔSWCF) is observed for simulations with ARGα. The larger ΔSWCF associated with ARGα is likely due to the large difference in the global mean liquid water path.

The annual mean in-cloud droplet number concentration, N_d, for the 5th model layer (930 hPa) are shown in Figure 11 for the present day simulation. This pressure level was chosen because it has the largest liquid cloud cover, and is representative of the results for the pressure levels in the column with liquid clouds. Figure 11 also

Table 7: Summary of simulations

Experiment ID	Activation Parameterization	Aerosol Emissions	Accommodation Coefficient
ARG-PD	*Abdul-Razzak and Ghan* [2000]	Year 2000	N/A
ARG-PD	*Abdul-Razzak and Ghan* [2000]	Year 1850	N/A
ARGα-PD	*Ghan et al.* [2011]	Year 2000	$\alpha_c = 0.1$
ARGα-PIa	*Ghan et al.* [2011]	Year 1850	$\alpha_c = 0.1$
FN-PD	*Fountoukis and Nenes* [2005]	Year 2000	$\alpha_c = 0.1$
FN-PIa	*Fountoukis and Nenes* [2005]	Year 1850	$\alpha_c = 0.1$
FN-IL-PD	*Barahona et al.* [2010a]	Year 2000	$\alpha_c = 0.1$
FN-IL-PIa	*Barahona et al.* [2010a]	Year 1850	$\alpha_c = 0.1$

shows the change in N_d between present day and pre-industrial simulations. These maps exhibit the expected patterns of increased CDNC over continental regions, with a particularly large increase in N_d over Southeast Asia. The marked decrease in CDNC over Southeast US, central South America, and North Australia has been observed in other studies, pointing to changes in biomass burning emissions as the cause [*Wang et al.*, 2011]. This feature arises from the emissions inventory used, in particular, the assumed size of the aerosol emitted, and has an important impact in both direct [e.g., *Lee et al.*, 2012b] and indirect effects [e.g., *Wang et al.*, 2011; *Bauer and Menon*, 2012].

The N_d fields in Figure 11 show also some noticeable differences across different parameterizations. Global mean N_d produced with ARGα is slightly larger than those for FN and FN-IL, but droplet number concentration over oceans show the opposite trend, being lower for FN and FN-IL compared to ARGα. For present-day aerosol emissions, simulations with ARGα have more numerous and smaller cloud droplets over land than simulations with FN or FN-IL. This difference is especially noticeable over the heavily polluted region of Southeast Asia. As a consequence, the annual mean cloud droplet effective radius, r_e, in ARGα-PD is 3.5% smaller over continents when compared to FN-PD, while the N_d is 10% larger over continents. This trend is

Table 8: Annual global mean for selected radiation parameters and cloud properties, namely: shortwave cloud forcing (SWCF), longwave cloud forcing (LWCF), liquid and ice water path (LWP and IWP respectively), total precipitation (PRECT), and column droplet number concentration (CDNUMC). The difference of these variables between PD and PI simulations, as well as for the total cloud forcing ΔCF= Δ(SWCF+LWCF), and the cloud top effective radius Δr_e

	ARG		ARGα		FN		FN-IL	
	PD	PI	PD	PI	PD	PI	PD	PI
SWCF (Wm^{-2})	-51.85	-49.86	-53.38	-51.13	-54.05	-52.00	-53.71	-51.70
LWCF (Wm^{-2})	24.15	23.80	24.13	23.79	24.18	23.82	24.18	23.76
LWP (gm^{-2})	44.38	40.73	47.26	42.82	47.77	43.57	47.37	43.45
IWP (gm^{-2})	17.81	17.76	17.68	17.65	17.74	17.55	17.74	17.55
PRECT (mm day^{-1})	2.96	2.98	2.97	2.99	2.97	2.99	2.97	2.99
CDNUMC (10^{10} m^{-2})	1.33	0.96	1.85	1.30	1.83	1.28	1.67	1.20
ΔSWCF (Wm^{-2})	-2.00		-2.24		-2.05		-2.01	
ΔCF (Wm^{-2})	-1.65		-1.90		-1.70		-1.60	
ΔCDNUMC (%)	38.6		42.6		42.7		39.0	
ΔLWP (%)	8.97		10.38		9.63		9.00	
Δr_e (%)	-2.2		-3.7		-4.1		-3.9	

reversed over oceanic regions, where the relative difference in r_e is 1% larger for ARGα and N_d is 15% smaller. The reason for this differences across parameterizations will be further discussed in Section 5.4.3.

5.4.2 Sensitivity of ARG and FN schemes in CAM

The sensitivities $\partial N_d/\partial \chi_j$ were computed at each time step during model integration, and annual mean in-cloud sensitivities summarized in Table 9. The spatial distribution of the annual mean in-cloud sensitivity of N_d to aerosol number and hygroscopicity parameter are shown in Figures 12 and 13, respectively.

Sensitivity of N_d for the Aitken mode to both n_{a_i} and κ_{a_i} is negligible, indicating that N_d is only weakly dependent on these parameters. This is expected, given that their size generally limits their contribution to the CCN concentration. Their size also limits the amount of water vapor they deplete during cloud formation, therefore

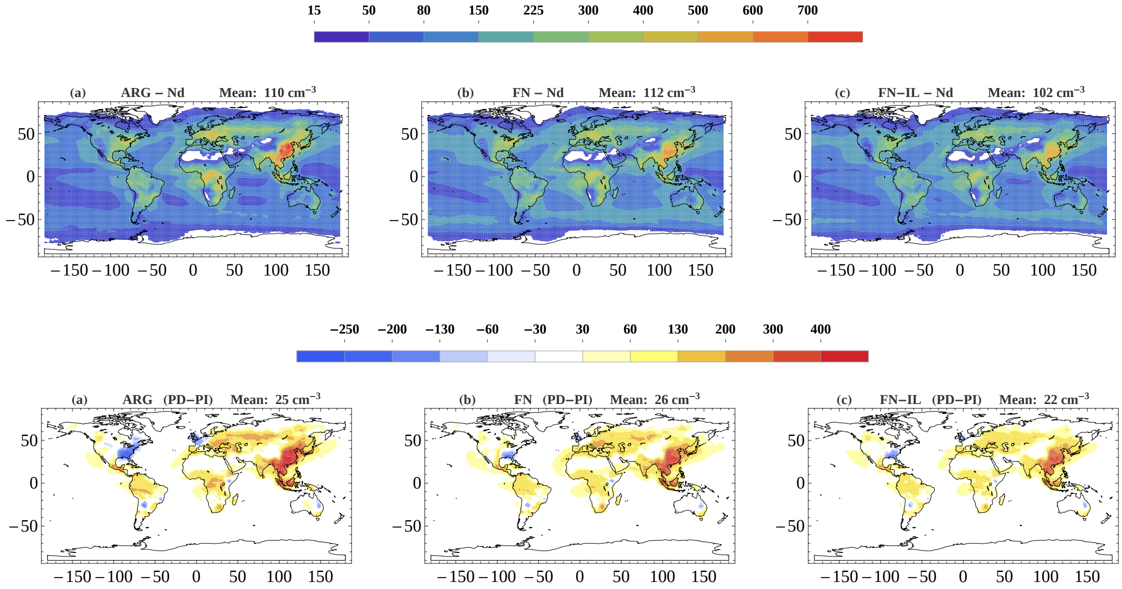

Figure 11: Annual mean in-cloud droplet number concentration, N_d (in cm^{-3}/cm^{-3}), at the 930 mb pressure level predicted for **(a)** ARGα-PD, **(b)** FN-PD, and **(c)** FN-IL-PD. The lower panels show the difference in (ΔN_d) between present day (PD) and pre-industrial emissions (PI)

only weakly impacting the maximum supersaturation. All the parameterizations considered consistently reflect this. The spatial distribution and magnitude of $\frac{\partial N_d}{\partial n_{a_i}}$ and $\frac{\partial N_d}{\partial \kappa_{a_i}}$ for accumulation mode aerosol are also in good agreement across parameterizations (Figure 12b, 12e, 12h, 12k). As expected, sensitivity of N_d to this population is strong and always positive, since they fall in the size range most appropriate for CCN-active particles.

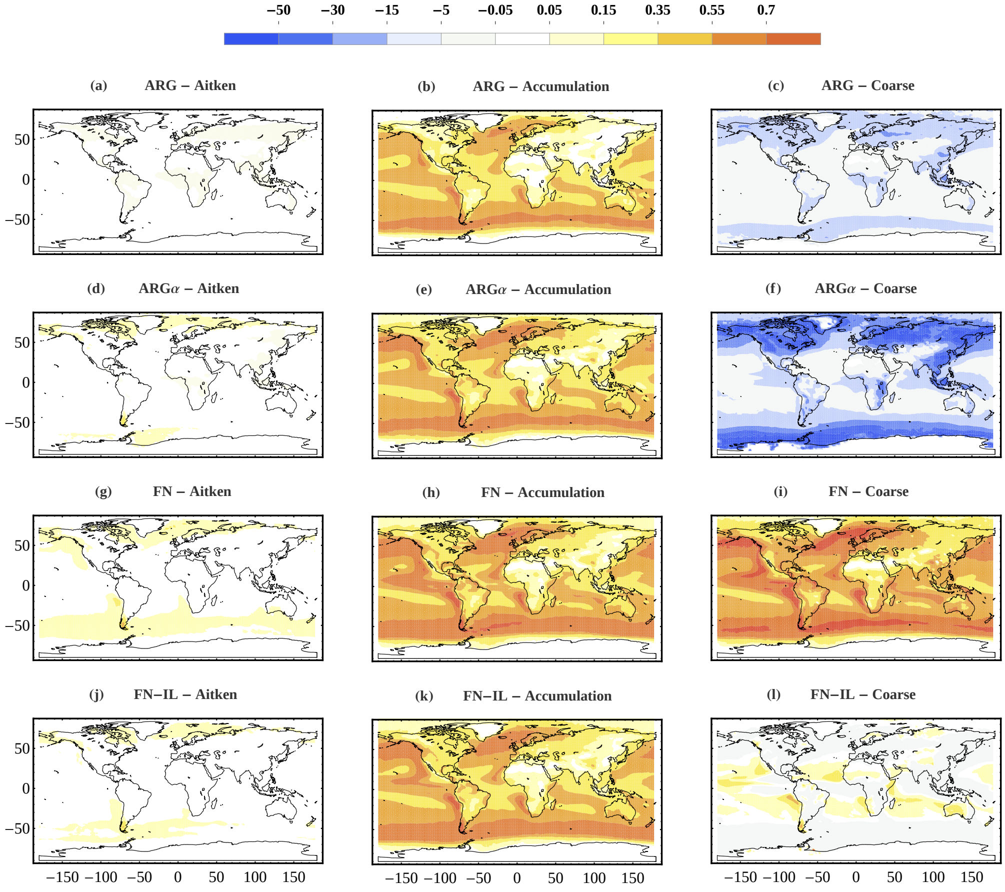

Figure 12: Annual mean sensitivity to aerosol number concentration $\partial N_d/\partial n_{a_i}$. **(a)-(c)** Aitken, Accumulation, and Coarse modes in the ARG-PD simulation, **(d)-(f)** ARGα-PD simulation, **(g)-(i)** FN-PD simulation, and **(j)-(l)** FN-IL-PD simulation .

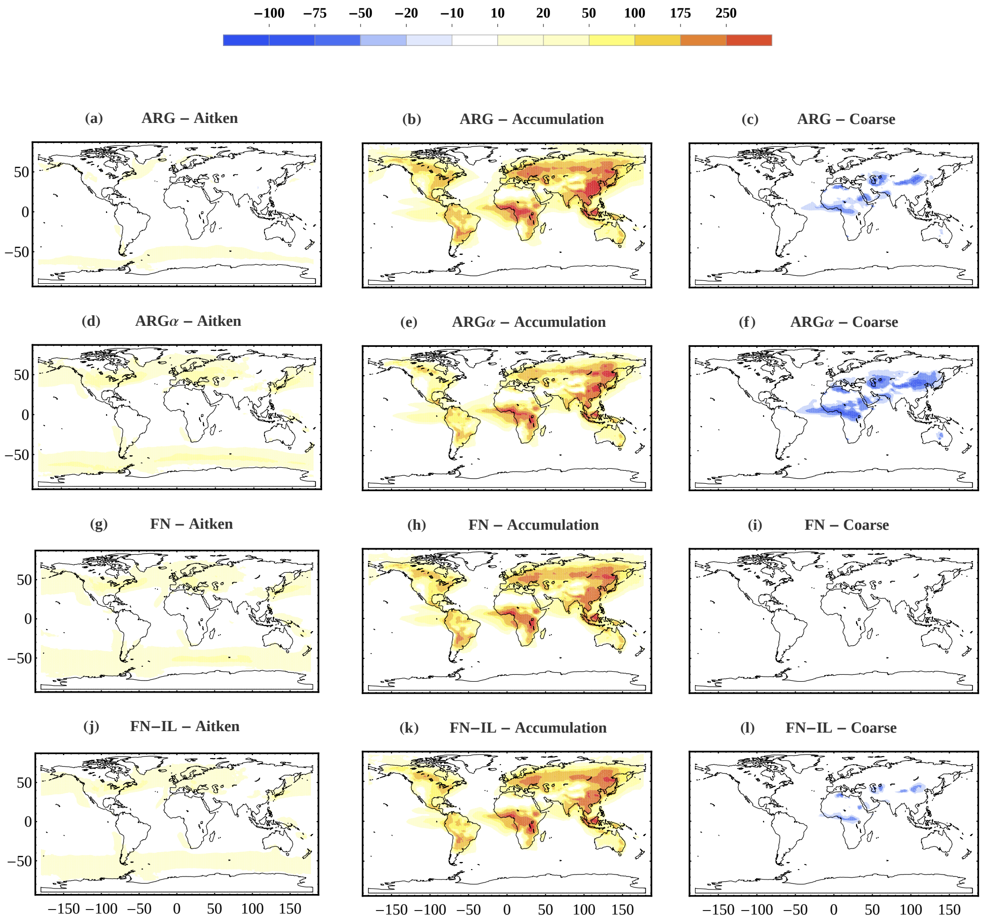

Figure 13: Same as Figure (12) but for aerosol hygroscopicity $\partial N_d/\partial \kappa_{a_i}$ (in cm^{-3})

.

Table 9: Annual mean sensitivities computed for the PD simulations. Fields are reported for the 930 mb pressure level

Sensitivity	Aerosol Mode	ARG-PD			FN-PD			FN-IL-PD		
		Land	Ocean	Global	Land	Ocean	Global	Land	Ocean	Global
$\partial N_d/\partial n_{ai}$ (–)	Aitken	−0.009	−0.002	−0.004	0.019	0.037	0.031	0.015	0.020	0.018
	Accumulation	0.26	0.43	0.38	0.27	0.49	0.43	0.24	0.46	0.40
	Coarse	−26.7	−10.6	−15.3	0.40	0.54	0.50	−0.31	−0.15	−0.20
$\mathrm{d}N_d/\mathrm{d}n_a$ (–)	–	0.19	0.18	0.18	0.22	0.31	0.28	0.19	0.25	0.24
$\partial N_d/\partial \kappa_{ai}$ (cm^{-3})	Aitken	9.06	8.19	7.92	8.41	10.62	9.96	7.29	9.23	8.66
	Accumulation	67.6	6.68	21.0	81.4	9.49	30.8	78.6	8.55	29.15
	Coarse	−9.0	−2.4	−4.2	0.05	0.001	0.016	−2.03	−0.74	−1.11
$\partial N_d/\partial d_{gi}$ ($\mathrm{cm}^{-3}\mu\mathrm{m}^{-1}$)	Aitken	433.7	545.7	512.7	284.8	561.2	479.2	249.8	507.7	431.9
	Accumulation	1125	167.3	449.5	482.8	78.0	198.1	466.8	65.86	183.7
	Coarse	0.0006	0.00008	0.0002	0.008	0.0005	0.003	−0.75	−1.43	−1.23
$\partial N_d/\partial w$ ($\mathrm{cm}^{-3}\mathrm{m}^{-1}s$)	–	194.5	63.7	102.3	185.8	65.90	101.2	175.2	69.07	100.3

Discrepancies between ARGα, FN, and FN-IL in the sensitivity of N_d to coarse mode aerosol number and hygroscopicity are evident (Figures 12 and 13), not only showing different magnitudes but in some cases, opposite signs. These large discrepancies arise in the treatment adopted in each scheme to describe the depletion of water vapor by the largest particles in the aerosol population.

From Table 9 it is clear that ARGα has the strongest negative sensitivity to coarse mode aerosol characteristics. The large negative response in the ARGα implies that the overall impact on N_d from the strong depletion of supersaturation by coarse mode particles (which depresses s_{max}) largely offsets any contribution from coarse particles to the CCN population. On the other extreme, FN appears to strongly underestimate the water vapor depletion from coarse mode particles, therefore changes to coarse mode aerosol do not impact s_{max} in a measurable way, while their large size and low s_c ensures their contribution to the CCN population. This is reflected in the sensitivity of FN to coarse mode aerosol number, which is positive, and slightly larger in magnitude than for the accumulation mode. An intermediate response is found when the FN-IL is used instead. This parameterization, which differs from FN in the treatment of the inertially limited CCN population, exhibits an often negative response to coarse mode aerosol, indicating a more physically consistent treatment of the water vapor depletion by this aerosol population. Careful validation of this sensitivities was performed by comparing them to detailed numerical simulations of the activation process (Section 5.9). It was found that, on average, the sensitivity to coarse mode aerosol is better captured by the FN-IL parameterization of all formulations considered.

The same arguments can be extended to the sensitivity of N_d to κ_{a_i} and d_{g_i} of coarse mode particles. The weak water vapor depletion of coarse particles in FN leads to a negligible impact of the coarse mode κ_{a_i} and d_{g_i} on N_d (Table 9). Both, ARGα and FN-IL, with a stronger depletion by coarse mode particles, are more sensitive to increases in the water uptake ability of this aerosol population. In both cases, a marked negative response is observed, in particular in areas where the coarse mode is dominated by dust, which has a very low hygroscopicity. The supersaturation depletion effect of coarse mode particles and their impact on N_d has been observed and discussed previously [e.g., *Ghan et al.*, 1998] in the framework of parcel model simulations, but the impact on global distributions of N_d had not been addressed before.

Table 9 also indicates a marked discrepancy in the sensitivity of N_d to geometric mean diameter, $\partial N_d/\partial d_{g_i}$, between ARG$\alpha$ and FN or FN-IL. In particular, for Aitken and accumulation mode this sensitivity is higher for ARGα by a factor of 2. Since d_{g_i} is derived from the volume and the number concentration for each mode, the derivatives of N_d with respect to v_{a_i} are given by

$$\frac{\partial N_d}{\partial v_{a_i}} = \frac{d_{g_i}}{3v_{a_i}}\frac{\partial N_d}{\partial d_{g_i}} \tag{30}$$

therefore, differences in the sensitivity to aerosol size directly impacts the sensitivity to aerosol volume.

The overall sensitivity to aerosol number, dN_d/dn_a, often used measure of the strength of the AIE, [e.g., *Quaas et al.*, 2009], is also strongly affected by the above enhanced response to coarse mode particles. We define this quantity as the sensitivity of N_d to an overall increase in aerosol number that preserves the shape of the aerosol size distribution, i.e.,

$$\frac{dN_d}{dn_a} = \sum_i \frac{\partial N_d}{\partial n_{a_i}}\frac{n_{a_i}}{|n_a|} \tag{31}$$

where, $|n_a|^2 = \sum_i n_{a_i}^2$. The values of dN_d/dn_a from the simulations indicate that aerosol activation over the vast majority of oceanic regions occurs under the "aerosol limited" regime identified by *Reutter et al.* [2009], mainly due to relatively low aerosol loads.

The sensitivity from Equation (31) is larger in the FN-PD experiment, with a global mean of 0.28, than for simulations performed with the ARG parameterization, which have a global mean dN_d/dn_a of 0.19, indicating a higher sensitivity to aerosol perturbations. This difference across parameterizations is largely explained by the negative sensitivity of ARG to coarse mode particles, which strongly dampens the value of dN_d/dn_a over marine environments (Table 9). This highlights the diverse contribution of each aerosol mode to N_d, namely, the crucial importance of accumulation and coarse mode in determining the magnitude of dN_d/dn_a.

The higher sensitivity to aerosol number as expressed by Equation (31) suggest that AIE should be stronger for simulations with FN and FN-IL compared to ARGα. However, a number of fields in Table 8, including droplet number concentration and short wave cloud forcing are larger for ARGα than for FN or FN-IL. This apparent inconsistency is resolved by realizing that dN_d/dn_a does not capture the total sensitivity of CDNC to aerosol changes. In actuality, there are processes that cause an increase in N_d without involving a direct change in aerosol number concentration. For instance, condensation of sulfate or SOA on an aerosol population will cause the hygroscopicity and the volume of the aerosol to increase, without significantly changing n_a. This suggests that the use of equation (31) as a metric for the strength of aerosol cloud interactions does not capture the concurrent changes in CCN activity that are associated with increased hygroscopicity and size. In this regard, the different value of these sensitivities are important in understanding the simulated N_d fields with different parameterizations.

5.4.3 Unraveling mass, number, and chemical composition contributions to N_d

The increase in aerosol emissions between PD and PI times has not only changed the total mass and number of atmospheric aerosol, but has also modified its chemical composition. Due to the heterogeneity of aerosol precursor sources these changes in aerosol load and chemical composition have a marked regional imprint. For instance, the marked increase in anthropogenic sulfate aerosol over most continental areas of the northern hemisphere produces not only a much larger number concentration of aerosols, but also promotes the hygroscopicity of continental aerosol after mixing with the background aerosol (composed mostly of POM, SOA, BC, and dust). The opposite trend is observed in the hygroscopicity of polluted marine aerosol as it is mixed with the sulfate aerosol outflow from continents.

The information provided by the adjoint sensitivities allows the apportionment of changes in N_d due to specific changes in either n_{a_i}, κ_{a_i} or v_{a_i}, and to do so in a spatially-resolved manner. This apportionment is achieved by combining the change in aerosol number Δn_{a_i}, aerosol volume Δv_{a_i} (proportional to the aerosol mass concentration changes), and mode hygroscopicity, $\Delta \kappa_{a_i}$ between PD and PI simulations, with the adjoint sensitivity fields using a first order approximation, i.e.,

$$(\Delta N_d)_{\chi_i} = \frac{\partial N_d}{\partial \chi_j} \Delta \chi_j \tag{32}$$

Figure 14 shows the estimated change in N_d between PI and PD simulations that can be attributed to changes in the number $(\Delta N_d)_{n_a}$, volume $(\Delta N_d)_{v_a}$, and hygroscopicity, $(\Delta N_d)_{\kappa_a}$, of accumulation mode aerosol using Equation (32). This analysis shows a negligible contribution from fine and coarse modes to ΔN_d and is therefore not shown.

From Figure 14 it is clear that the dominant contributor to ΔN_d is the accumulation mode aerosol number, with a strong signal over continental regions. The spatial patterns and intensity of this field are very similar across parameterizations. Large areas of the globe exhibit a negative $(\Delta N_d)_{n_a}$, particularly over North America, and over the British Islands, as is also seen in Figure 11. Since $\partial N_d / \partial n_{a_i}$ for accumulation mode aerosol is always positive, this reduction must be associated with a decrease in n_{a_i} from pre-industrial times over those areas. This trend occurs even though aerosol mass concentration has not decreased over those areas, supporting the idea that this is due to a decrease in primary emitted particles [*Wang et al.*, 2011]. This is further discussed in section 5.4.3.1.

After Δn_a, the next largest contributor to ΔN_d is Δv_a, i.e., the change in total aerosol volume (Fig. 14b, 14e, 14h and 14k). This field is also heavily concentrated in areas dominated by biomass burning (e.g., Central Africa) and sulfate aerosol (e.g., Europe, Southeast Asia and North America).

Unraveling the contributions of aerosol parameters to ΔN_d from different variables casts light on the diverging parameterization response over specific regions. Figures 14e, 14h, 14b and 14k, show that $(\Delta N_d)_{v_a}$ has a different response for ARG and FN parameterizations. Over continental areas, when ARG or ARGα are used, $(\Delta N_d)_{v_a}$ is much higher as compared with simulations with either FN or FN-IL. This is in fact a consequence of the two-fold stronger sensitivity of N_d to d_{g_i} exhibited by ARG. This markedly stronger sensitivity to v_{a_i}, is magnified in regions were aerosol changes are dominated by condensible species, and largely explain the higher N_d and ΔN_d over Southeast Asia observed in Figure (11). This region is particularly important in controlling the strength of the AIE, particularly through the impact it has on liquid water path.

Figures 14c, 14f, 14i and 14l show $(\Delta N_d)_{\kappa a}$ for the different parameterizations, indicating that chemical composition effects represent a weak contribution to ΔN_d from pre-industrial times.

5.4.3.1 Sensitivity of CDNC to POM burden

Further apportionment of the impacts of aerosol emissions on N_d requires the adjoint of the aerosol module [e.g., *Karydis et al.*, 2012a], which is not yet available for MAM3. However, as POM is emitted directly in the particle phase and instantaneously merged with the accumulation mode, we can use the size distribution of emitted particles to estimate the increase in number concentration per each $\mu g m^{-3}$ of POM.

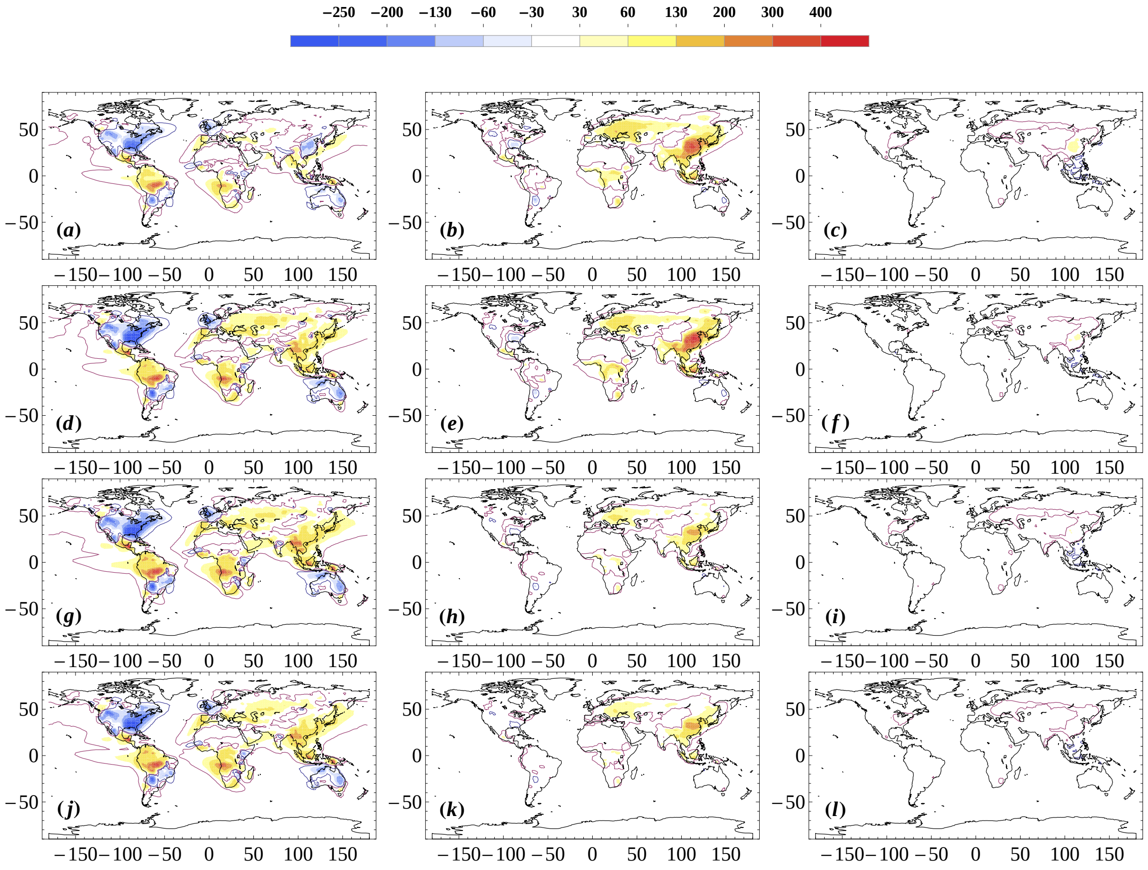

Figure 14: Change in number of activated cloud droplets (in cm^{-3}) attributable to changes in accumulation mode aerosol properties. **(a)-(c)** δN_d due to change in aerosol number (a), aerosol volume (b), and aerosol hygroscopicity (c) for simulation with the ARG parameterization **(d)-(f)** Same as above, but for the simulation using the FN activation parameterization

.

The impact of POM has been the subject in previous modeling studies, finding that inclusion of POM can contribute significantly to the CCN population (e.g, *Pierce et al.* [2007]; *Adams and Seinfeld* [2003]). These studies suggest that even when the organic aerosol lacks hygroscopicity, it contributes to the CCN population as a seeding particle where a hydrophilic coating can condense on. When these aerosol species are assumed internally mixed, they directly contribute to the number of CCN regardless of their hygroscopicity. In this section, we utilize the adjoint approach to quantify the contribution attributable to POM to changes in N_d in different regions to show the significant regional impact of POM in droplet number. To express the mass emissions to number emissions, the guidelines proposed by *Dentener et al.* [2006] are followed. POM is assumed to be emitted with a lognormal size distribution with geometric standard deviation $\sigma_{ge} = 1.8$ and a geometric mean diameter $d_{ge} = 0.08\mu$m. This size however, is uncertain, with a wide range of mode diameters reported in the literature. Some studies consider such particle sizes to be too small by up to a factor of 2 [e.g., *Anderson et al.*, 1996], arguably leading to an over-representation of the impact of primary emissions on total aerosol number [*Yu and Luo*, 2009]. Considering the dependencies of N_d on variables related to POM, the sensitivity of N_d to changes in POM mass, m_{POM}, can then be expressed as:

$$\frac{dN_d}{dm_{POM}} = \sum_{i}^{n_m} \frac{\partial n_{a_i}}{\partial m_{POM}} \left(\frac{\partial N_d}{\partial n_{a_i}}\right)_{adj} + \frac{\partial \kappa_{a_i}}{\partial m_{POM}} \left(\frac{\partial N_d}{\partial \kappa_{a_i}}\right)_{adj} + \frac{\partial v_{a_i}}{\partial m_{POM}} \left(\frac{\partial N_d}{\partial v_{a_i}}\right)_{adj} \tag{33}$$

The terms in the right hand side of Equation (33) account for the contribution to dN_d/dm_{POM} from number concentration changes, hygroscopicity of the corresponding mode κ_{ai}, and the lastly, for the contribution to the change in total aerosol volume, respectively. Since all the POM is emitted in the accumulation mode, the summation over modes on equation (33) reduces to one term, ($i = 1$ used to denote the accumulation mode),

$$\frac{\partial n_{a_1}}{\partial m_{POM}} \approx \left(\rho_{POM} \frac{\pi}{6} d_{ge}^3 \exp\left(4.5 \ln^2 \sigma_{ge}\right)\right)^{-1} \tag{34a}$$

$$\frac{\partial \kappa_{a_1}}{\partial m_{POM}} = \frac{(\kappa_{POM} - \kappa_{a_1})}{v_{a_1} \rho_{POM}} \tag{34b}$$

$$\frac{\partial v_{a_1}}{\partial m_{POM}} = \frac{1}{\rho_{POM}} \tag{34c}$$

where ρ_{POM} is the assumed density for POM. The change in N_d associated with the mass concentration change of POM between present-day and pre industiral cases,

$\Delta m_{_{POM}}$, is estimated from equation (33) as $(\partial N_d/\partial m_{_{POM}})\Delta m_{_{POM}}$. The resulting fields after applying this analysis are shown in Figure 15 for the case of ARGα. Only the first two terms, associated with number and volume are illustrated in Figure 15 since the impact of POM on κ_{a_i} had a negligibly small contribution to N_d. The distribution of these fields closely track those areas where there has been either increases or decreases in biomass burning according to the emission inventories used. This analysis reaffirms the strong impact of POM in N_d through its contribution to accumulation mode aerosol number. This contribution is markedly regional, since it is associated with a specific emission sector. Areas such as North America, the British islands and Australia show a marked decrease in N_d attributable to POM. On the other extreme, areas were there is large contribution from biomass burning, such as central Africa and South America, as well as Southeast Asia, show a large increase in N_d between PI and PD simulations.

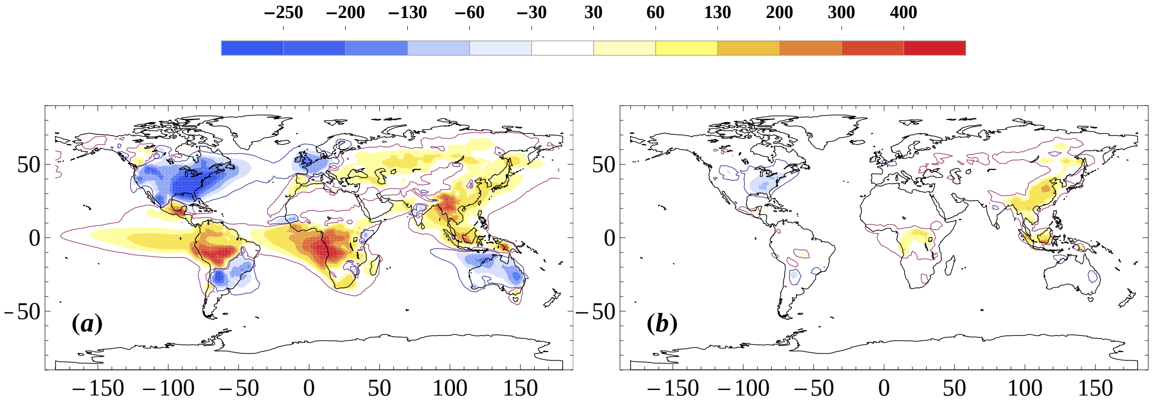

Figure 15: Estimated contribution to changes in N_d (in cm^{-3}) due mass change of POM aerosol. **(a)** Due to changes associated with the number concentration alone, **(b)** Changes attributable to mass (volume) associated with POM aerosol. Results shown here are for the ARGα parameterization.

.

5.5 Quantifying parametric uncertainty with the adjoint approach

In this section, we utilize the information provided by the gradient of the activation parameterizations to investigate model sensitivity to uncertainty in model parameters.

5.5.1 Sensitivity of CDNC to hygroscopicity parameter

The adjoint of the activation scheme can be used to estimate the envelope of uncertainty in N_d associated with parametric uncertainty. We focus here on the hygroscopicity parameter of organic aerosol species, and estimate the geographic imprint of its uncertainty on N_d. The first-order derivative of N_d with respect to κ_α of any species can be calculated from Equation (29) as

$$\frac{\partial N_d}{\partial \kappa_\alpha} = \sum_i \left(\frac{\partial N_d}{\partial \kappa_{a_i}}\right) \frac{\partial \kappa_{a_i}}{\partial \kappa_\alpha} = \sum_i \left(\frac{\partial N_d}{\partial \kappa_{a_i}}\right) v_{\alpha,i} \tag{35}$$

Then, the uncertainty in N_d associated to κ_α can be estimated, to first order, as

$$(\delta N_d)_{\kappa_\alpha} \approx \frac{\partial N_d}{\partial \kappa_\alpha} \delta \kappa_\alpha \tag{36}$$

where $\delta \kappa_\alpha$ is the uncertainty in κ_α. The assumed hygroscopicity of SOA and POM of $\kappa_{soa} = 0.14$ and $\kappa_{pom} = 0.1$ respectively (Table 6), however, there is a wide range of values reported for these parameters in the literature [e.g., *Lathem et al.*, 2013]. For application of Equation (36) we investigated the impact on CDNC of a ±50% uncertainty in κ_α. The resulting fields (Figure 16) indicate the regions were the uncertainty of the assumed hygroscopicity for organic matter impacts the CDNC the most.

For SOA, the annual-average percent CDNC uncertainty was 5.1% over continents for PD, and 7.8% for PIa simulations. The percentages are negligible over oceanic regions averaging less than 0.5% in all cases. For the PD simulations, the uncertainty can be as large as 15% over continents, while for PIa it can be up to 30% over the boreal forests owning to the large contribution of organics to aerosol volume in pre-industrial conditions. The uncertainty associated with the hygroscopicity of POM is smaller compared to that of SOA, with annual-average CDNC uncertainty over continents of 2.5% (3.5%) for the PD (PIa) simulation, while reaching a maximum of 16% (22%) for the corresponding PD (PIa) simulations. These results agree qualitatively with previous work focused on CCN uncertainty associated with perturbed parametric values [*Liu and Wang*, 2010].

Equation (36) only includes the effects of uncertainty during the step of aerosol activation. It does not account for other changes in CDNC associated with the modified hygroscopicity. For instance, an increase (decrease) in hygroscopicity might also increase (decrease) the rate of wet removal, reducing (augmenting) the total aerosol burden and having a corresponding impact on CDNC. Therefore the uncertainties presented here are an upper limit for $\partial N_d / \partial \kappa_\alpha$.

5.6 Summary and Conclusions

The sensitivity of cloud droplet number concentration to aerosol properties was evaluated in a state-of-the-art GCM by using an adjoint sensitivity approach. Two commonly used parameterization frameworks, the ARG [*Abdul-Razzak and Ghan*, 2000] and FN [*Fountoukis and Nenes*, 2005], were tested and compared within the CAM5.1 GCM.

All the parameterizations considered here showed a consistent sensitivity to accumulation mode aerosol number for both, marine and continental aerosol. Furthermore, these sensitivities agreed to within ±10% when compared to detailed numerical simulations of the activation process. Overall, the parameterizations also showed consistent responses to the updraft velocity. Both this variables being central in the determination of N_d.

Among those variables with inconsistent responses across parameterizations, it was

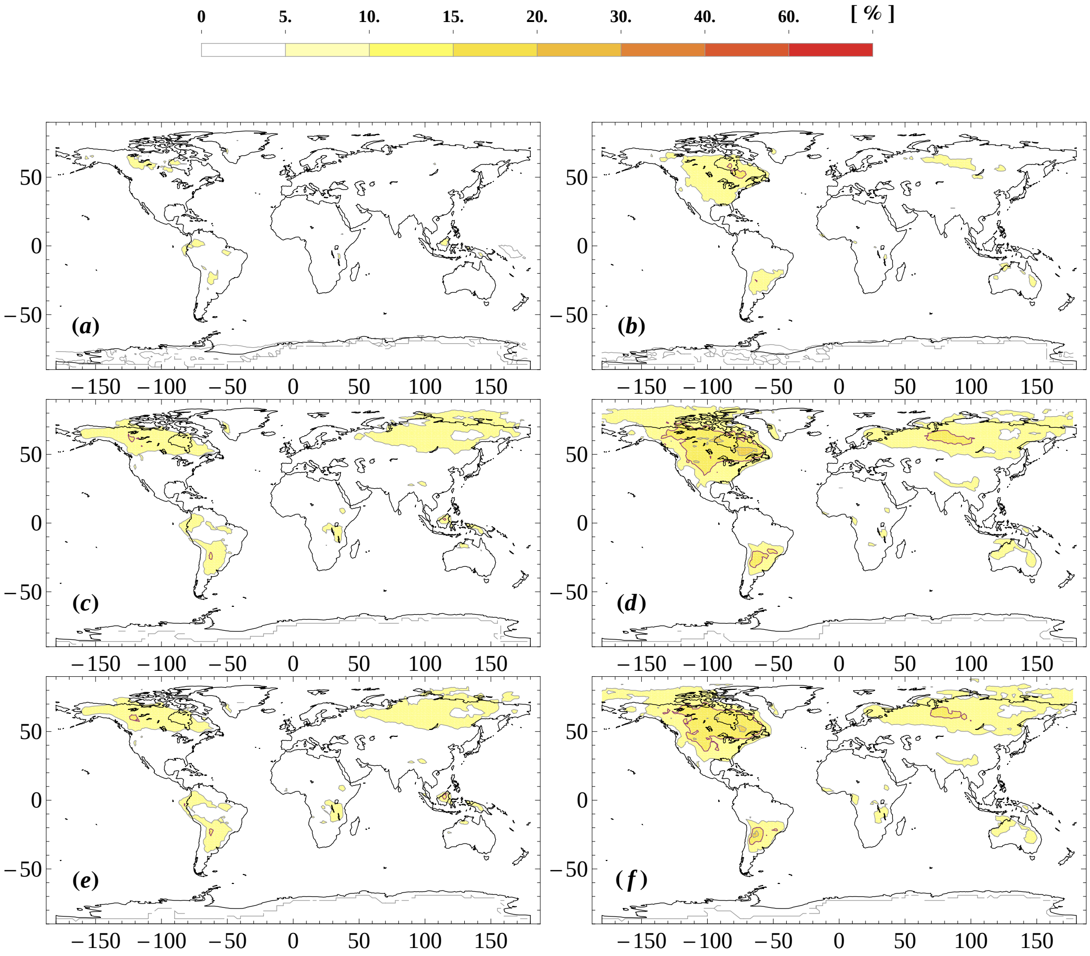

Figure 16: Estimated percent uncertainty on N_d due to a ±50% uncertainty in the hygroscopicity parameter of SOA for: **(a)** ARGα-PD, **(b)** ARGα-PIa, **(c)** FN-PD, **(d)** FN-PIa, **(e)** FN-IL-PD, **(f)** FN-IL-PIa

.

found that the response to coarse mode aerosol characteristics varies widely across parameterizations, ranging from an overepresentation of the water depletion of coarse mode particles in ARGα, to a lack of sensitivity to large particles in FN. The FN-IL, which includes the water uptake by inertially limited CCN, captures the sensitivity to coarse mode aerosol more accurately than the other schemes considered in this study. Although not a significant contributor to N_d, the large amount of water vapor depleted by the coarse mode particles can modulate the magnitude of dN_d/dn_a. In fact, the consistently lower N_d over oceans predicted by ARGα compared to FN and FN-IL is due to the large sensitivity to coarse mode particles. However, the diverse response observed across parameterizations implies that a physically consistent representation of coarse mode aerosol remains a challenge for activation parameterizations [*Morales and Nenes*, In preparation].

Although great emphasis in the literature has been placed in ensuring that activation parameterizations capture dN_d/dn_a consistently, our study suggests that sensitivity to aerosol number alone does not capture the full extent of aerosol indirect effects, and does not explain the differences in N_d fields produced with these parameterizaitons. We found that the sensitivity of N_d to the geometric mean diameter, d_{g_i}, was on average two times higher for ARG compared to FN and FN-IL. This sensitivity difference accounts for the much larger N_d concentration predicted with ARGα over heavily polluted environments. This is particularly noticeable over Southeast Asia, region that also has very deep clouds. Therefore, large increases in N_d over that region have a profound impact on LWP, and therefore over shortwave cloud forcing. These two factors, i.e., the large change in N_d that induces a large change in LWP over Southeast Asia, the Maritime continent and the North Pacific have been shown to control the strenght of the indirect effects on CAM to a large extent *Wang et al.* [2011].

The sensitivity analysis reaffirms the well-known importance of accumulation mode aerosol number concentration in controlling cloud droplet number concentrations. It was found that both, the variables controlling the size distribution of aerosol contribute the most to changes in CDNC between present day and pre-industrial simulations. For the conditions commonly found in stratiform clouds simulated by CAM, aerosol number and size plays a much more important role than the chemical composition of the aerosol.

The adjoint sensitivities were further used in this study to unravel the regional footprint of specific aerosol species to N_d. The large impact of primary organic matter (POM) in controlling accumulation mode number concentration was shown to also control the magnitude of the changes in N_d over large areas of the planet. This indicates that given their considerable impact on both, aerosol and CDNC, efforts should be made to constrain the uncertainty in emission sizes for this primary particles.

Computation of the regional distribution of N_d sensitivities to aerosol size distribution, chemical composition, and dynamic parameters is an important step in understanding the relative contribution of aerosol parameters to CDNC variability. We demonstrate this using the adjoint-sensitivities to attribute the contribution from different sectors to the change in N_d between present day and pre-industrial simulations. Not surprisingly, changes in aerosol number, to a large extent control the changes in N_d, followed by change in mass, and to a lesser extent, changes in the hygroscopicity of aerosol. The powerful and computationally inexpensive information from adjoint analysis leads to an unprecedented understanding of what causes differences in model responses from each activation scheme.

5.7 Acknowledgements

We thank the DOE EaSM program for funding that supported the research carried out in this proposal. Authors would like to thank Dr. Xiaohong Liu for providing access to the computational resources. All the simulations for this work were performed with resources from the National Energy Research Scientific Computing Center (NERSC) of the U.S. Department of Energy.

5.8 Adjoint Development

The method to compute the number of activated cloud droplets, N_d, in both parameterizations considered here involves two conceptual steps. The first step is the computation of the CCN spectrum, i.e., the cumulative number of particles with critical supersaturation less than a given value s. The second step consists of determining the maximum supersaturation, s_{max}, that develops in the ascending air parcel that rises with updraft velocity, w, and includes the water vapor condensation sink provided by the CCN computed in the previous step. The first step is achieved by mapping the aerosol size distribution and chemical composition onto supersaturation space [e.g., *Fountoukis and Nenes*, 2005; *Karydis et al.*, 2012b], i.e.,

$$N_{CCN}(s) = \sum_{i}^{n_m} \frac{n_{ai}}{2}\left[1 - \mathrm{erf}(u_i(s))\right] \tag{37}$$

where

$$u_i = \frac{2\ln\left(s_{mi}/s\right)}{3\sqrt{2}\ln\sigma_{gi}} \tag{38}$$

and s_{mi} is the critical supersaturation for a particle with a size equal to d_{g_i} and hygroscopicity parameter κ_i, $s_{mi} = \frac{2}{\sqrt{\kappa_i}}\left(\frac{A}{3d_{pg_i}}\right)^{3/2}$. Equations 37 and 38 consider only Köhler theory for computation of CCN. The impact of water adsorption onto insoluble particles such as dust, can also be treated with a similar formalism [*Kumar et al.*, 2009]. The second step is achieved by finding an approximate solution to the equation describing the supersaturation tendency in the ascending air parcel, which can be written as,

$$\left(\frac{dq}{dt}\right)_{s_{max}} = \frac{\alpha w}{\gamma} \tag{39}$$

Equation (39) expresses the balance in production and depletion of water vapor attained in the ascending air parcel between the adiabatic cooling provided by the cloud updraft $\alpha w/\gamma$, and the depletion of supersaturation by condensation on the growing droplets, (dq/dt). Once s_{max} is determined from Equation (39), the number of activated droplets is given by the CCN spectra evaluated at $s = s_{max}$,

$$N_d = N_{CCN}(s_{max}) \tag{40}$$

The two parameterizations differ in the approximations made in the solution of Equation (39). An in-depth analysis of these assumptions can be found in *Ghan et al.* [2011]. The ARG is constructed by performing a statistical fit to a large set of detailed numerical solutions to this equation, while the FN use the "population spliting" approach, which brings Equation (39) to a form where an iterative numerical solution can be found for s_{max}.

5.8.1 FN and FN-IL parameterizations

The development of the adjoint of the *Fountoukis and Nenes* [2005] parameterization (FN), as well as that for the adsorption activation parameterization of *Kumar et al.* [2009] is described in full detail in *Karydis et al.* [2012b]. Briefly, because the computation of N_d in FN is achieved by iterative solution of Equation (39), the computation of the sensitivities has to be achieved by performing a line-by-line differentiation of the numerical routines. *Karydis et al.* [2012b] used the automatic differentiation software TAPENADE to construct the routines necessary for efficient computation of derivatives. The FN-adjoint built with this procedure, yields the set of sensitivities of N_d with analytical precision, and the computational cost of the computation is a constant multiple, independent of the number of input parameters, of the cost of computing N_d itself.

5.8.2 ARG parameterization

The ARG droplet activation parameterization [*Abdul-Razzak et al.*, 1998; *Abdul-Razzak and Ghan*, 2000] computes the maximum supersaturation, s_{max}, and droplet number concentration, N_d, explicitly as a function of the updraft velocity, w, the aerosol size distribution parameters, σ_{g_i} and d_{g_i}, n_{a_i}, and chemical composition of the aerosol, represented by κ_{a_i}. In this parameterization, s_{max} is given by,

$$s_{max} = \left\{ \sum_{i}^{n_m} \frac{1}{s_{mi}^2} \left[f_{1,i} \left(\frac{\zeta_i}{\eta_i} \right)^{3/2} + f_{2,i} \left(\frac{s_{mi}^2}{\eta_i + 3\zeta_i} \right)^{3/4} \right] \right\}^{-1/2} \tag{41}$$

where $f_{1,i}$ and $f_{2,i}$ are functions of σ_{g_i} only. The explicit functionality of $f_{1,i}$ and $f_{2,i}$, together with the definitions of ζ_i and η_i can be found in *Abdul-Razzak and Ghan* [2000]. Because Equation (41) is an explicit function of the input variables, it is amenable for the calculation of analytical expressions for its derivatives. In this section we follow the approach of *Rissman et al.* [2004], and expand these expressions to include other parameters. The derivatives of N_d to a parameter χ_j reads

$$\frac{\partial N_d}{\partial \chi_j} = \frac{\partial N_{CCN}}{\partial \chi_j} - \sum_i \frac{\partial u_i}{\partial \chi_j} \left(\frac{n_{ai}}{\sqrt{\pi}} e^{-u_i^2} \right) \tag{42}$$

The term $\partial N_{CCN} / \partial \chi_j$ is zero for all variables except for $\chi_j = n_{a_j}$, for which case it is equal to $\left[1 - \mathrm{erf}(u_i)\right]/2$. The partial derivatives of u_i read:

$$\frac{\partial u_i}{\partial w} = -\frac{\sqrt{2}}{3 s_{max}} (\ln \sigma_{gi})^{-1} \frac{\partial s_{max}}{\partial w} \tag{43a}$$

$$\frac{\partial u_i}{\partial n_{a_j}} = -\frac{\sqrt{2}}{3 s_{max}} (\ln \sigma_{g_i})^{-1} \frac{\partial s_{max}}{\partial n_{a_j}} \tag{43b}$$

$$\frac{\partial u_i}{\partial \kappa_{a_j}} = -\frac{\sqrt{2}}{3 s_{max}} (\ln \sigma_{g_i})^{-1} \left(\frac{s_{max}}{2\kappa_{a_i}} \delta_{ij} + \frac{\partial s_{max}}{\partial \kappa_{a_j}} \right) \tag{43c}$$

$$\frac{\partial u_i}{\partial d_{g_j}} = -\frac{\sqrt{2}}{3 s_{max}} (\ln \sigma_{g_i})^{-1} \left(\frac{3 s_{max}}{2 d_{g_i}} \delta_{ij} + \frac{\partial s_{max}}{\partial d_{g_j}} \right) \tag{43d}$$

$$\frac{\partial u_i}{\partial \sigma_{g_j}} = -\frac{\sqrt{2}}{3 s_{max}} (\ln \sigma_{g_i})^{-1} \left(\frac{3 s_{max} u_i}{\sqrt{2} \sigma_{g_i}} \delta_{ij} + \frac{\partial s_{max}}{\partial \sigma_{g_j}} \right) \tag{43e}$$

where $\delta_{ij} = 0$ for $i \neq j$, and $\delta_{ij} = 1$ for $i = j$. Defining the following functions,

$$k_i = f_{1,i} \left(\frac{\zeta_i}{\eta_i} \right)^{3/2} \tag{44a}$$

$$g_i = f_{2,i} \left(\frac{s_{mi}^2}{\eta_i + 3\zeta_i} \right)^{3/4} \tag{44b}$$

the gradient of s_{max} can be written as,

$$\frac{\partial s_{max}}{\partial w} = \frac{3}{4}\frac{s_{max}^3}{w}\sum_i \frac{1}{s_{mi}^2}\left(k_i + \frac{3g_i}{4}\frac{\eta_i+\zeta_i}{\eta_i+3\zeta_i}\right) \tag{45a}$$

$$\frac{\partial s_{max}}{\partial n_{a_i}} = -\frac{3}{4n_{a_i}}\frac{s_{max}^3}{s_{mi}^2}\left(k_i + \frac{g_i}{2}\frac{\eta_i}{\eta_i+3\zeta_i}\right) \tag{45b}$$

$$\frac{\partial s_{max}}{\partial \kappa_{a_i}} = -\frac{1}{2\kappa_{a_i}}\frac{s_{max}^3}{s_{mi}^2}\left(k_i + \frac{g_i}{4}\right) \tag{45c}$$

$$\frac{\partial s_{max}}{\partial d_{g_i}} = -\frac{3}{2d_{g_i}}\frac{s_{max}^3}{s_{mi}^2}\left(k_i + \frac{g_i}{4}\right) \tag{45d}$$

$$\frac{\partial s_{max}}{\partial \sigma_{g_i}} = -\frac{5}{2\sigma_{g_i}}\frac{s_{max}^3\ln(\sigma_{g_i})}{s_{mi}^2}\left(k_i + \frac{g_i}{4}\right) \tag{45e}$$

5.8.3 ARGα parameterizations: Non-continuum effects

Ghan et al. [2011] extended the ARG parameterization to account for non-continuum effects through the inclusion of a size dependent mass transfer coefficient G, that has explicit dependence on the mass accommodation coefficient α_c. In such way, the transfer coefficient, G_i, is defined as

$$G_i = G_0\frac{G(D_{pci},\alpha_c)}{G(D_{pci},1)} \tag{46}$$

where G_0 is the mass transfer coefficient for the continuum regime, and $G(x,\alpha_c)$ is the size dependent mass transfer coefficient [e.g., *Pruppacher and Klett*, 1997]. D_{pci} is the critical wet diameter corresponding to d_{g_i}. The derivatives with respect to d_{g_i} and κ_{a_i} are affected by the redefinition of G according to Equation (46). Since N_d now depends on α_c, the corresponding sensitivities can also be computed. The derivatives of s_{max} are as follows:

$$\frac{\partial s_{max}}{\partial \kappa_{a_i}} = -\frac{1}{2\kappa_{a_i}}\frac{s_{max}^3}{s_{mi}^2}\left[\left(k_i + \frac{g_i}{4}\right) + \frac{3\Psi_i}{16}\left(k_i + \frac{3g_i}{4}\frac{\eta_i+\zeta_i}{\eta_i+3\zeta_i}\right)\right] \tag{47a}$$

$$\frac{\partial s_{max}}{\partial d_{g_i}} = -\frac{3}{2d_{g_i}}\frac{s_{max}^3}{s_{mi}^2}\left[\left(k_i + \frac{g_i}{4}\right) + \frac{3\Psi_i}{16}\left(k_i + \frac{3g_i}{4}\frac{\eta_i+\zeta_i}{\eta_i+3\zeta_i}\right)\right] \tag{47b}$$

This extension also allows for the calculation of the sensitivities of s_{max} and N_d to the mass accommodation coefficient, α_c. The corresponding sensitivities are given by

$$\frac{\partial s_{max}}{\partial \alpha_c} = -\frac{3}{16}\frac{s_{max}^3}{\alpha_c}\sum_i \frac{\Upsilon_i}{s_{mi}^2}\left(k_i + \frac{3g_i}{4}\frac{\eta_i + \zeta_i}{\eta_i + 3\zeta_i}\right) \tag{48}$$

and,

$$\frac{\partial u_i}{\partial \alpha_c} = -\frac{\sqrt{2}}{3s_{max}}(\ln \sigma_{gi})^{-1}\frac{\partial s_{max}}{\partial \alpha_c} \tag{49}$$

The coefficients Υ_i and Ψ_i are defined as:

$$\Psi_i = K_i G_i(D_{pci}, \alpha_c)\left(1 - \alpha_c \frac{G_0}{G_i}\right) \tag{50}$$

and

$$\Upsilon_i = K_i G_i(D_{pci}, \alpha_c) \tag{51}$$

where the function K_i is a temperature dependent coefficient given by

$$K_i = \frac{2\rho_w RT}{e_s M_w \alpha_c D_{pc_i}}\left(\frac{2\pi M_w}{RT}\right)^{1/2} \tag{52}$$

In the previous expression T is the temperature, ρ_w is the density of water, M_w is the molecular weight of water, R the universal gas constant, and e_s is the saturation vapor pressure of water at temperature T.

5.9 Validation of parameterization derivatives

The accuracy of the first order derivatives of FN and ARG introduced in Appendix 5.8 have been extensively tested by comparing them against central difference computations [e.g., *Karydis et al.*, 2012b]. In this section however, we perform an evaluation of the adjoint sensitivities against detailed numerical simulations of the activation process, since this provides a method for validating the physical consistency of the parameterization-derived sensitivities.

Annual average fields of n_{a_i}, κ_{a_i}, d_{g_i} and w, corresponding to the 930 hPa pressure level from a 6-year simulation with CAM5.1 were used to drive off-line computations with a Lagrangian parcel model. The Lagrangian parcel model used here explicitly computes the size-resolved growth of cloud droplets in a non-entraining parcel ascending with a constant updraft velocity [*Pruppacher and Klett*, 1997]. The temporal evolution of supersaturation is also computed. The sensitivities were performed by central difference computation for each of the ten variables (requiring of 20 model integrations per grid cell). Identical input was used to drive the adjoint sensitivities of ARGα, FN, and FN-IL. All the calculations were performed assuming an accommodation coefficient $\alpha_c = 0.1$ [*Raatikainen et al.*, 2013].

The relative error between the parcel model and parameterization-derived sensitivities are summarized in Table (10). The relative error ϵ_χ for a quantity χ is defined here as

$$\epsilon_\chi = 1 - \frac{\chi_{PM}}{\chi_{param}}, \tag{53}$$

where χ_{PM} and χ_{param} are the parcel model and parameterization derived value for χ respectively. This analysis reveals that the accuracy of the derivatives fluctuates widely across the different variables considered. Among those sensitivities that are better captured by all the parameterizations are those of N_d to updraft, $\partial N_d/\partial w$, accumulation mode number concentration, and total aerosol number $\mathrm{d}N_d/\mathrm{d}n_a$, which are all within ±30% error. Similarly, all parameterizations capture N_d within a ±20% margin, with ARGα and FN-IL slightly underestimating N_d while FN shows the opposite trend, biasing $N_d \sim 10\%$ high. Table (10) reflects that the largest errors are encountered for coarse mode particles, with sensitivity of N_d to Aitken and accumulation mode have overall smaller biases than those of coarse mode characteristics.

Table 10: Relative error for N_d, s_{max}, and the adjoint-sensitivities $\partial N_d/\partial \chi_j$, computed with the adjoint of the activation parameterizations, as compared against numerical parcel model values. Reported values correspond to the mean and the standard deviation of the percent error.

Sensitivity	Aerosol Mode	ARGα	FN	FN-IL
N_d		$-18.1 \pm 9.7\%$	$8.1 \pm 7.7\%$	$-10.5 \pm 6.2\%$
S_{max}		$-42.3 \pm 13\%$	$31 \pm 22.2\%$	$-24 \pm 6.7\%$
$\partial N_d/\partial n_{ai}$	Aitken	$-93 \pm 38\%$	$56 \pm 81\%$	-57 ± 16.6
	Accumulation	$10.6 \pm 24\%$	$3.5 \pm 18\%$	-8.1 ± 20.4
	Coarse	$-509 \pm 838\%$	$210 \pm 225\%$	$-93 \pm 131\%$
$\mathrm{d}N_d/\mathrm{d}n_a$		$-15.6 \pm 8.8\%$	$+9.3 \pm 19\%$	$-19.4 \pm 15\%$
$\partial N_d/\partial \kappa_{ai}$	Aitken	$-74 \pm 18\%$	$27 \pm 53\%$	$-48 \pm 20\%$
	Accumulation	$190 \pm 345\%$	$101 \pm 223\%$	$101 \pm 223\%$
	Coarse	$-300 \pm 223\%$	$100 \pm 0\%$	$-59 \pm 51\%$
$\partial N_d/\partial d_{gi}$	Aitken	$-74 \pm 18\%$	$27 \pm 53\%$	$-42 \pm 20\%$
	Accumulation	$191 \pm 348\%$	$96 \pm 216\%$	$96 \pm 216\%$
	Coarse	$-297 \pm 214\%$	$100 \pm 0\%$	$-64 \pm 52\%$
$\partial N_d/\partial w$		$-27.7 \pm 37\%$	$5.8 \pm 23\%$	$8.5 \pm 81\%$

It is apparent from this analysis that the largest discrepancies amongst parameterizations occur precisely for coarse mode characteristics. For instance, sensitivity of N_d to coarse mode aerosol characteristics is overpredicted by $300\% - 500\%$ for ARGα, while FN-IL reduces this overprediction to $\sim 100\%$. On the other hand, the lack of responsiveness of N_d computed with FN to perturbations in coarse mode aerosol is made clear from the relative error of $100\% \pm 0\%$ observed for coarse mode κ_{a_i} and d_{g_i}. For both this casese, the absolute value of the adjoint sensitivities is negligibly small. The variability associated with coarse mode characteristics is illustrated in Figure (17) with the derivative of N_d to the hygroscopicity κ_{a_i}.

Sensitivity to accumulation mode κ_{a_i} and d_{g_i} shows a large variability as measured by the standard deviation of the errors for all parameterizations, but the bias for the case of ARGα is a factor of 2 larger than it is for either FN or FN-IL. However, the large bias and considerable scatter for $\partial N_d/\partial \kappa_{a_i}$ and $\partial N_d/\partial d_{g_i}$ suggests that the parameterizations are not accurately capturing the dependency of N_d on those variables.

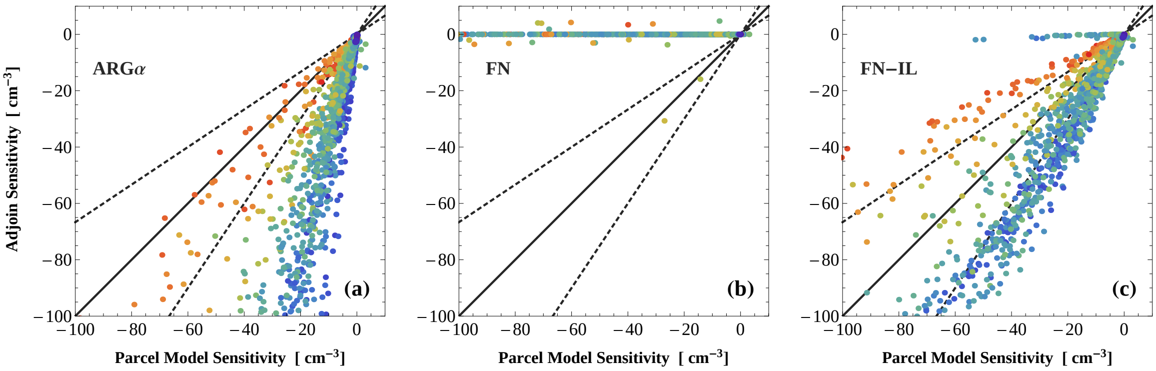

Figure 17: Comparison between the sensitivity to hygroscopicity for coarse mode aerosol, $\partial N_d/\partial \kappa_{a_i}$ (cm^{-3}), computed with detailed parcel model simulations and: **(a)** ARGα, **(b)** FN, **(c)** FN-IL

.

CHAPTER VI

AEROSOL ACTIVATION PARAMETERIZATION: THE POPULATION SPLITTING CONCEPT REVISITED

6.1 Summary

In this work we postulate, implement and evaluate modifications to the "population splitting" concept first introduced by *Nenes and Seinfeld* [2003] for calculation of water condensation rates in droplet activation parameterizations, and extended by *Barahona et al.* [2010a] to account for the water uptake of large CCN. The modifications introduced here lead to an improved accuracy and precision of the parameterization-derived s_{max} and N_d as determined by comparing against those of detailed numerical simulations of the activation process. The proposed modifications require only minor changes for their numerical implementation in existing codes.

6.2 Introduction

During the process of cloud formation aerosol particles act as cloud condensation nuclei (CCN) on which cloud droplets first form and grow. Changes in either the amount or composition of atmospheric aerosol can alter cloud microphysical and optical properties, indirectly impacting the radiatiave balance and hydrological cycle. Aerosol-cloud interactions constitute some of the most uncertain aspects of anthropogenic climate change estimates [*Intergovernmental Panel on Climate Change*, 2007].

Parameterizations that describe the activation process determine the fraction of atmospheric aerosol that activates into cloud droplets for an air parcel that ascends with an updraft velocity, w. These activation parameterizations use a Lagrangian parcel model approach to study the detailed process of water vapor condensation on the population of growing droplets. A thorough review of activation parameterizations can be found in *Ghan et al.* [2011]. Most of these activation schemes follow the framework proposed by *Twomey* [1959] which divides this task in two conceptual steps. First, determine the availability of CCN as function of supersaturation (for instance using Köhler theory together with knowledge of aerosol size distribution and chemical composition), and second, by approximately solving the water vapor balance in the ascending cloud parcel to determine the maximum supersaturation, s_{max}, attained in it. After this is done, the number of activated cloud droplets, N_d, can be found simply as the subset of CCN with a critical supersaturation, s_c, smaller than s_{max}. A number of such parameterizations have been developed using this framework [e.g., *Feingold and Heymsfield*, 1992; *Ghan et al.*, 1993; *Nenes and Seinfeld*, 2003; *Pinsky et al.*, 2012], and many have been incorporated into GCM to compute aerosol indirect effects [e.g., *Abdul-Razzak and Ghan*, 2000; *Fountoukis and Nenes*, 2005; *Ming et al.*, 2006; *Shipway and Abel*, 2010].

The central problem these schemes need to address is the correct estimation of the size of the growing droplets at the time of peak supersaturation. The condensation rate is proportional to the integral diameter of the growing droplet population, and therefore it plays an important role in defining s_{max}. This task is particularly problematic for the largest particles in the CCN population. As noted by *Chuang et al.* [1997], a portion of the CCN population, those with relatively low supersaturation (i.e., large particles) are 'inertially-limited' and their size does not equilibrate instantaneously with the ambient supersaturation. Therefore, the equilibrium assumption is not adequate for computing the sizes for these particles.

Even though these large CCN particles typically contribute a small number concentration to the CCN population, they represent an important sink for water vapor, effectively modulating the parcel s_{max} [e.g., *Ghan et al.*, 1998]. This means that even modest increases in either the number or the hygroscopicity of these large particles can cause a significant decrease in s_{max}, leading to lower droplet concentrations. Therefore, accurately accounting for the water uptake of large particles is of great importance in determining s_{max} and N_d.

Within the parameterization framework first proposed by *Nenes and Seinfeld* [2003], different approaches have been incrementally adopted to improve their ability to capture the supersaturation across a large set of conditions. *Fountoukis and Nenes* [2005] extended this framework to include the effect of mass transfer limitations in the non-continuum regime through an effective accommodation coefficient. *Kumar et al.* [2009] introduced changes in the CCN spectra to allow for adsorption activation, and *Barahona and Nenes* [2007] included the impact of entrainment and mixing in decreasing the condensation rate in the ascending parcel to sub-adiabatic levels. The prediction of N_d with *Fountoukis and Nenes* [2005] parameterization is typically within ±20% when compared to parcel model simulations for a wide range of aerosol conditions and updrafts. However, when the population of 'inertially limited' CCN is large, it tends to sliglthly overestimate N_d and s_{max}. *Barahona et al.* [2010a] noted this and introduced a novel way of approximating the condensation rate on this particles, to better account for their contribution to depleting the available water vapor. This new approach corrected the overprediction issue of *Fountoukis and Nenes* [2005] in conditions where there is a significant presence of large CCN. However, and as we show in the present work the modification by *Barahona et al.* [2010a] overrepresents the condensation rate on large CCN, introducing an slight underestimation of N_d and s_{max} under specific circumstances.

In this work we introduce some modifications to the "population splitting" concept regarding the computation of droplet size at activation. We first present a brief account of the concepts leading to the "population splitting" approach of *Nenes and*

Seinfeld [2003], and then present the proposed modifications. The augmented parameterization is evaluated by comparing computations of N_d and s_{max} against detailed parcel model simulations. Finally, the augmented parameterization is implemented in the Community Atmosphere Model, version 5.1 (CAM5.1) to investigate the spatial distribution of the simulated cloud fields, and to perform estimates of the AIE with these modifications.

6.3 General framework of activation parameterizations

The number concentration of aerosol activated into cloud droplets, N_d, is the central quantity to be predicted by activation parameterizations. These parameterizations typically determine the maximum supersaturation s_{max} developed in an ascending air parcel, and then set N_d as the subset of CCN with a critical supersaturation, s_c, smaller than s_{max}. The maximum supersaturation is attained when the supersaturation production due to expansion cooling is balanced by the water vapor depletion from condensation. If the parcel is ascending with a vertical velocity w, its supersaturation tendency can be written as [e.g., *Pruppacher and Klett*, 1997],

$$\frac{ds}{dt} = \alpha w - \gamma \left(\frac{dq_l}{dt} \right) \tag{54}$$

where (dq_l/dt) is the rate of change of liquid water mixing ratio in the parcel, q_l, and α and γ are size independent, slowly varying functions of temperature, which can be considered constant (see Appendix A). Since condensation transfers mass to the droplet population, the condensation rate in equation (54) can be expressed in terms of droplet growth rate. Ignoring the effects of curvature and solutes on the equilibrium vapor pressure of the growing droplets, the condensational growth of a droplet with diameter D_p is given by [*Nenes and Seinfeld*, 2003],

$$D_p \frac{dD_p}{dt} = Gs \tag{55}$$

where G is the mass transfer coefficient of water to the droplets (Appendix A). Since q_l is proportional to the total volume concentration of the droplet population, the condensation rate in equation (54) can be expressed in terms of D_p by using the growth rate equation (55),

$$\frac{dq_l}{dt} = \frac{\pi}{2}\frac{\rho_w}{\rho_a} G s \int n(d_p) D_p(d_p, t) \mathrm{d}d_p \tag{56}$$

where $D_p(d_p, t)$ is the wet diameter at time t of a droplet growing on an aerosol particle with dry size d_p. Equation (56) indicates that the condensation rate is proportional to the integral diameter of the droplet size distribution. Using Köhler theory to relate the size of the aerosol to s_c, the integral in equation (56) can thus be expressed in terms of the critical supersaturation s_c. Following *Nenes and Seinfeld* [2003], the integral diameter is defined here as,

$$I(0, s) \equiv \int_0^s n(s_c) D_p(s_c, t) \mathrm{d}s_c \tag{57}$$

The maximum supersaturation can be found by setting $ds/dt = 0$ in equation (54). Using equation (57) and after some manipulation, the supersaturation equation can be written as

$$s_{max} I(0, s_{max}) = \beta \tag{58}$$

with $\beta = 2\rho_a \alpha w/(\pi \rho_w \gamma G)$. Equation (58) cannot, in general, be solved analytically. The integral diameter at peak supersaturation, $I(0, s_{max})$, is the central quantity to be approximated, and still requires a formulation in terms of the dry aerosol size distribution. The "population splitting" approach [*Nenes and Seinfeld*, 2003] provides such framework to approximate D_p by identifying different regimes, and is briefly explained below.

6.3.1 The "population splitting" concept

A solution to the supersaturation balance equation (58) requires to express the condensation rate, proportional to $I(0, s_{max})$, in terms of the dry aerosol size distribution and the size of droplets at the instant of maximum supersaturation t_m. To estimate the size $D_p(s_c, t_m)$, equation (55) is often integrated from the activation time, τ_{s_c} defined as $s(\tau_{s_c}) = s_c$, to the time t_m when s reaches a maximum, i.e.,

$$D_p^2 = D_p(\tau_{s_c})^2 + 2G \int_{\tau_{s_c}}^{t_m} s dt \tag{59}$$

Two assumptions, each representing extreme asymptotic limits, have been often adopted to obtain an approximate expression for D_p in equation (59). One such approximation consists of neglecting the growth of the particles after activation, and to assume that their diameter at s_{max} is simply given by their critical diameter. i.e., that $D_p(\tau_{s_c}) = D_{pc}$ [e.g., *Ghan et al.*, 1993]. In terms of the critical supersaturation (using Köhler theory) D_{pc} is written as

$$D_p^{(1)} = \frac{2A}{3s_c} \tag{60}$$

This approximation, although adequate for the smallest CCN, has serious caveats when applied to the largest particles in the CCN population. Due to their size, droplets growing on aerosol particles with a dry diameter larger than $\sim 0.2\mu m$ cannot grow in equilibrium with the ambient supersaturation [*Chuang et al.*, 1997]. As a consequence of this 'inertial limitation' [*Nenes et al.*, 2001], as the parcel supersaturation increases these large droplets fall far behind their equilibrium diameter, and therefore application of equation (60) leads to a large overestimation of their size. This in turn leads to overestimating the condensation rate, biasing s_{max} and N_d low [*Ghan et al.*, 1993].

Another commonly found approximation, first introduced by *Twomey* [1959] in his classic work, considers that particle growth after exposure to their critical supersaturation is the main contributor to particle size. This approach, effectively neglects the initial size of the particles ($D_p(\tau_{s_c}) \approx 0$) and considers only the contribution of the growth term in equation (59). *Twomey* [1959] further proposed a lower bound for the supersaturation integral relating it to s_c, namely

$$\int_{\tau_{s_c}}^{t_m} s dt = \frac{s_{max}^2 - s_c^2}{2\alpha w} \tag{61}$$

However, neglecting the size of the particles when exposed to $s = s_c$ can cause a large underestimation of D_p, and therefore, of the condensation, particularly for large CCN. When this approximation is adopted, the droplet size $D_p(s_c, t_m)$ can be found by replacing equation (61) into (59), i.e.,

$$D_p^{(2)} \approx \left(\frac{G}{\alpha w}\right)^{1/2} \left(s_{max}^2 - s_c^2\right)^{1/2} \tag{62}$$

Subsequent approaches to the problem have acknowledged that both regimes are likely to occur within the same CCN population. *Abdul-Razzak et al.* [1998] identified this regimes based on the proximity of s_c to s_{max}, proposing that for particles with $s_c << s_{max}$ the growth term was dominant, while for those with $s_c \sim s_{max}$ the effect of of growth was negligible, and their size was close to their activation size.

Nenes and Seinfeld [2003] further build on this concept to establish specific criteria to split the population of CCN between particles where the equilibrium assumption, $D_p = D_p^{(1)}$, was adequate, and those for which the droplet growth contributed more significantly to particle size, i.e., $D_p = D_p^{(2)}$. To partition the CCN population between these regimes *Nenes and Seinfeld* [2003] determined the values of s_c for which the critical wet diameter D_{pc} was equal to the growth term after activation, effectively establishing the boundaries between regimes. Solving the resulting equation, i.e., $D_p^{(1)} = D_p^{(2)}$ for s_c, two roots were found to satisfy the equality,

$$\frac{s_p^{\pm}}{s_{max}} = \frac{1}{\sqrt{2}} \left[1 \pm \left(1 - \frac{\xi_c^4}{s_{max}^4} \right)^{1/2} \right]^{1/2} \tag{63}$$

where $\xi_c = (16A^2 \alpha w/9G)^{1/4}$. These roots define two different regions in s_c space (Figure 18), one for which the growth term is larger than the critical diameter ($D_p^{(1)} < D_p^{(2)}$), and one for which D_{pc} is larger than the growth term ($D_p^{(1)} > D_p^{(2)}$). In terms of the discriminant $\Delta = 1 - \xi_c^4/s_{max}^4$ of *Nenes and Seinfeld* [2003], two clear regimes arise from equation (63), one for $s_{max} > \xi_c$ (equivalent to the condition $\Delta > 0$), and another for $s_{max} < \xi_c$ (equivalent to the condition $\Delta < 0$).

When $s_{max} > \xi_c$, both roots $s_p^{\pm}$ exist, splitting the CCN into three different populations. For the smallest particles, those with $s_{max} > s_c > s_p^+$, $D_p^{(1)} > D_p^{(2)}$ because the particles do not have enough time to grow. Owing to the inverse relation between s_c and D_{pc}, those particles with $s_p^- > s_c$, have such large critical diameters that they cannot be matched by the growth in equation (62), and therefore, the same inequality holds for them. For the CCN population in between, those with $s_p^+ > s_c > s_p^-$, the growth term is larger than D_{pc}. Finally, when $s_{max} < \xi_c$, equation (63) has no solutions reflecting the fact that in this region the critical diameter $D_p^{(1)}$ is always larger than the growth term, $D_p^{(2)}$.

Nenes and Seinfeld [2003] used the clues provided by this classification to define rules for the estimation of D_p. For those CCN with $s_{max} > s_c > s_p^+$ (termed here population I), D_p was approximated by D_{pc}. This is a reasonable assumption since these small particles are the most likely to equilibrate instantaneously with the ambient supersaturation, and as discussed before, they have little time to growth. For those CCN with $s_p^+ > s_c > s_p^-$ (termed here population II), approximation $D_p^{(2)}$ was used. This stills leaves a third population out, the large CCN with $s_c < s_p^-$. Despite the rules of equation (63) dictate that for this population $D_p^{(1)} > D_p^{(2)}$, it is well known that in actuality they are generally not capable of growing at equilibrium, so their size at s_{max} is much smaller than their D_{pc}. With these argument these large CCN particles were merged together into population II, using approximation $D_p^{(2)}$ for all particles with $s_c < s_p^+$, i.e., discarding s_p^- (Figure 18a).

The approach was completed by defining an empirically derived s_p in the region of $s_{max} < \xi_c$, this is:

$$\frac{s_p^+}{s_{max}} = \frac{2 \times 10^7}{3} A s_{max}^{-0.3824} \tag{64}$$

The population splitting formulation has been shown to have great skill in capturing the behavior of s_{max} under a large set of aerosol and updraft inputs. The FN parameterization *Fountoukis and Nenes* [2005] which is based on the framework described aboves has been capable of reproducing observed cloud droplet concentrations [*Meskhidze et al.*, 2005].

6.3.1.1 Correction for inertially limited CCN

Based on detailed numerical simulations of the activation process, *Barahona et al.* [2010a] noted that when the activation process occurs in situations of weak updrafts, and the aerosol contains a significant number of large CCN, the FN parameterization exhibited a tendency to overestimate s_{max} and N_d. It was shown that this behavior originated in the assumptions made regarding the size of the inertially limited CCN. A simple correction for these 'inertially limited' particles was introduced by *Barahona et al.* [2010a]. Since the timescale for this particles to grow to D_{pc} is many times larger than the timescale of cloud formation, it was proposed that the condensation rate on this population could be estimated by approximating their size at s_{max} with their equilibrium diameter at $s = 0$, D_{p0}. Using Köhler theory, this can be shown to be equal to $D_{pc}/\sqrt{3}$ [*Barahona et al.*, 2010a].

However, this correction term, which improves the predictions of the parameterization when there is significant presence of large CCN, was applied to all the population II particles, inadvertently overestimating the water uptake by this entire population.

6.3.2 The "population splitting" concept revisited

We aim to improve two main aspects of the parameterization framework of *Nenes and Seinfeld* [2003] and *Barahona et al.* [2010a]. First, to better account for the size of large CCN, so their contribution to supersaturation depletion can be quantified correctly, avoiding biasing it high or low. The second goal is to avoid the discontinuity in $s_p^{\pm}$ introduced in equation (64). As s_{max} approaches ξ_c from the right, $s_p^{\pm}$ from equation (63) approaches $1/\sqrt{2}$. However, the value of s_p^{+} for $s_{max} = \xi_c$ in equation (64) is in general, not equal to $1/\sqrt{2}$. This creates a discontinuity in the parameterization response in scenarios where s_{max} shifts from the $s_{max} < \xi_c$ regime, to the $s_{max} > \xi_c$.

The first goal is attained by recognizing, as *Barahona et al.* [2010a], that neither $D_p^{(1)}$ or $D_p^{(2)}$ are appropriate approximations for the size of the largest CCN particles. However, instead of merging all CCN with $s_c < s_p^{+}$ in the same population (Region - I in figure 18) we consider that only the largest particles, those with $s_c < s_p^{-}$, should be approximated as in *Barahona et al.* [2010a], i.e., $D_p^{(3)} \approx D_{pc}/\sqrt{3}$. Similarly, and to maintain consistency and avoid overestimation of the water uptake, D_p for CCN with $s_p^{+} > s_c > s_p^{-}$ are approximated with equation (62)

$$D_p^{(1)} \approx D_{pc}(s_c) = \frac{2A}{3s_c} \tag{65a}$$

$$D_p^{(2)} \approx \left(\frac{G}{\alpha w}\right)^{1/2} \left(s_{max}^2 - s_c^2\right)^{1/2} \tag{65b}$$

$$D_p^{(3)} \approx D_{p0}(s_c) = \frac{2A}{3\sqrt{3}s_c} \tag{65c}$$

and the integral $I(0, s_{max})$ is naturally split in the different components:

$$s_{max}\left[I(0, s_p^{-}) + I(s_p^{-}, s_p^{+}) + I(s_p^{+}, s_{max})\right] = \beta \tag{66}$$

The second goal is achieved by defining the partition supersaturation for $s_{max} < \xi_c$ such that it transitions smoothly to the regime where CCN is completely dominated

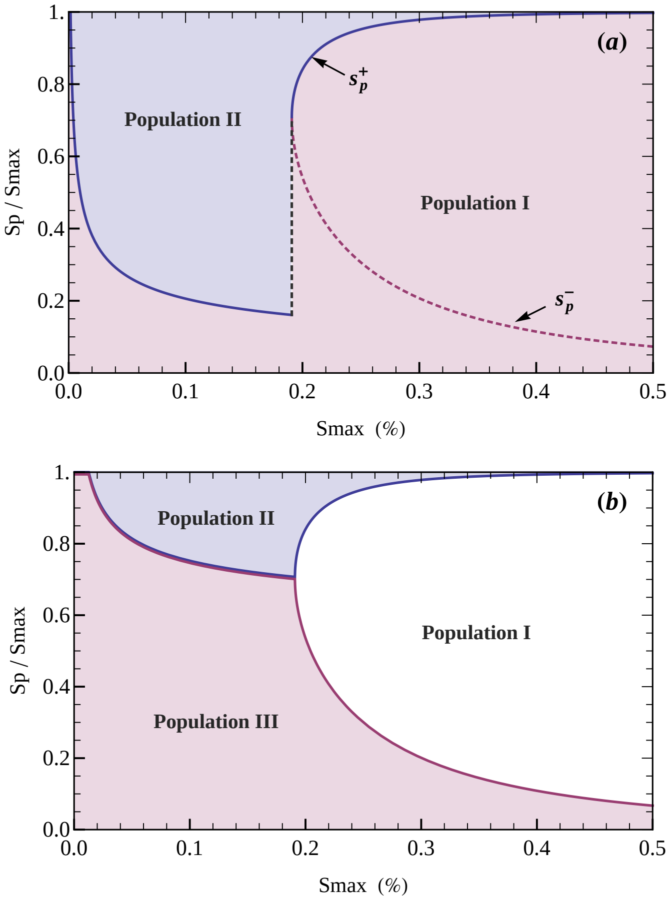

Figure 18: The 'partitioning supersaturations' $s_p^{\pm}$ illustrated in the s_c-s_{max} space. a) The s_c-s_{max} space as used in *Nenes and Seinfeld* [2003] and *Barahona et al.* [2010a]; and b) as used in this study. The example here is for a vertical velocity $w = 0.1ms^{-1}$

by inertially limited particles. Noting that as $s_{max} \rightarrow \xi_c$, both roots became identical $s_p^+ = s_p^-$ and both approach the value $1/\sqrt{2}$, we define s_p as:

$$\frac{s_p^{\pm}}{s_{max}} = \frac{2A \times 10^7}{3}(s_{max}^{-0.3824} - \xi_c^{-0.3824}) + \frac{1}{\sqrt{2}} \tag{67}$$

which maintains the same empirically derived dependence on s_{max}, but solves the discontinuity issue in the original framework of *Nenes and Seinfeld* [2003]. From this expression the vanishing of the term $I(s_p^-, s_p^+)$ emerges naturally for $s_{max} < \xi_c$, since both roots collapse to the same value. The regions where each approximation should be used are depicted in Figure 18b.

6.3.3 Numerical Implementation

The modifications proposed here can be implemented in the existing *Barahona et al.* [2010a] framework without the need of any major changes. Using the functions $I_1(0, s_p)$ and $I_2(s_p, s_{max})$ whose formulas are given in *Nenes and Seinfeld* [2003] for sectional, and in *Fountoukis and Nenes* [2005] for lognormal aerosol size distribution, $I(0, s_{max})$ is simply given by the following expression,

$$I(0, s_{max}) = \frac{1}{\sqrt{3}} I_2(0, s_p^-) + I_2(s_p^+, s_{max}) + \left[I_1(0, s_p^+) - I_1(0, s_p^-)\right] \tag{68}$$

which can be implemented with only minimal adjustments to codes that use the original population splitting concept. This formulation can be easily extended to the formulation of *Barahona and Nenes* [2007] that includes the effect of entrainment and mixing in the supersaturation development. If the fractional entrainment rate is given by e, then, the condensation rate is reduced, and equation (58) is transformed to

$$I(0, s_{max}) = \beta^\star = \beta(1 - \mu/\mu_c) \tag{69}$$

where μ_c is the critical entrainment rate.

6.4 Results

6.4.1 Parameterization evaluation

The augmented parameterization was tested against results from a numerical parcel model simulations of droplet number and s_{max}. For this purpose we employed off-line aerosol fields from MAM3, which is a 3-mode lognormal aerosol model. The characteristics of the test aerosol fields are described in Table 11. The results show a significant improvement in the accuracy and precision of the parameterized N_d and s_{max} values, without any appreciable increase in the computational cost.

Table 11: Size distribution parameters for the 3-modal aerosol size distribution used for evaluation of the parameterization. Each log-normal mode is characterized by the number concentration n_{a_i}, geometric standard deviation σ_{g_i}, geometric mean diameter d_{g_i}, and the hygroscopicity of the mode κ_{a_i}

Aerosol mode	σ_{g_i}	n_{a_i} (cm^{-3})	d_{g_i} (μm)	κ_{a_i}
Aitken	1.6	40 - 200	0.004 - 0.055	0.6
Accommodation	1.8	30 - 510	0.13 - 0.35	0.5
Coarse	1.8	0.1 - 5	1.0 - 4.0	1.1

Table 12: Summary of comparisons against parcel model simulations expressed as $\epsilon \pm \sigma_\epsilon$

Activation Parameterization	s_{max}	N_d
Fountoukis and Nenes [2005]	$+31\% \pm 25\%$	$+7.8\% \pm 9.7\%$
Barahona et al. [2010a]	$-24\% \pm 7\%$	$-10\% \pm 7.8\%$
This work	$-6.0\% \pm 6.2\%$	$-2.7\% \pm 4.8\%$

Figure 19a and Table 12 summarize the results of the validation. When FN was used, the relative error in s_{max} was on average +31% ± 25% while in N_d was of +7.8% ± 9.7%. Both numbers indicate a slight overestimation in both fields for the conditions explored. Figure 19b shows a similar analysis for the *Barahona et al.* [2010a] parameterization, with a relative error for s_{max} of −24% ± 7%, and N_d of −10% ± 7.8%, showing a tendency to underestimation for BN.

The relative error when using the parameterization with the modifications proposed in this work were considerably lower, being −6.0% ± 6.2% for s_{max}, and −2.7% ± 4.8% for N_d. For both fields there is a marked decrease in both the avearge error (a measure of parameterization bias) and in the dispersion of the errors (a measure of the parameterization accuracy). Figure 20 show the results of the comparison against parcel model for the case of N_d.

6.5 Conclusions

The “population splitting” concept of *Nenes and Seinfeld* [2003] and *Barahona et al.* [2010a] was modified to accurately account for the condensation rate of inertially limited CCN. The modifications to this parameterization framework were shown to improve the accuracy and precision for predictions of cloud droplet number concentration N_d and maximum supersaturation s_{max}. Implementation of this modifications is straightforward and does not require any major modifications to the previous formulations. The impact of these changes is expected to be larger in environments dominated by highly hygroscopic coarse mode aerosol, such as marine environments far from pollution sources.

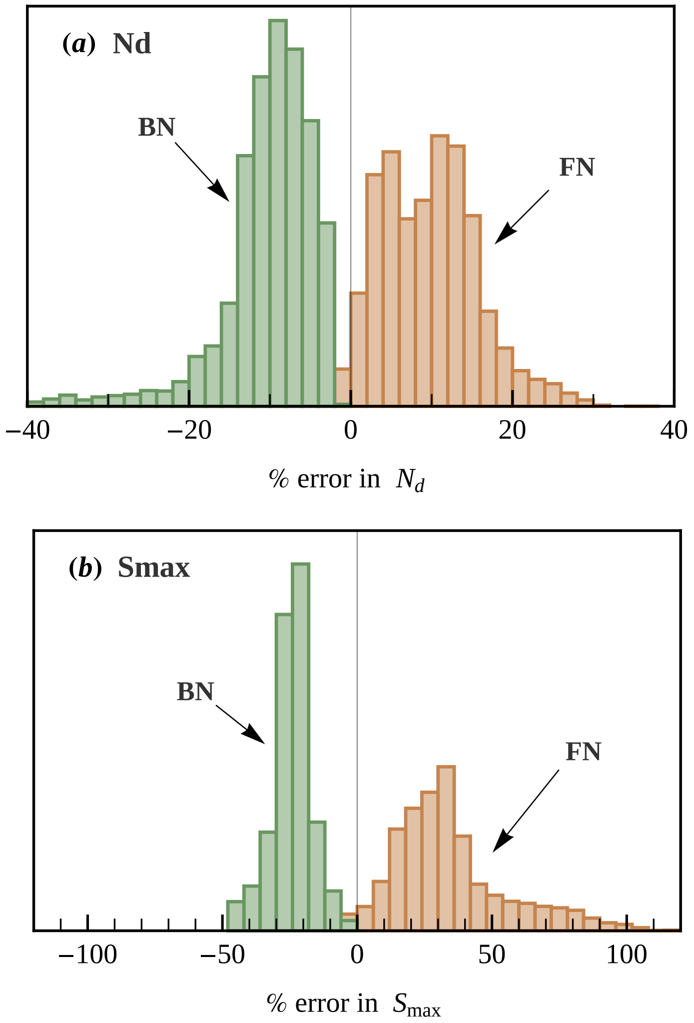

Figure 19: Histogram of the frequency of occurrence for the relative error $e = 1 - X_{param}/X_{PM}$, with X_{param} is the parameterized value, and X_{PM} is the value from parcel model simulations. (a.) for the droplet number N_d, (b.) for the maximum supersaturation s_{max}

.

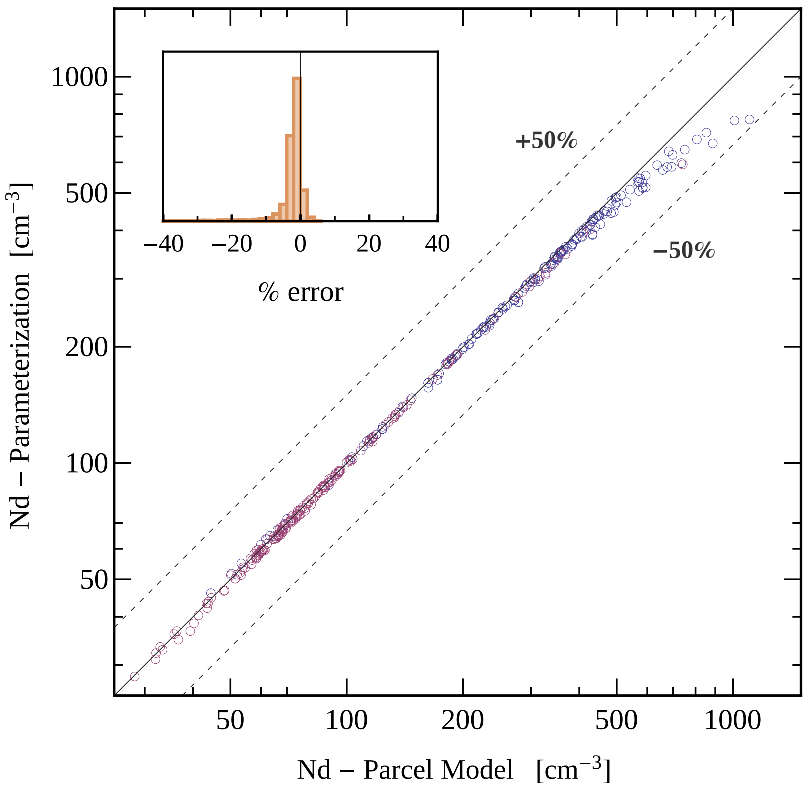

Figure 20: Comparison between parcel model simulations and predictions the parameterization. Blue circles correspond to marine aerosol while red circles are for continental aerosol. The inset is an histogram of the relative error between parcel model and parameterization derived N_d.

CHAPTER VII

WORLDWIDE DATA SETS CONSTRAIN THE WATER VAPOR UPTAKE COEFFICIENT IN CLOUD FORMATION

7.1 Summary

Cloud droplet formation depends on the condensation of water vapor on ambient aerosols, the rate of which is strongly affected by the kinetics of water uptake as expressed by the condensation (or mass accommodation) coefficient, α_c. Estimates of α_c for droplet growth from activation of ambient particles vary considerably and represent a critical source of uncertainty in estimates of global cloud droplet distributions and the aerosol indirect forcing of climate. We present an analysis of ten globally-relevant data sets of cloud condensation nuclei to constrain the value of α_c for ambient aerosol. We find that rapid activation kinetics ($\alpha_c > 0.1$) is uniformly prevalent. This means that uncertainty in water vapor accommodation on droplets is less than previously thought and resolves a long-standing issue of cloud physics.

7.2 Introduction

Atmospheric aerosols affect the radiative balance of the Earth, directly through absorption and scattering of solar radiation, and indirectly by influencing the microphysical properties, abundance, and lifetime of clouds. The magnitude of the indirect aerosol radiative forcing represents the most uncertain component of the estimated

---

This chapter contain excerpts from reference *Raatikainen et al.* [2013], to which the author of this dissertation contributed as a co-author, performing and analyzing the results of global climate model simulations. Experimental data, data analysis and its description was performed by fellow group members and colleagues.

anthropogenic effect on climate [*Intergovernmental Panel on Climate Change*, 2007]. Cloud properties are intimately tied to the activation of individual aerosol particles and subsequent growth of the newly formed droplets by accretion of water vapor. This process depends on the rate of transfer of water vapor to droplets; the fraction, α_c, of water molecules impinging on the surface of droplets that are incorporated in the droplet.

The value of α_c has been a subject of research for decades; it is commonly determined as an adjustable parameter to match growth rate measurements of droplets containing a well-defined concentration of solute [*Mozurkewich*, 2008; *Kolb et al.*, 2010]. The prevailing view is that α_c for a pure water surface is close to unity. Actual cloud droplets however may contain solutes or surface films that affect growth kinetics even at low concentrations [*Feingold and Chuang*, 2002], since slow solute dissolution [*Asa-Awuku and Nenes*, 2007] may suppress droplet growth rates. The "effective" α_c (that accounts for all water uptake processes) for droplets activated on ambient particles may be considerably lower than unity, with estimates of α_c for ambient droplets ranging from 10^{-5} up to 1.0 [*Chuang*; *Fountoukis et al.*, 2007; *Ruehl et al.*, 2008; *Ruehl et al.*; *Moore et al.*, 2012b]. The smallest values in this range are unlikely to be representative of the global aerosol population, but several of these studies report values of α_c between 10^{-1} and 10^{-2}, indicating significantly slower water uptake rates than that for pure water droplets.

Droplet formation in climate model simulations can be very sensitive to variations in α_c, owing to the dependence of cloud droplet number concentration (N_d) on the maximum supersaturation that develops in clouds. The latter is controlled by a balance between supersaturation generation (from radiative or expansion cooling) and depletion from condensation of water vapor on existing droplets. A smaller value of α_c results in slower water vapor condensation, allowing supersaturation to develop more fully and increasing N_d before reaching its maximum. This phenomenon is demonstrated by the sensitivity of global annual average vertical distributions of N_d to α_c, computed with a state-of-the-art climate model for preindustrial (Figure 21a) and current-day emissions (Figure 21b). As expected, N_d correlates directly with aerosol concentration. Decreasing α_c from 1.0 to 0.1 results in a 10-15% increase in N_d for current day emissions, while reducing α_c to 10^{-2} and 10^{-3} leads to considerable increases in N_d by factors of 1.5-1.8 and 2.0-2.5, respectively (Figure 21c). This N_d variability far surpasses the predicted 20-40% change in N_d between preindustrial and current-day emissions (for constant α_c; Figure 21d). The implication is that for aerosol-cloud-climate interaction studies, the extent to which α_c varies over space and time (especially if $\alpha_c < 0.1$) is critical in understanding its contribution to N_d variability, hence global cloud properties and climate. Little is known, however, concerning the spatial and temporal distribution of α_c. This uncertainty translates to a considerable, but unconstrained, source of uncertainty in estimating aerosol indirect forcing.

Measurements of the droplet size distribution resulting from exposure of aerosol particles to a given water vapor supersaturation, so-called Cloud Condensation Nuclei (CCN) data, can provide the fundamental information upon which values of α_c can be inferred. A recently developed numerical model, that simulates droplet growth in the Droplet Measurement Technologies CCN instrument [*Raatikainen et al.*, 2012] is able to analyze large field and laboratory data sets while comprehensively accounting for supersaturation depletion effects [*Lathem and Nenes*, 2011], variations in instrument operation parameters, and dry particle size distributions and hygroscopicity. The first applications of the model to ambient CCN data sets, one collected close to the Deepwater Horizon oil spill site *Moore et al.* [2012b] and the other transecting forest fire plumes [*Raatikainen et al.*, 2012], demonstrated that supersaturation depletion effects and changes in dry particle size and hygroscopicity distributions caused depressions in observed droplet size which TDGA would incorrectly interpret as changes in α_c.

Table 13: Globally representative data sets considered in this study. The growth kinetics analysis of the FAME and DWH data sets is published elsewhere; analysis of the other eight data sets is presented in the Supplementary Material. ICARTT *Medina et al.* [2007], EUCAARI *Cerully et al.* [2011], MIRAGE *Lance et al.* [2013], AMIGAS *Padró et al.* [2012], GoMACCS *Lance et al.* [2009], ARCPAC *Moore et al.* [2011], ARCTAS *Lathem et al.* [2013], CalNex *Moore et al.* [2012a], FAME *Bougiatioti et al.* [2009, 2011], DWH *Moore et al.* [2012b]

Campaign	Location	Dates	Supersaturation
ICARTT	New Hampshire, USA	7/04-8/04	0.2–0.6 %
EUCAARI	Hyytiälä, Finland	3/07-5/07	0.1–1.8%
MIRAGE	Mexico City, Mexico	4/06	0.07–1.05%
AMIGAS	Atlanta, Georgia, USA	8/08-9/08	0.2–1.0%
GoMACCS	Texas, USA	8/06-9/06	0.3–1.0%
ARCPAC	Alaska, USA	4/08	0.1–0.6%
ARCTAS	Saskatchewan, Canada	7/08	0.20–0.57%
CalNex	California, USA	5/10	0.31–0.34%
FAME	Finokalia, Crete	7/07-10/07	0.2–0.73%
DWH	Gulf of Mexico	6/10	0.31%

Extending the analysis to ambient CCN data sets of global relevance provides a novel constraint on the variability of α_c and its dependence on source type and chemical composition.

The eight data sets analyzed here (Table 13 and Figure 24) are large and representative of many different locations and conditions, including urban outflows, boreal forests, Arctic air masses, fresh and aged biomass burning plumes, and continental air with anthropogenic and biogenic influences. We also include two previous studies on the activation kinetics of aged marine air in the Eastern Mediterranean [*Bougiatioti et al.*, 2009, 2011] and near a strong hydrocarbon source at Deepwater Horizon [*Moore et al.*, 2012b]. A detailed description of the data sets and the instrumentation deployed during each individual campaign is available in the reference in Table 13.

7.3 Results from Dataset analysis

To study whether the observed depressed size is from $\alpha_c < 0.1$, instrument variability, supersaturation depletion effects, or variability in aerosol size distribution and hygroscopicity, we apply an approach proposed by *Raatikainen et al.* [2012] that is insensitive to observation and prediction biases. Since activated droplet size is a function of aerosol size distribution, hygroscopicity, instrument operating conditions (accurately known) and α_c (not known), one can simulate the activation and growth of CCN in the Droplet Measurement Technologies CCN counter using a prescribed (constant) α_c. If the difference between observed and predicted droplet size is essentially constant for all of the data, then assuming constant α_c is valid. Indeed this is found to be the case for our globally-relevant data sets. Prescribing α_c =0.2 (which is representative of fast activation kinetics; *Raatikainen et al.* [2012]) captures the temporal variability of measured droplet size to within a constant bias and a 0.3μm variance, which characterizes normal instrument variability and the essentially unresolvable range of α_c between 0.1 and 1.0 *Raatikainen et al.* [2012]. With this result and the fact that TDGA suggests that the majority of particles activate as rapidly as $(NH_4)_2SO_4$, one concludes that α_c >0.1 is globally representative. Regions of the globe not directly sampled (e.g., Eastern Asia, Amazon) generally follow one of the airtypes of Table 1; CCN activation kinetics of globally important secondary organic aerosol generated in environmental chambers further support the model of rapid activation (See Supplementary Material).

Important implications arise from our results. First, α_c is effectively constant for all the data considered, even for particles composed largely of organics with very low oxygen content. This implies that anthropogenic (compositional) impacts on α_c are essentially limited to the 0.1-1.0 range, considerably reducing the uncertainty for cloud droplet number prediction in climate models. This resolves a decades-long uncertainty in cloud physics on the value of α_c, as it appears that α_c for ambient aerosol can be represented in models with a constant value in the 0.1-1.0 range.

7.4 CCN Instrument Model Description

The coupled instrument and droplet growth model *Raatikainen et al.* [2012], freely available at http://nenes.eas.gatech.edu/Experiments/CFSTGC.html, calculates flow velocity, pressure and supersaturation profiles from the measured sample pressure, column temperatures, sample and sheath flow rates, and calibrated maximum supersaturation. Flow velocities and supersaturation profiles are then used in a Lagrangian droplet growth model to calculate the growth and activation of CCN as they flow through the instrument chamber. The growth model input parameters are α_c, dry particle size distributions and hygroscopicity. Number concentrations are needed to account for water vapor depletion effects as CCN chamber supersaturation is decreased due to water vapor condensation on growing droplets, leading to coupling between the instrument and droplet growth models *Lathem and Nenes* [2011].

7.5 Global Simulations

The impact of the mass accommodation coefficient α_c on cloud properties and indirect aerosol radiative forcing was estimated using the Community Atmosphere Model (CAM5.1), which is a state-of-the-art atmospheric general circulation model with fully coupled aerosol-cloud interactions *Liu et al.* [2012]. We used the model configured with the finite volume dynamic core, with a horizontal resolution of $1.9° \times 2.5°$, and 30 levels in the vertical. The 3-mode version of the modal aerosol module (MAM3) was used, which considers aerosol sulfate, ammonium, nitrate, primary organic matter, secondary organic aerosol, black carbon, sea salt, and dust; particles are distributed into Aitken, accumulation, and coarse lognormal modes with prescribed geometric standard deviation. The mode diameter varies as aerosol number and total mass change. The MAM3 is coupled to a double moment cloud microphysics scheme. Particles can be removed by wet removal mechanisms, or regenerated to interstitial aerosol after cloud droplets evaporate. Activation of aerosol to cloud droplets is calculated with the *Fountoukis and Nenes* [2005] parameterization which includes the effect of α_c on the activation process. Simulations with $\alpha_c = 1$, 10^{-1}, 10^{-2}, and 10^{-3} were performed for current-day and preindustrial emissions of aerosol precursors, with climatological sea surface temperatures and ice cover. Emissions data sets used in the simulations are those of *Lamarque et al.* [2010] for both present day (year 2000) and preindustrial simulations (year 1850). Vertical distribution of emissions follow the protocol of *Dentener et al.* [2006]. The reported fields of in-cloud droplet number concentrations correspond to the annual average from the last 5 years of simulation, after allowing one year of simulation for spin-up. The annual average spatial distribution of cloud number concentrations are provided for preindustrial (Figure 22) and current-day (Figure 23) emissions. These figures correspond to annual average N_d at the 936 hPa pressure level, for preindustrial and current day simulation, respectively. In all these figures, results are shown for α_c=1.0 (top left panels), 10^{-1} (top right panels), 10^{-2} (low left panels) and 10^{-3} (low right panels).

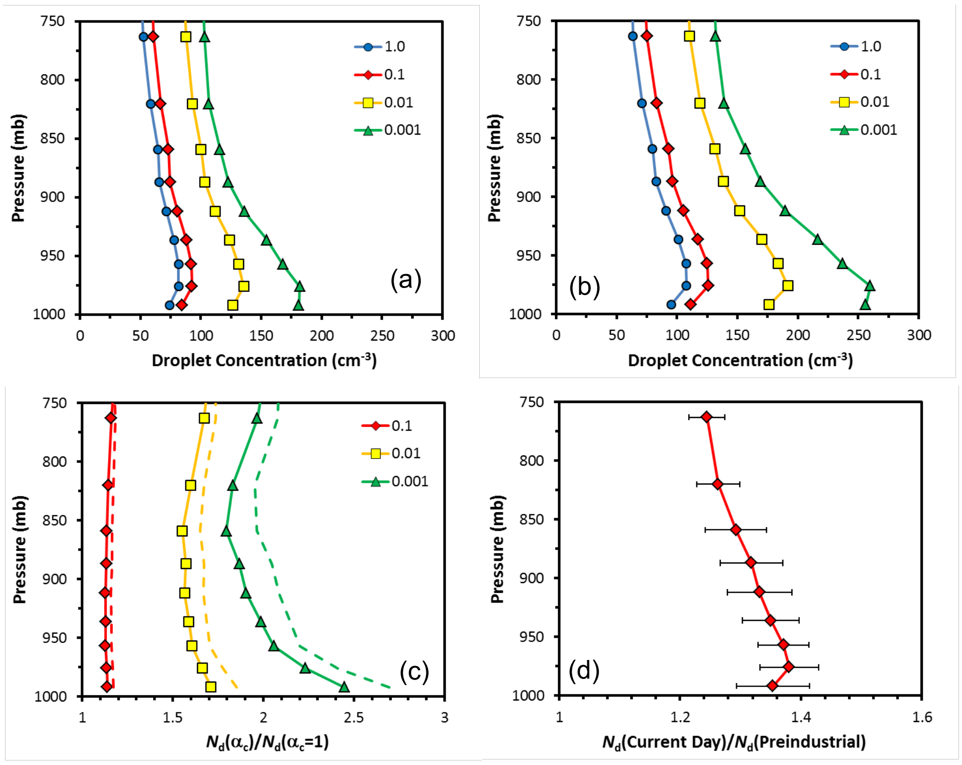

Figure 21: Global annual average vertical distributions of cloud droplet number concentration (N_d) computed with the NCAR Community Atmosphere Model 5.1 for (a) preindustrial emissions with fixed α_c, and (b) current-day emissions with fixed α_c. (c) N_d for fixed value of α normalized by those computed for α_c=1, for preindustrial (solid line) and current-day (dashed line) emissions. (d) N_d for current-day emissions normalized with those for preindustrial emissions. Curve represents average of all constant α_c simulations, while error bars reflect the corresponding standard deviation

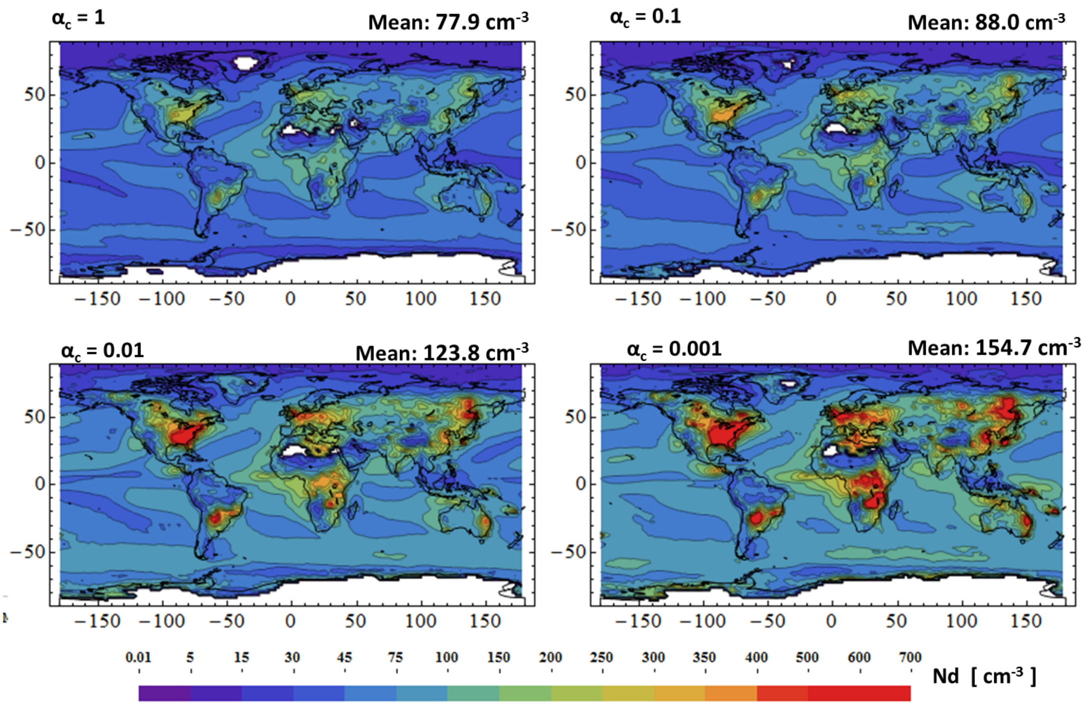

Figure 22: Annual average cloud droplet number concentration for preindustrial emissions (936 mb pressure level). Number at the top right corner of each subplot represents the global annual average mean concentration. Results are shown for α_c=1.0, 10^{-1}, 10^{-2}, 10^{-3}.

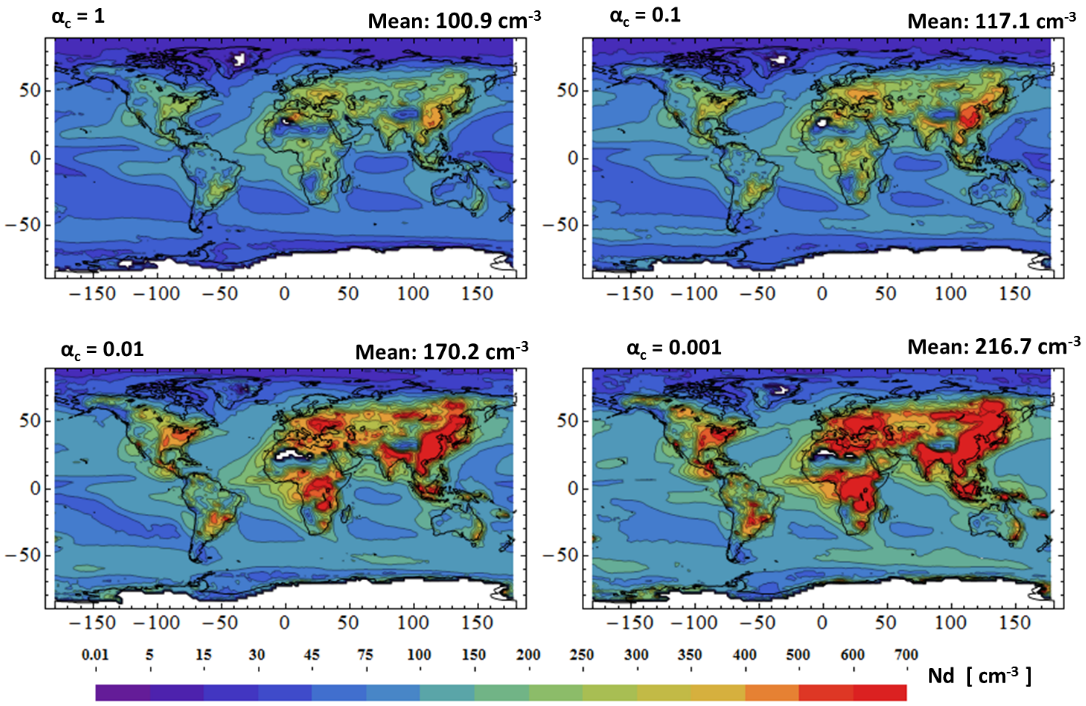

Figure 23: Similar to Figure 22, but for current day emissions.

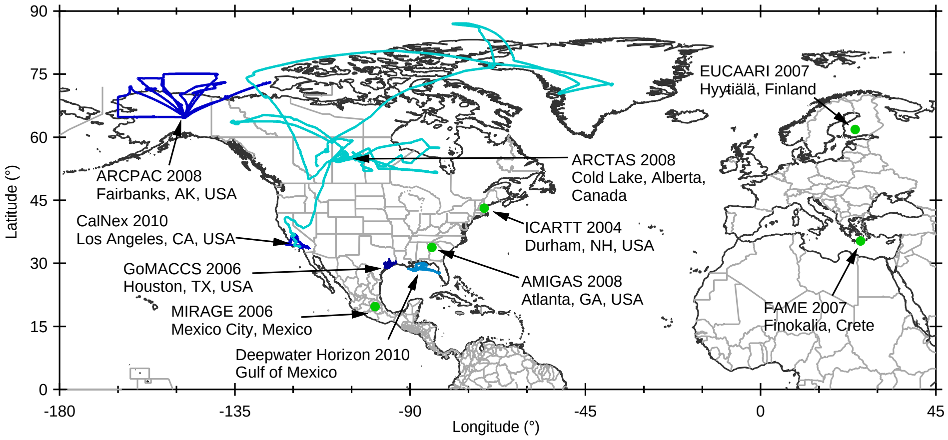

Figure 24: Campaign sites (green markers) and flight tracks (light and dark blue lines) of the globally representative data sets considered in this study. Analysis of the data sets is presented in the Supplementary Material, *Bougiatioti et al.* [2009, 2011] and *Moore et al.* [2012b].

CHAPTER VIII

SENSITIVITY OF CIRRUS AND MIXED-PHASE CLOUDS TO THE ICE NUCLEI SPECTRA IN MCRAS-AC: SINGLE COLUMN MODEL SIMULATIONS

8.1 Summary

The salient features of mixed-phase and ice clouds in a GCM cloud scheme are examined using the ice nucleation parameterizations of Liu and Penner (LP) and Barahona and Nenes (BN). The performance of both parameterizations was assessed in the GEOS-5 AGCM using the McRAS-AC cloud microphysics framework in single column mode. Four dimensional assimilated data from the intensive observation period of ARM TWP-ICE campaign was used to drive the fluxes and lateral forcing. Simulation experiments were established to test the impact of each parameterization in the resulting cloud fields. Three commonly used IN spectra were utilized in the BN parameterization to describe the availability of IN for heterogeneous ice nucleation. The results showed large similarities in the cirrus cloud regime between all the schemes tested, in which ice crystal concentrations were within a factor of 10 regardless of the parameterization used. In mixed-phase clouds there were some persistent differences in cloud particle number concentration and size, as well as in cloud fraction, ice water mixing ratio, and ice water path. Contact freezing in the simulated mixed-phase clouds contributed to the effective transfer of liquid to ice, so that on average, the clouds were fully glaciated at $T\sim260\,\mathrm{K}$, irrespective of the ice

---

This chapter appears as reference *Morales et al.* [2012]

nucleation parameterization used. Comparison of simulated ice water path to available satellite derived observations were also performed, finding that all the schemes tested with the BN parameterization predicted average values of IWP within ±15% of the observations.

8.2 Introduction

The role of atmospheric aerosols in modulating the atmospheric radiative balance, by directly scattering solar radiation, or indirectly, by modifying cloud optical and microphysical properties, has received considerable attention during the last couple of decades. Soluble and insoluble aerosol species provide nucleation sites for the atmospheric water vapor to form liquid droplets (Cloud Condensation Nuclei, CCN), and ice crystals (Ice Nuclei, IN) respectively. The important interactions between aerosol particles and cloud optical and physical properties operate at temporal and spatial scales unresolved by Global Climate Models (GCMs); their inclusion in climate simulations therefore relies on parameterizations. The importance of these aerosol–cloud interactions, and their potential impact on climate, makes their inclusion in climate models through accurate and physically based schemes a high priority [*Intergovernmental Panel on Climate Change*, 2007].

Aerosol indirect effects (AIE) in warm clouds have been long studied and implemented in atmospheric models [e.g., *Penner et al.*, 2006], but less has been accomplished for cold clouds. Modifications to the number density and sizes of ice crystals not only strongly affect the radiative properties of ice-bearing clouds, but also impacts the development of precipitation [e.g., *Lohmann and Diehl*, 2005; *Lohmann*, 2002]. The complexities associated with cold clouds, both mixed-phase and ice-only clouds (due in part to the concurrent action of different freezing mechanisms, the high selectivity of the IN process, and the theoretical uncertainties associated with their description) have challenged the representation of such clouds in GCMs, most of which lack explicit ice microphysics [*Lohmann and Feichter*, 2005]. As a result, even the sign of the radiative effects of aerosol-ice cloud interactions remains uncertain in climate simulations.

Important steps to improve the simple treatments of cirrus and mixed-phase cloud originally included in GCMs have been undertaken in recent years. For example, the partitioning of cloud condensate between ice and liquid water in mixed-phase clouds ($235\,\mathrm{K} \leq T \leq 273\,\mathrm{K}$) was typically represented by a temperature-only approach [e.g., *DelGenio et al.*, 1996; *Rasch and Kristjánsson*, 1998]. This approach has been progressively replaced by a less empirical and more physically-based representation, in which the deposition growth of cloud ice at the expense of the liquid water, the Bergeron-Findeisen process [*Pruppacher and Klett*, 1997], is taken into account [e.g., *Rotstayn et al.*, 2000]. This prognostic approach for condensate partitioning which includes explicit dependence of the deposition rate on microphysical variables such as ice content q_i, and ice crystal concentration, N_c, has been adopted by a variety of GCMs [*Sud and Lee*, 2007; *Liu et al.*, 2007; *Salzmann et al.*, 2010].

Another advancement in GCM cloud schemes is the implementation of two-moment cloud microphysics, which include prognostic equations for the mass as well as number concentration of different hydrometeor categories [e.g., *Seifert and Beheng*, 2001, 2006; *Morrison and Gettelman*, 2008]. This has permitted the prognostic computation of cloud particles sizes and deposition rates [e.g., *Salzmann et al.*, 2010; *Muhlbauer and Lohmann*, 2009].

Estimates of the AIE on ice-bearing clouds require an adequate description of the aerosol-cloud coupling through the nucleation process. That is, the prognostic calculation of hydrometeor sizes should be done in a manner consistent to aerosol load changes and aerosol characteristics. However, an efficient and comprehensive representation of the ice nucleation process in the framework of a GCM has proven difficult. Most ice nucleation parameterizations rely on simple functions to determine how many ice crystals will be heterogeneously nucleated at a given set of environmental conditions. These relations describing the availability of IN, termed IN spectra, exhibit different level of complexity, ranging from saturation-dependent schemes [e.g., *Meyers et al.*, 1992; *Phillips et al.*, 2007] to IN spectra with aerosol-dependent parameters derived empirically [e.g., *Connolly et al.*, 2009; *Niedermeier et al.*, 2010; *Phillips et al.*, 2008]. Theory-based approaches have also led to formulations of IN spectra with explicit dependence on aerosol number concentration, aerosol size distribution, and aerosol surface properties [*Khvorostyanov and Curry*, 2009; *Barahona and Nenes*, 2009b; *Barahona*, 2012]. A comprehensive review of IN parameterizations developed from laboratory studies, observations, and theory is provided in *Hoose and Möhler* [2012]. Most GCM microphysical schemes that account explicitly for aerosol effects represent ice nucleation assuming that there is no variation in ice nucleation properties within an aerosol species. In reality, there is large variability in the ice nucleation properties of aerosol populations, which contributes to the large uncertainty in the predicted IN concentrations.

Homogeneous freezing of deliquesced aerosol (i.e., without the presence of a solid phase) may occur only at temperatures below 235 K, the homogeneous freezing threshold T_{hom} [*Pruppacher and Klett*, 1997]. For temperatures higher than T_{hom}, in which mixed-phase clouds typically exist, the presence of a solid phase is necessary for ice formation, and therefore only heterogeneous ice nucleation is active. Below T_{hom}, where ice-only clouds form, the supersaturation with respect to ice is the result of the competition between the rate of cooling of the cloud parcel and the deposition on nucleated ice crystals. Since homogeneous and heterogeneous ice nucleation may occur simultaneously, the competition from both mechanisms and their impact on supersaturation further complicate calculations. Therefore, the supersaturation in such situation varies dynamically given the amount of IN present and the dynamical forcing available. For this reason, Lagrangian simulations have been used to develop solutions to the variable supersaturation problem [e.g., *Lin et al.*, 2002], and fits to these numerical solutions have been used to develop ice nucleation parameterizations. A few such parameterizations have been developed [*Kärcher and Lohmann*, 2002, 2003; *Liu and Penner*, 2005], and have been implemented in GCM models [*Hoose et al.*, 2010]. Analytical solutions to this problem have been developed in which any IN spectrum can be used [*Barahona and Nenes*, 2009b].

For the case of mixed-phase clouds, liquid water, water vapor, and ice are simultaneously present, and can exhibit complex dynamics [e.g., *Korolev*, 2007]. For the coarse vertical resolution of GCM cloud schemes, the simplifying assumption that the water vapor is saturated with respect to liquid water is sometimes made. The supersaturation with respect to ice, S_i, is therefore constrained by thermodynamic equilibrium rather than by the competition of cooling and condensation. With this assumption, it is sufficient to know the availability of IN (given by an IN spectrum) at S_i to compute the nucleation rate of ice crystals.

A number of studies have focused on the implementation and evaluation of new microphysical schemes in GCM simulations, including prognostic calculation of the ice fraction in mixed phase clouds, and using more physically-based ice nucleation schemes [*Storelvmo et al.*, 2008; *Sud and Lee*, 2007; *Liu et al.*, 2007; *Salzmann et al.*, 2010]. *Curry and Khvorostyanov* [2012] performed a comparison of some heterogeneous nucleations parameterizations in a single-column model for long lived mixed-phase arctic clouds. However, none of these studies has performed sensitivity analysis of the simulated mixed-phase and cirrus clouds fields to different IN spectra.

In this study, we use the parameterization of *Barahona and Nenes* [2009b], BN hereafter, in which the ice nucleation problem is treated in a general framework that admits the use of any IN spectra, empirical or theoretical. *Barahona et al.* [2010b] used the BN parameterization to compare common formulations of the IN spectrum in a chemical transport model, finding that the 2 to 3 orders of magnitude variation in the IN concentrations among different schemes would lead to up to a factor of 20 variation in N_c in cirrus clouds. The sensitivity can be even larger in mixed-phase clouds where only heterogeneous ice nucleation is active, and competition for water vapor does not buffer the response of crystal number to IN concentration changes.

Testing the impact of IN spectra in a comprehensive cloud microphysical framework would provide valuable information on how the uncertainties associated with ice nucleation are reflected on the cloud field variables when coupled to other cloud processes. In this study, we report the implementation of the BN ice nucleation scheme into the Microphysics of Clouds with Relaxed Arakawa-Schubert and Aerosol-Cloud interaction (McRAS-AC) [*Sud and Lee*, 2007] driven by the Goddard Earth Observing System Model, version 5 (GEOS-5). The flexibility provided by the BN ice nucleation parameterization is ideal for testing the sensitivity of the simulated cloud properties to the representation of IN spectra in the McRAS-AC framework. To isolate the response from the underlying physical parameterization, all the simulations were performed in the Single Column Model version of GEOS-5. This is a common test of GCM microphysics since the SCM configuration contains the same physical parameterizations as the host GCM model, with the advantage of a much smaller computational burden, and the laterally constrained input flux fields allows better delineation of the role of microphysical processes of cloud formation and aerosol effects. The simulations were forced with data collected during the Tropical Warm Pool International Cloud Experiment (TWP-ICE) intensive observation period (IOP) of the ARM program [*May et al.*, 2008], that took place around Darwin, Australia in early 2006.

8.3 Model description and simulation set-up

A detailed description of the McRAS-AC microphysics can be found elsewhere [*Sud and Walker*, 1999; *Sud and Lee*, 2007; *Bhattacharjee et al.*, 2010]. Here we will primarily focus on describing the treatment of ice-only and mixed-phase clouds microphysics in McRAS-AC.

8.3.1 Ice Nucleation in McRAS-AC

McRAS-AC has the option to invoke either the *Liu and Penner* [2005], (LP), or the *Barahona and Nenes* [2008, 2009a,b] parameterizations to describe the ice nucleation process. This capability was used to assess and compare the performance of the two schemes.

The LP parameterization was originally designed to describe the nucleation process at temperatures typical of cirrus cloud formation, i.e., for temperature less than the homogeneous freezing threshold ($T_{\mathrm{hom}} = 235\,\mathrm{K}$). It is based on numerical correlations derived from statistical fits to a large number of Lagrangian parcel model simulations, in which homogeneous and heterogeneous freezing mechanisms were explicitly accounted for. The homogeneous freezing of deliquesced sulfate aerosol was approached using an effective freezing temperature. Immersion freezing on soot particles was included in the parcel model simulations leading to the LP parameterization by using classical nucleation theory, in which a fixed aerosol size distribution and freezing characteristics were assumed. Deposition freezing is calculated using the *Meyers et al.* [1992] formulation. In this way, the LP parameterization takes into consideration the impact of updraft velocity, w, and aerosol load N_a on the number concentration of nucleated ice crystals, $N_{\mathrm{c,nuc}}$. In the cirrus regime, it is capable of calculating $N_{\mathrm{c,nuc}}$ as the result of the competition of both freezing mechanisms. For temperatures above T_{hom}, homogeneous freezing is inactive, and $N_{\mathrm{c,nuc}}$ is given solely by heterogeneous nucleation. However, because the scheme obtains the number of nucleated ice crystals from curve-fitted functions of temperature and vertical velocity, these specific equations may not hold as well when extrapolated beyond the curve-fit data domain, nor be applied to aerosols that do not follow the prescribed freezing properties used in the simulations.

The implementation of LP in McRAS-AC for mixed-phase clouds ($T_{\text{hom}} < T < 273\,\text{K}$) follows closely that of *Liu et al.* [2007], and was described and tested in a SCM framework [*Bhattacharjee et al.*, 2010]. In this regime, $N_{\text{c,nuc}}$ is calculated by adding the contributions from the numerical correlations described above and the contribution from deposition freezing as given by a modified version of the *Meyers et al.* [1992] formula,

$$N_{\text{id}}(S_i) = f(z)N_0\exp(a + b(S_i - 1)) \tag{70}$$

where N_{id} is the number concentration of ice crystals due to deposition nucleation in m^{-3}, $N_0 = 10^{-3}\,\text{m}^{-3}$, $a = -0.639$, and $b = 0.1296$, and $f(z)$ is an empirical height correction factor, given by $f(z) = 10^{(z_0 - z)/\delta z}$, with $z_0 = 1\,\text{km}$, $\delta z = 6.7\,\text{km}$, and $f(z) \in [0.12, 1.0]$. This decay factor was derived from observations by *Minikin et al.* [2003] during the INCA (Interhemispheric Differences in Cirrus Properties from Anthropogenic Emissions) campaign, to augment the formula by *Meyers et al.* [1992] that was derived from ground-level observations.

In the present work we also implemented and tested the BN parameterization in McRAS-AC. BN is based on an analytical solution of the governing equations of a cooling air parcel in which deliquesced aerosol and heterogeneous IN are allowed to freeze and grow by water vapor deposition [*Barahona and Nenes*, 2008, 2009a,b]. Accordingly, BN circumvents the need for curve-fitted equations, and holds for a wide range of configurations encountered in the physical system. The availability of IN in the BN parameterization can be described with any heterogeneous nucleation parameterizations. Here we use the correlations of *Meyers et al.* [1992] (MY92), *Phillips* *et al.* [2008] (PDA08), and the semi-empirical spectra derived from classical nucleation theory of *Barahona and Nenes* [2009b], (CNT). MY92 is a widely used, empirical IN spectrum which depends only on S_i, which we use here in its original form, without the height correction factor $f(z)$. PDA08 is also empirical, but it considers separately the contribution of organics, dust, and black carbon to the IN population for a given supersaturation. CNT is based on an approximation of classical nucleation theory to calculate IN concentration as a function of supersaturation, and accounts for the impact of aerosol number and freezing properties of different aerosol species to the IN spectrum. For temperatures below T_{hom}, BN calculates the competing effects of homogeneous nucleation on deliquesced aerosol and the heterogeneous freezing for the availability of water vapor in a forming cirrus cloud. The maximum supersaturation with respect to ice attained in the ascending parcel, $S_{\mathrm{i,max}}$, is calculated by balancing the depletion effect from deposition growth of ice crystals and the availability of water vapor from cooling. In this way, $S_{\mathrm{i,max}}$ is given by the dynamics of cooling and ice nucleation. BN then uses $S_{\mathrm{i,max}}$ to calculate $N_{\mathrm{c,nuc}}$.

The application of BN in the mixed-phase cloud regime differs slightly from that of LP. In the absence of any liquid water, the maximum supersaturation in the parcel would be dictated dynamically by expansion cooling and the IN concentration. However, in McRAS-AC, any initial condensate is considered to be liquid (*Rotstayn* [1997]) and it is then partitioned following *Rotstayn et al.* [2000]. Therefore, in practice, ice nucleation above T_{hom} is assumed to occur in an environment saturated with respect to water. Under this circumstance, $S_{\mathrm{i,max}}$ is fixed by the assumption of water saturation, equal to $S_{\mathrm{i,max}} = e_{\mathrm{sl}}(T)/e_{\mathrm{si}}(T)$, i.e., the ratio of the saturation vapor pressure over water and over ice, and it is therefore independent of the dynamic forcing, w, or aerosol loading. The number concentration of nucleated ice crystals, $N_{\mathrm{c,nuc}}$, is then calculated by direct application of the IN spectra at the given $S_{\mathrm{i,max}}$.

8.3.2 McRAS-AC cold cloud microphysics

The cloud microphysics in McRAS-AC include balance equations for the mixing ratios of liquid water, q_l, and cloud ice q_i. The precipitation microphysics are described by *Sud and Lee* [2007], which recast *Seifert and Beheng* [2006] to make it applicable to the thicker clouds of a coarse resolution GCM. The activation of aerosol to cloud droplets follows the parameterization of *Fountoukis and Nenes* [2005]. Aerosol mass concentrations are taken from the Goddard Chemistry Aerosol Radiation and Transport (GOCART), and log-normal size distribution for each species are prescribed, from which aerosol number concentrations are derived.

The partitioning of cloud condensate between ice and liquid in mixed-phase clouds is prognostic, and takes into account the Bergeron-Findeisen (BF) process, by which cloud droplets evaporate and the resulting water vapor deposits onto ice crystals. The process is represented following *Rotstayn et al.* [2000]. The scheme assumes that the water vapor is saturated with respect to liquid water, so that S_i is given by the ratio between the saturation vapor pressure over ice and over liquid water respectively, i.e., $S_i = e_{\mathrm{sl}}/e_{\mathrm{si}}$. Liquid water is evaporated to maintain saturation, so the net process is equivalent to a mass transfer from liquid water to ice. Under the assumption of monodisperse, spherical ice crystals, the rate of change of q_i by deposition is given by

$$\frac{dq_i}{dt} = \left(\frac{N_c}{\rho}\right)^{2/3} \frac{7.8q_i^{1/3}(e_{\mathrm{sl}} - e_{\mathrm{si}})}{\rho_i^{1/3}(A+B)e_{\mathrm{si}}} \tag{71}$$

which explicitly accounts for the dependence of the ice deposition rate on crystal number concentration, N_c. In Eq. (71), ρ and ρ_i are the densities of air and ice crystals respectively, and A and B represent mass diffusion and heat conduction coefficients associated with the deposition process [*Pruppacher and Klett*, 1997]. Equation (71) is then integrated analytically under the assumption that during one time step, Δt, all the temperature dependent quantities remain constant, so that over Δt, the change

Table 14: Simulations reported in this study. The simulation set-up for all the simulations is identical, and they only differ on the ice nucleation scheme. LP05 is the parameterization of *Liu and Penner* [2005]. BN stands for *Barahona and Nenes* [2009a].

Simulation ID	Contact Freezing	Ice-only Clouds (cirrus)	Mixed-Phase Clouds
LP-CTRL	Yes	LP05	*Meyers et al.* [1992]
LP-NoFrzc	No	LP05	*Meyers et al.* [1992]
BN-PDA08	Yes	BN09	*Phillips et al.* [2008]
BN-PDA08-NoFrzc	No	BN09	*Phillips et al.* [2008]
BN-CNT	Yes	BN09	*Barahona and Nenes* [2009a]
BN-MY92	Yes	BN09	*Meyers et al.* [1992]

in q_i is given by,

$$\Delta q_i = \min\left[q_l,\, CF\left(\frac{2}{3}c_{\mathrm{vd}}\Delta t + q_{\mathrm{i0}}^{2/3}\right)^{3/2}\right] \tag{72}$$

where CF is the cloud fraction, and c_{vd} is a coefficient equal to the left hand side of Eq. (71) divided by $q_i^{1/3}$, and q_{i0} is the assumed initial mixing ratio of cloud ice. The corresponding temperature increase due to the release of latent heat of fusion is applied to the grid-box mean temperature field.

Ice crystal number concentration N_c is determined in McRAS-AC by the processes of ice nucleation, both by homogeneous nucleation of deliquesced aerosols and heterogeneous ice nucleation, contact freezing of water droplets, melting of cloud ice, and freezing of supercooled water droplets below T_{hom}. The ice nucleation term is calculated with the LP and the BN parameterizations as explained in Sect. 8.3.1. Contact freezing of supercooled cloud droplets through Brownian coagulation with insoluble IN (mineral dust) is included as given by *Young* [1974] and *Muhlbauer and Lohmann* [2009]. Ice multiplication processes are not included in the calculation of ice crystal number concentration.

Aerosol input for ice nucleation is also based on GOCART aerosol climatology. A single mode log-normal size distribution was assumed for black carbon, with geometric mean diameter, $d_{\mathrm{g}} = 0.04\,\mu$m, and a geometric standard deviation $\sigma_{\mathrm{g}} = 2.3$ [*Jensen* *and Toon*, 1994]. Similarly, sulfate aerosol size distribution is assumed log-normal with $d_\mathrm{g} = 0.14\,\mu$m and $\sigma_\mathrm{g} = 1.5$ [*Pueschel et al.*, 1992]. The mass of mineral dust from GOCART is distributed in 3 log-normal modes, with geometric mean diameters of 0.16, 1.4, and 10μm respectively, and geometric standard deviations σ_g of 2.1, 1.9 and 1.6 respectively for each mode [*D'Almeida*, 1987]. The density of black carbon was assumed equal to 1 g cm^{-3} while for sulfates, we assumed the density of sulfuric acid (1.84 g cm^{-3}). Density of mineral dust was assumed equal to 2.5 g cm^{-3}. A probability distribution function of cloud scale vertical velocity, w, was used to represent the local variations of velocity at scales relevant for nucleation. The distribution was assumed to be a normal distribution, with mean, $\overline{w}$, equal to the large scale vertical velocity, and a fixed standard deviation $\sigma_w = 0.25\,\mathrm{ms}^{-1}$, consistent with the mean standard deviation observed in the INCA campaign for the cirrus regime [*Kärcher and Ström*, 2003]. The large-scale vertical velocity $\overline{w}$ in our simulations was found to be typically $\sim 0.05\,\mathrm{ms}^{-1}$. The sensitivity to σ_w was assessed by varying this parameter between 0.1 and $0.5\,\mathrm{ms}^{-1}$.

8.3.3 Forcing data

The SCM configuration consists of an isolated column of a global circulation model, and is therefore, a 1-dimensional time-dependent atmospheric model. The lateral forcing fields to the 72 pressure levels in the atmospheric columns of GEOS-5 are prescribed from assimilated 4D observational data. For the purpose of this study, we used the forcing from the TWP-ICE intensive observation period (IOP), derived by the Atmospheric Radiation Measurement (ARM) program. It includes data from 17 January to 12 February 2006. This data set has been previously utilized in forcing SCM simulations with the intent of testing ice microphysics for GCMs [*Wang et al.*, 2009a], as well as for comparing simulations produced with bulk microphysical schemes of varying complexity in a cloud resolving model with observational data

[*Wang et al.*, 2009b; *Lee and Donner*, 2011]. The TWP-ICE data is ideally suited for testing the representation of cold and mixed-phase clouds in models and is a frequently used test case that allows comparison with other existing studies [e.g., *Varble et al.*, 2011; *Fridlind et al.*, 2012]. It includes periods dominated by deep convective clouds and by persisting layers of cirrus clouds.

8.4 Simulated clouds fields

Table 14 summarizes the simulations considered in this study. The objective of the simulation experiments is to evaluate the sensitivity of the cloud fields to the treatment of ice nucleation. A "control" simulation was performed with the LP ice nucleation parameterization as described above, which has been previously used in the McRAS-AC framework [*Bhattacharjee et al.*, 2010]. Other simulation experiments were carried out with the BN parameterization, utilizing three different IN spectra. Two additional simulations were considered, in which the contribution to N_c from contact freezing was neglected (LP-NoFrzc and BN-PDA08-NoFrzc). Sensitivity simulations to the width of the updraft velocity distribution, σ_w, were performed for the CNT IN spectra. All the simulations share the same lateral forcing fields, surface fluxes, and aerosol input, and they only differ in the treatment of ice formation.

The time-height distributions of the total cloud fraction, CF, exhibits the basic features observed during the TWP-ICE campaign (Fig. 25). In the first period of the intensive observation period (IOP), prior to 25 January 2006, the region was influenced by an active monsoon period characterized by considerable convective activity. From 26 January to 2 February, the monsoon was suppressed, and little convective activity was observed, but high clouds persisted through the period. In the final part of the IOP (3–13 February) the region was increasingly impacted by continental storms, reflected in a renewed increase in the convective activity.

The simulated cloud fields show some differences in the CF, particularly the simulation with the BN-PDA08, which shows higher frequency of high CF cells. Common to all the simulations with the BN scheme is an increase, compared to the LP-CTRL, in the CF for the mixed-phase regime, particularly in the convectively active periods, as shown for two of the simulations in Fig. 27. The resulting simulated q_i fields are shown in Fig. 26. Ice mixing ratios generally reach a maxima in the layer extending from the 0 °C to the −38 °C levels. The overall ice mixing ratios encountered in the LP-CTRL simulation are generally higher than for the BN cases, the difference being more pronounced for the mixed-phase regime.

The temperature dependence of $N_{\mathrm{c,nuc}}$ and the total ice crystal concentration N_c was calculated from the model output for each one of the simulations as a function of temperature (Fig. 28). Similarly, the dominant transition from heterogeneous dominated freezing at T_{hom} to homogeneous dominated freezing in the cirrus regime is demonstrated in Fig. 28, as well as the impact of the assumed dynamical forcing on this transition (Fig. 29). The impact of the nucleation scheme in the partitioning of condensate was investigated through the ice fraction, f_c, defined as

$$f_c = \frac{q_i}{q_i + q_l}. \tag{73}$$

Figure 30 shows the temperature dependence of the condensate partitioning, for the BN-PDA08, LP-CTRL, BN-PDA08-NoFrzc, and LP-NoFrzc. Attention was given to variables affecting the radiative properties of the ice clouds. The size of ice particles would be among the most directly affected variables with changes in crystal concentrations. The behavior of effective radius for ice particles as a function of temperature is shown in Fig. 31 for two of the simulations. Figure 32 shows a time series of IWP from different simulation experiments, together with IWP derived from satellite retrievals from the geostationary satellite MTSAT-1R, using the Visible Infrared Shortwave-Infrared Split-Window Technique (VISST), described in *Fridlind et al.* [2012].

8.5 Discussion of the results

Since the lateral forcing and surface fluxes were prescribed identically in all simulation experiments, any differences in the cloud fields can be attributed to the interaction of the ice nucleation scheme with the BF process and the cloud microphysical response that follows. Some such differences are encountered between the fields produced with LP and BN parameterization respectively. $N_{\mathrm{c,nuc}}$ calculated with the BN-PDA08 and BN-MY92 is systematically lower for the mixed-phase cloud regime, as compared to LP-CTRL. For the $BN-CNT$ simulation, crystal number concentrations show similar values than those in LP-CTRL. In the CNT spectrum, the IN efficiency of mineral dust is accounted for by assuming a high value for the "compatibility parameter", m, equal to the cosine of the IN-water contact angle *Pruppacher and Klett* [1997]. For dust it is assumed that $m = 0.96$. The contribution of soot to the IN population is much smaller, which is represented in CNT by setting $m = 0.76$.

The greatest difference in the number of nucleated ice crystals is found between LP-CTRL and BN-PDA08, for which the maximum difference in the predicted $N_{\mathrm{c,nuc}}$ can be considerable (Fig. 28). The low concentration of IN predicted by the PDA08 spectrum, typically two orders of magnitude lower than produced by the other spectra, explains part of this difference. However, the systematic discrepancy between LP and BN in the mixed-phase regime is likely due to the different implementation of the two nucleation schemes. As described in Sect. 8.3.1, the LP scheme adds the contributions from immersion freezing (given by the numerical correlations of *Liu and Penner* [2005]) and from deposition (as given by Eq. (70)). In the BN schemes the availability of IN in the mixed-phase regime is dictated by the IN spectrum alone, which consider deposition and condensation freezing.

The large differences in predicted $N_{\mathrm{c,nuc}}$ are also noticeable in the resulting N_c fields, but the magnitude of the difference is significantly lower. In the range of temperatures where contact freezing is active ($270.15\,\mathrm{K} > T > 235\,\mathrm{K}$) this mechanism was found to contribute, on average, between $10^{-4}\,\mathrm{cm}^{-3}$ and $10^{-3}\,\mathrm{cm}^{-3}$ to the ice crystal concentration, thereby effectively providing a lower bound for N_c (Fig. 28). This contribution is significant only for IN spectrum predicting very low $N_{\mathrm{c,nuc}}$ (such as PDA08), or for the temperatures above $T \sim 260\,\mathrm{K}$, in which the other IN spectrum (MY92 and CNT) predicts very small $N_{\mathrm{c,nuc}}$.

It is expected that the differences in N_c would significantly impact other cloud microphysical variables, particularly through the modification of the rate of the BF process. Lower ice crystal concentrations should result in lower rates of conversion of liquid water to ice because the surface area for vapor–ice mass transfer is low [*Rotstayn et al.*, 2000]. Such behavior, in which low aerosol concentrations are associated with low f_{c}, has been observed in satellite retrievals for the case of dust aerosol [*Choi et al.*, 2010]. However, the ice fraction exhibits little to no change across simulations even for the cases where N_c differ by a factor of 100 (Fig. 30a, b). This diminished sensitivity of f_c to ice crystal concentration seems to be caused by the action of the contact freezing mechanism. To verify this, two simulations in which this mechanism was deactivated were performed (LP-NoFrzc and BN-PDA08-NoFrzc), the results of which are shown in Fig. 30c, d. LP-NoFrzc shows that the transition from pure liquid to pure ice cloud occurs over a larger temperature interval as compared to simulations in which contact freezing is allowed to occur. However, because LP predicts relatively large crystal concentrations in the entire range of supercooling temperatures, the BF process is always fast, resulting in a rather similar dependence of f_c on temperature. This is not the case for the simulations with BN-PDA08, in which the low N_c severely limits the rate of conversion of liquid water to ice by water vapor deposition, which is evidenced when contact freezing is deactivated (Fig. 30d).

Satellite data based on polarization measurements and cloud top brightness temperatures retrieved during the monsoon active period of the TWP-ICE campaign, suggest that liquid-only cloud tops occur at temperatures above 253 K, while only ice-topped clouds are seen at temperatures colder than T_{hom} [*van Diedenhoven et al.*, 2012]. These observations, consistent with similar studies [e.g., *Choi et al.*, 2010], suggest that the simulated glaciation temperatures in our simulations could be too warm, pointing perhaps to an overestimation of the mass transfer to ice from contact freezing. Nevertheless, the narrow temperature range associated with the transition from $f_c = 0$ at 273 K to $f_c = 1$ at 260 K is consistent with other studies with the same partitioning scheme, as well as with available cloud observations of f_c [*Rotstayn et al.*, 2000; *Liu et al.*, 2007]. This transition to a fully glaciated state at warmer temperatures has been exhibited by cloud resolving models for the same observation period [*van Diedenhoven et al.*, 2012]. For the coarse vertical resolution of a GCM, this rapid glaciation could arise from the assumption that the BF mechanism dominates this regime [*Korolev*, 2007].

The cloud amount in the mixed-phase regime was affected by the crystal ice nucleation parameterization used in the simulations. As shown in Fig. 27, there is an increase in the frequency of occurrence of cloudy cells with $CF > 0.5$ when the BN-PDA08 parameterization is used in place of LP. This is true for the three IN spectra utilized in this study, with CF being 49 % larger for BN-PDA08, and $\sim$ 25% for BN-MY92 and BN-CNT, as compared to simulations with LP.

In the cirrus cloud regime, the difference in $N_{\mathrm{c,nuc}}$ between LP and BN is less pronounced than in the mixed-phase regime. For this temperature range, crystal concentrations calculated with LP and BN are within one order of magnitude irrespective of the IN spectrum used, which is consistent with the variability reported in previous studies [*Barahona et al.*, 2010b]. $N_{\mathrm{c,nuc}}$ for LP-CTRL and BN-PDA08 are in close agreement, however, the predicted mechanism of freezing is different for both parameterizations. Due to the very low IN number predicted with PDA08, the contribution of heterogeneous freezing to $N_{\mathrm{c,nuc}}$ in BN-PDA08 is negligible, and the process is dominated by homogeneous freezing (Fig. 28). The opposite behavior is observed when LP is used, in which homogeneous freezing only contributes significantly to the $N_{\mathrm{c,nuc}}$ at extremely low temperatures. When CNT or MY92 are used instead, the lower $N_{\mathrm{c,nuc}}$ is the result of the depletion of water vapor from the more numerous IN, and homogeneous freezing is triggered only at temperatures between 200 K and 220 K (Fig. 28).

The impact of updraft velocity on the dominant freezing mechanism is exemplified in Fig. 29. When a weak dynamical forcing is applied (e.g., $\sigma_w = 0.1\,\mathrm{m\,s^{-1}}$), freezing on the available IN rapidly depletes supersaturation, and the resulting dominant mechanism is heterogeneous freezing, implying that colder temperatures are required to enter the homogeneous freezing dominated regime. When the dynamical forcing is stronger (e.g., $\sigma_w = 0.5\,\mathrm{m\,s^{-1}}$), the available IN cannot deplete supersaturation quickly enough to prevent homogeneous freezing to occur, and the transition to homogeneous freezing occurs even at warmer temperatures. This behavior is shown in the envelope of Fig. 29. Such dependency on updraft velocity was not observed when the PDA08 was used (not shown), because IN concentrations are very low, such that even extremely weak updrafts ($\sim 0.05\,\mathrm{ms^{-1}}$) are enough for high supersaturations to be reached, thereby favoring homogeneous freezing as the dominant freezing mechanism [*Barahona and Nenes*, 2009b].

Finally, even though the impact of N_c on the simulated condensate partitioning is small, the different ice crystal concentration predicted with the parameterizations considered in this study considerably impact the cloud radiative properties. For instance, Figs. 26 and 27 shows the ice mixing ratio for different simulation scenarios. The differences observed translate also into ice water path differences, as well as of the hydrometeor sizes. Figure 31 shows the temperature dependence of the median values of the calculated ice effective radius for BN-PDA08 and LP-CTRL. The inset shows a histogram of the frequency distribution of the effective radius for BN-PDA08 and LP only for the range of mixed-phase temperatures. Due to the much lower N_c predicted by PDA08, the effective radius is shifted from a median of $45\,\mu$m for BN-PDA08, to a smaller size with a median of $32\,\mu$m in the LP-CTRL simulation.

The changes induced in the cloud microphysics by the different IN spectra consequently modify the overall column integrated properties of the cloud fields. Figure 32 illustrates the time series of IWP for the different parameterizations. It is clear that

IWP for LP-CTRL is higher than for any simulation with BN, with differences being larger in the periods of convective activity. In fact, the average IWP in the active monsoon period for the LP simulation was found to be $0.30\,\mathrm{kg\,m^{-2}}$, while it was of $0.23\,\mathrm{kg\,m^{-2}}$ for BN-PDA08, and $0.28\,\mathrm{kg\,m^{-2}}$ for BN-CNT and BN-MY92. In the suppressed period, IWP averaged $\sim 0.04\,\mathrm{kg\,m^{-2}}$ in all the simulation experiments. These results compare qualitatively well to the available data of IWP as retrieved from MTSAT data. However, the lower bound in these satellite retrievals tends to be much lower than the simulated IWP, while the peaks during the convective events often exhibit higher values than simulated fields. This marked underestimation of the lower IWP values is shown in the relative frequency histograms of Fig. 32. Ice water path from MTSAT during the active monsoon period averages $0.25\,\mathrm{kg\,m^{-2}}$ and $0.04\,\mathrm{kg\,m^{-2}}$ for the suppressed period.

8.6 Summary and conclusions

The ice nucleation parameterization of *Barahona and Nenes* [2009b] was implemented in the GEOS-5 McRAS-AC cloud scheme and tested in single column mode forced with TWP-ICE campaign data. Three different heterogeneous ice nucleation spectra (PDA08, CNT, and MY92) were used in simulations experiments with the BN parameterization framework. The IN concentration predicted by the spectra used in this study varied greatly, with PDA08 predicting very low IN concentrations of around $\sim 10^{-4}\,\mathrm{cm}^{-3}$, followed by the much higher IN concentrations predicted with MY92, generally $\sim$ 100 times larger than PDA08 at any given temperature. BN-CNT predicted the highest IN concentrations in the mixed-phase regime. These simulation experiments were compared to a control simulation using the LP parameterization, which was found to predict the highest ice crystal concentrations across the simulations.

It was shown that the different schemes used in this study often predicted IN concentrations differing by up to three orders of magnitude. Despite these important differences in IN availability, ice crystal number concentration for cirrus cloud temperatures predicted in all the simulations were found to agree within a factor of 10. However, the mechanism by which these ice crystal are produced is considerably different; N_c computed with LP was dominated by heterogeneous freezing, while simulations with BN transitioned from heterogeneous to homogeneous dominated freezing at higher temperatures. The dynamical forcing was also shown to be an important component in determining the transition from heterogeneous to homogeneous dominated freezing.

In the regime of mixed-phase clouds, the variations in N_c among simulations with the different nucleation schemes was considerably larger than for the ice-only clouds, with the largest variations being within a factor of $\sim$ 100. This larger variability is not surprising, since in the absence of homogeneous freezing, the nucleation schemes strongly depend on the IN nucleation spectra. However, the contribution to N_c from contact freezing of cloud droplets with dust particles of $\sim 10^{-3}\,\mathrm{cm}^{-3}$ provided a lower bound on N_c, and was effectively the largest contributor to crystal concentration when the PDA08 scheme was used. This contribution to N_c also acted to counteract the very large variations in predicted IN concentrations. This points out the specific need for more studies on the necessary parameters to describe contact freezing accurately.

Similarly, it was also found that the action of contact freezing efficiently transforming cloud water into cloud ice buffered the impact of the large variations of N_c seen across the different simulation experiments on the partitioning of cloud condensate. Ice mixing ratios, however, were strongly affected by the ice nucleation scheme. Accordingly, cloud microphysical variables relevant to radiative properties, such as the effective radius of ice crystals and the ice water path, were impacted by the wide range of N_c predicted. It was observed that nucleation schemes that predict lower N_c lead to lower in-cloud ice mixing ratios and ice water path, and considerably larger crystal sizes.

This study highlights the need for detailed cloud microphysical observations to constrain the large uncertainties associated with the ice nucleation process which limit the ability of GCM models to make accurate estimates of the contribution of cold clouds to the overall aerosol indirect effects. Continued development and refinement of ice nucleation schemes capable of accounting correctly for different freezing mechanisms is needed; using the approaches used here will help accomplish this.

8.7 Acknowledgements

We acknowledge the JCET/NASA Graduate Summer Research Program in Earth Sciences. A. Nenes acknowledges support from DOE grant DE-SC0007145 and NASA

ACMAP grant NNX08AK50G. D. Barahona was supported by the NASA MAP program under WBS 802678.02.17.01.07. Lee, Oreopoulos and Sud were supported by funding from NASA's IDS and MAP programs. Resources supporting this work were provided by the NASA High-End Computing (HEC) Program through the NASA Center for Climate Simulation (NCCS) at Goddard Space Flight Center. The authors also acknowledge the valuable insight from Trude Strovelmo and one anonymous reviewer.

Edited by: J. H. Seinfeld

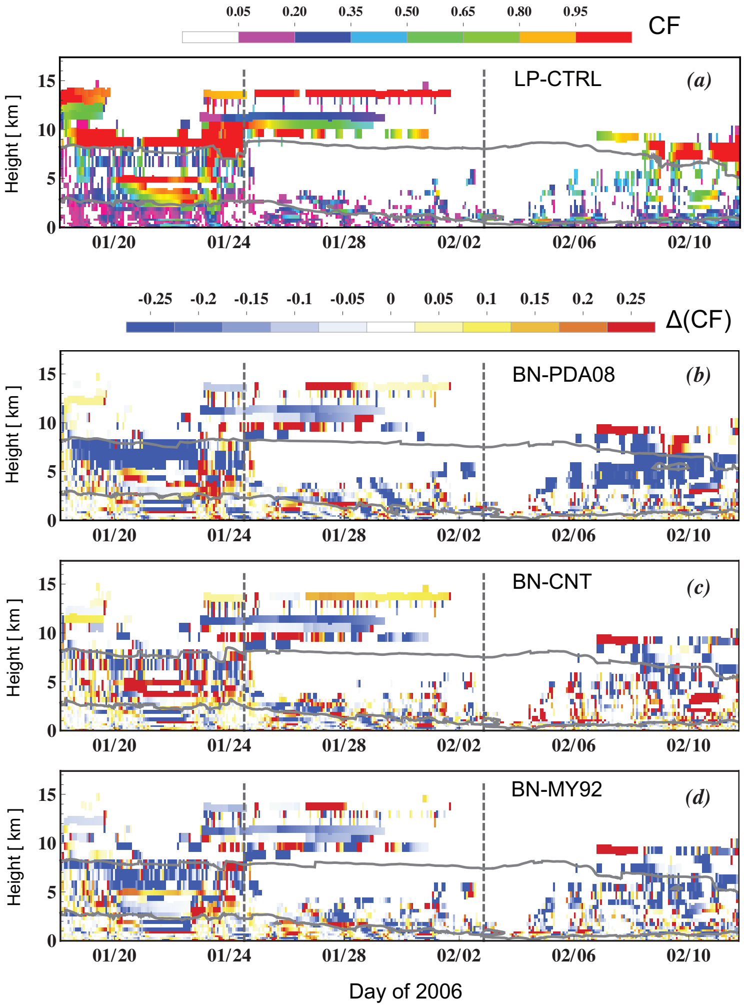

Figure 25: Time-Height distribution of the simulated cloud fraction for **(a)** Control simulation with the LP ice nucleation parameterization. **(b)**, **(c)**, and **(d)** are the differences in the distribution of cloud fraction between the LP-CTRL and simulations performed with BN: **(b)** for the PDA08 ice nucleation spectra, (c) for the CNT ice nucleation spectra, and **(d)** corresponds to the simulation with the MY92 ice nucleation spectra. The gray curves correspond to the 0 °C and −38 °C isolines, indicating the region where mixed-phase clouds may occur.

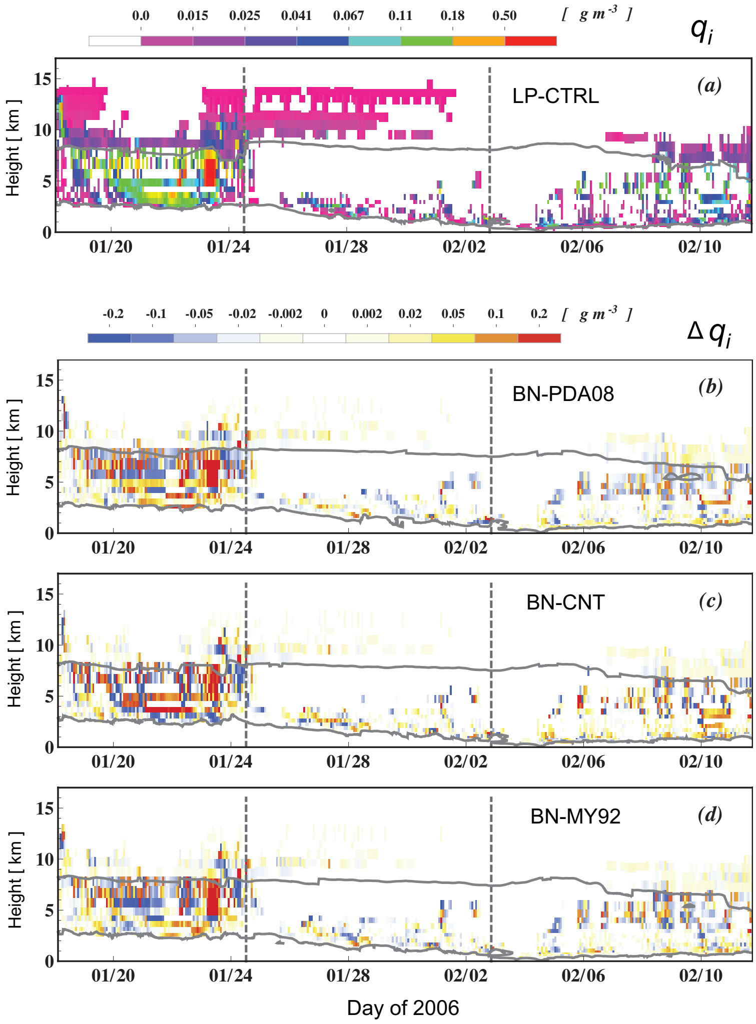

Figure 26: As in Fig. 25 but for ice mixing ratio in $\mathrm{g\,m^{-3}}$.

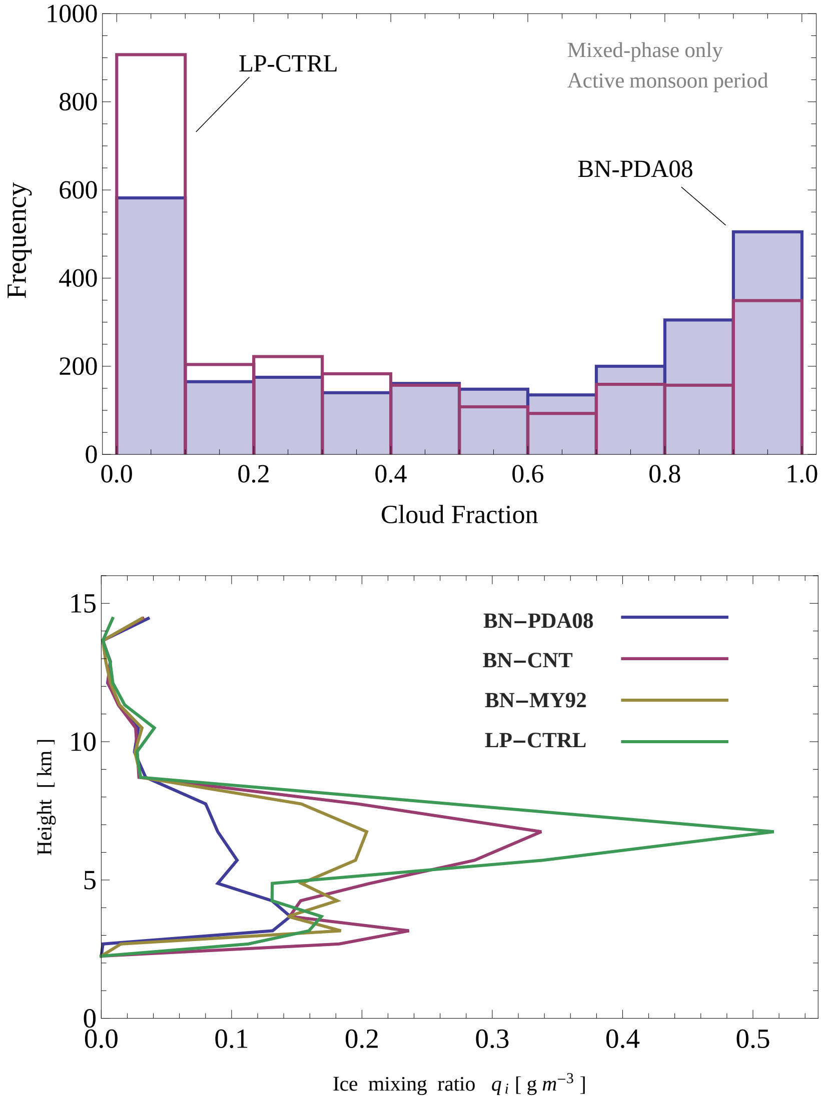

Figure 27: **(a)** Histogram of cloud fraction for the LP-CTRL and BN-PDA08 simulations. The frequencies are calculated for the active monsoon period and for cells with temperatures in the range $235\,\mathrm{K} < T < 273\,\mathrm{K}$. **(b)** Vertical profile of in-cloud ice mixing ratios averaged over the monsoon active period.

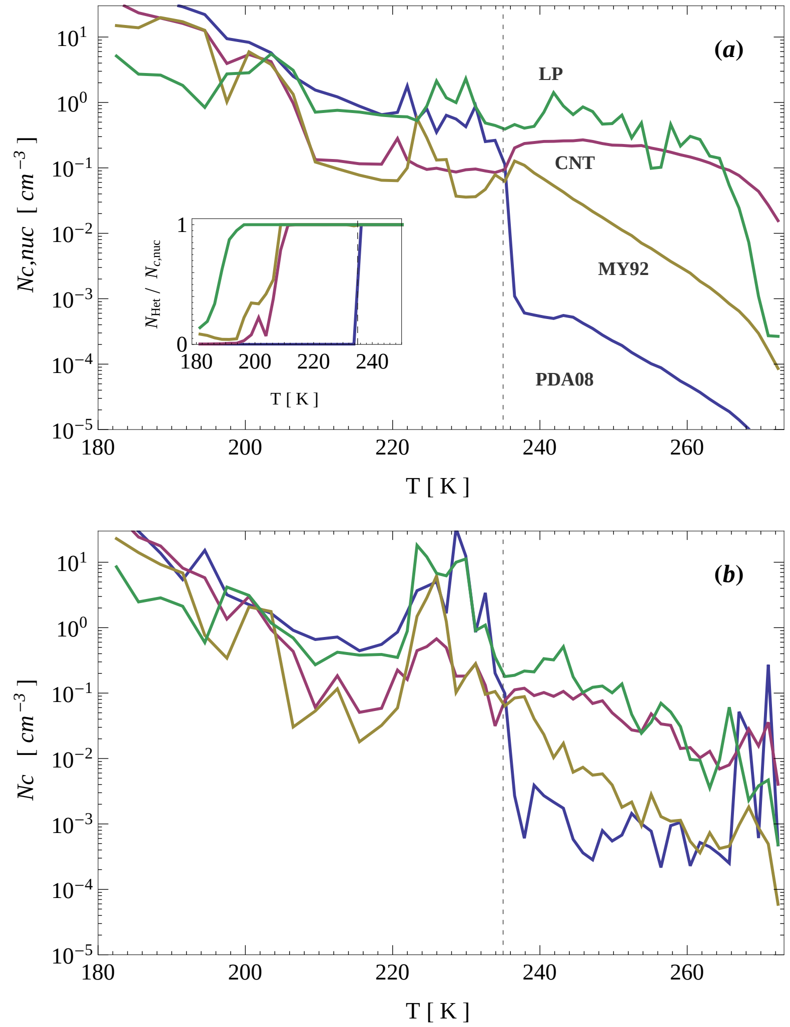

Figure 28: (a) Average number of nucleated ice crystals, $N_{\mathrm{c,nuc}}$ as a function of temperature for the simulations considered in this study. The inset is the fraction of crystals nucleated heterogeneously, $N_{\mathrm{het}}/N_{\mathrm{c,nuc}}$. (b) Average number concentration of ice crystals N_c as a function of temperature. The vertical dashed line marks the homogeneous freezing temperature threshold.

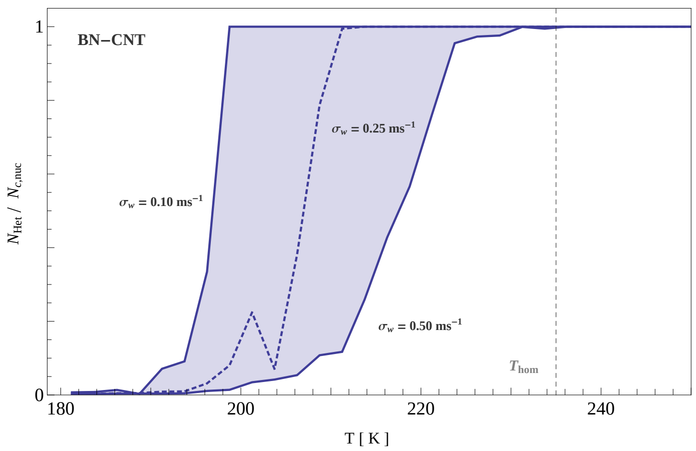

Figure 29: Average fraction of crystals nucleated heterogeneously, $N_{\mathrm{het}}/N_{\mathrm{c,nuc}}$ for the BN-CNT parameterization, as a function of temperature for different assumed widths of the probability distribution function of updrafts, σ_w, ranging from 0.1 to 0.5 ms^{-1}. The vertical dashed line marks the homogeneous freezing temperature threshold.

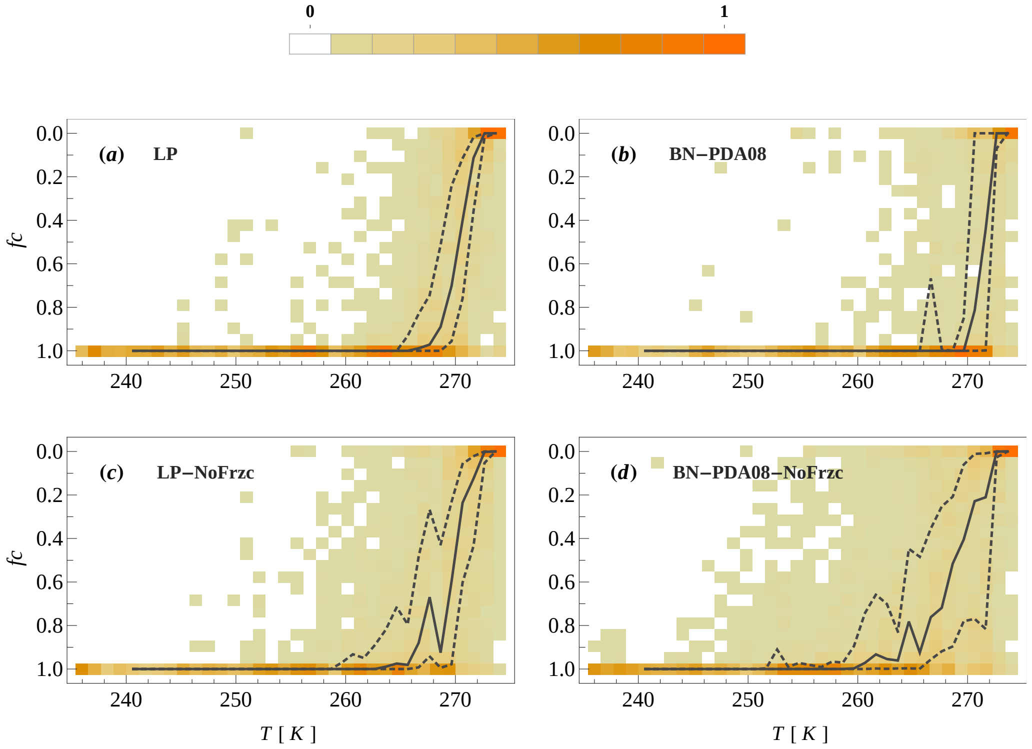

Figure 30: Frequency distribution of the ice fraction f_c as a function of temperature. The dark grey curves represent the quartiles of the distribution of f_c corresponding to a temperature interval of 1 K. **(a)** LP-CTRL simulation, **(b)** LP-NoFrzc simulation, **(c)** BN-PDA08 simulation, and **(d)** the BN-PDA08-NoFrzc.

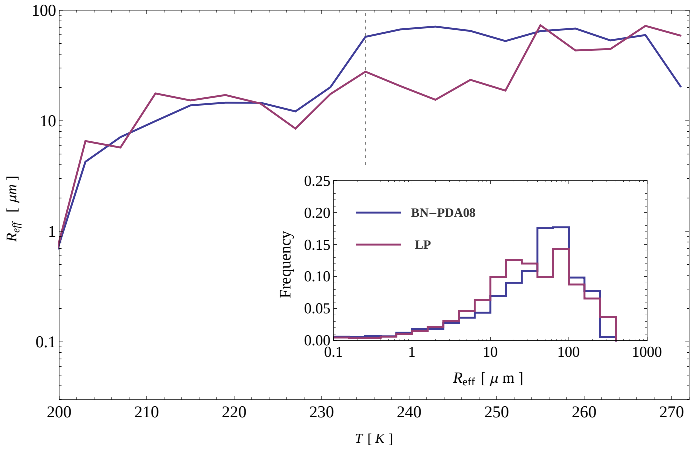

Figure 31: Median values for the ice crystals effective radius for BN-PDA08 and LP-CTRL. The inset is a histogram of the frequency distribution of the effective radius of ice crystals for the simulated clouds in the mixed-phase temperature regime (235K$< T <$ 273K). The bins are uniformly separated in logarithmic scale.

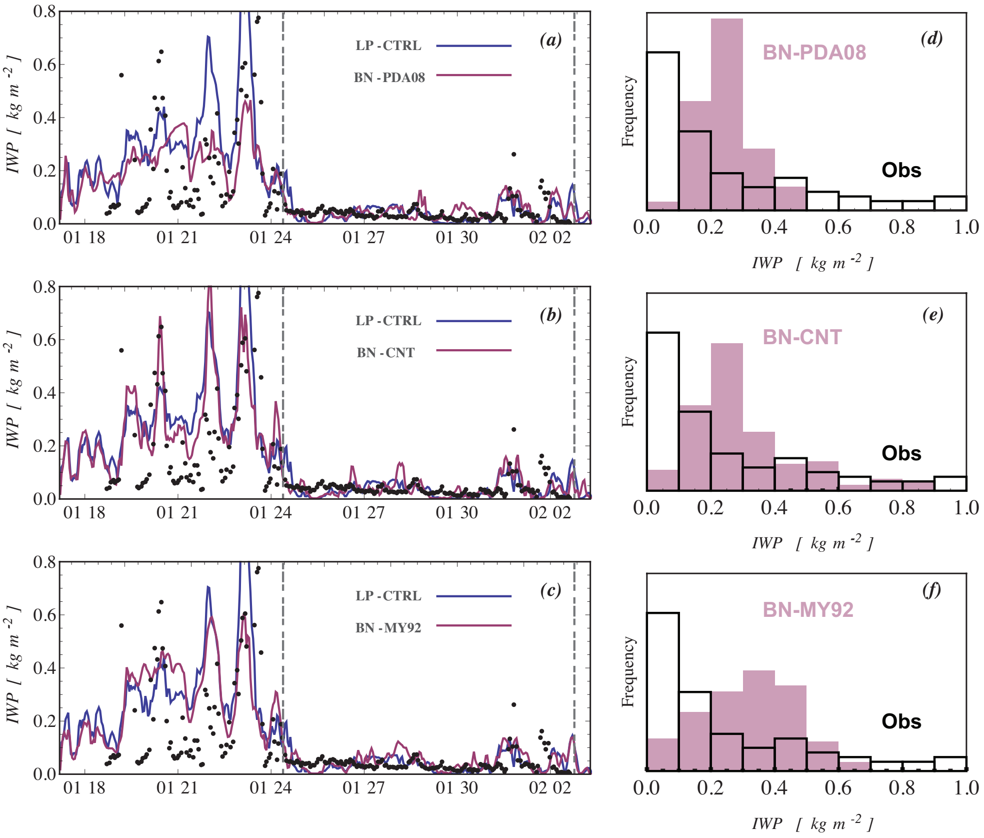

Figure 32: Ice Water Path (IWP) time series in kg m^{-2} from MTSAT-derived data with the VISST technique, and simulated IWP for different IN spectra **(a)** LP-CTRL and BN-PDA08, **(b)** LP-CTRL and BN-CNT, **(c)** LP-CTRL and BN-MY92. The dashed vertical lines denote the initiation and end of the suppressed monsoon period. **(d)**, **(e)**, and **(f)** are the corresponding relative frequency histograms for the time-series data restricted to the active monsoon period. Black (empty) histograms correspond to observations, while shaded histograms correspond to simulations with BN.

CHAPTER IX

CONCLUSIONS AND IMPLICATIONS

In this thesis, a variety of atmospheric models are used to better understand the representation of aerosol-cloud interactions in global circulation models (GCMs). With the increase in the complexity of aerosol modules and cloud microphysical schemes incorporated in current GCMs, new challenges arise regarding the physical consistency of the parameterizations used, and the links between resolved variables and the unresolved ones.

To address some of these questions, this thesis (1) postulates new methods to account for previously neglected subgrid variability effects in climate models, (2) implements new analysis techniques to identify specific variables and processes responsible for discrepancies across activation parameterizations, (3) develops a new formulation for activation parameterizations to describe the water uptake of the entire CCN population, and (4) utilizes in-situ observations to evaluate the validity and applicability of an existing activation parameterization that accounts for entrainment and mixing.

In Chapters 2 and 3 a new method to account for the subgrid variability of cloud droplet number on gridcell average process rates was investigated. The underlaying distribution of N_d is computed as a consequence of the subgrid scale variability diagnosed from the model turbulent kinetic energy. The different non-linear dependence of cloud microphysical processes and properties (e.g., autoconversion rate and cloud droplet effective radius) is shown to impact to a different extent each individual process rate. The magnitude of this impact is estimated with both, simple analytical arguments, and detailed calculations with the *Fountoukis and Nenes* [2005]. The theoretical basis of this subgrid scale variability (Chapter 4) are shown. In Chapter 3 the global impact of this formulation is then tested in the Community Atmosphere Model version 5.1, (CAM5.1), finding out that the enhancement in autoconversion rates has an important impact in the climatology of the model, producing 15% lower gloabal mean LWP and SWCF. Since this correction affects equally present-day and pre-industrial time simulations, its impact on aerosol indirect effects is small. In this way, processes that sometimes are required to be tunned independently of each other, can be treated in a more coupled way, imposing a reduction in the number of independent tunning parameters.

In Chapter 5, the adjoint-sensitivity of two commonly used aerosol activation parameterizations [*Fountoukis and Nenes*, 2005; *Abdul-Razzak and Ghan*, 2000] are implemented in the CAM5.1 GCM. The simulations clearly show the specific variables for which these parameterizations schemes have inconsistent responses, and the spatial distribution of these 'highly sensitive' variables was established. It was found that correct treatment of the water depletion by coarse mode particles has a crucial importance in modulating the maximum supersaturation in the parcel. Differences across the parameterization schemes considered showed that the different responses over marine and continental air mases is largely explained by the differing sensitivity to coarse mode aerosol particles. Similarly, it was found that the response to changes in aerosol mass alone (considering constant aerosol number) is 2-fold larger for the [*Abdul-Razzak and Ghan*, 2000] parameterization compared to the [*Fountoukis and Nenes*, 2005]. This discrepancy was found to be magnified in regions where aerosol mass increase has been dominated by condensible species rather than by primary emitted particles. The adjoint sensitivities are sued to estimate the contributions to droplet number changes coming from changes in either aerosol number concentration, mass concentration, or chemical composition. In order to evaluate the physical consistency of the response, extensive evaluation of the parameterization-derived sensitives was performed against detailed simulations of the activation process with a Lagrangian parcel model.

Overall, it was found that the two parameterizations considered here, *Abdul-Razzak and Ghan* [2000] and *Fountoukis and Nenes* [2005], produce similar aerosol indirect forcing estimates, suggesting that these physically-based schemes are not a major source of model uncertainty.

Chapter 6 describes and evaluates modifications to the formulation of the "population splitting" concept, fundamental in the development of the activation parameterization of *Nenes and Seinfeld* [2003] and *Barahona et al.* [2010a]. This formulation was shown to be capable of reproducing parcel model results more accurately and with less scatter.

In addition to the primary thesis work presented in Chapters 2-6, Chapter 7 presents a summary of the results from group wide collaborative effort spanning several years. My contribution to this work was to assess the global impact of the uncertainty in the mass accommodation coefficient α_c, by implementing a parameterization capable of accounting for this non-continuum effects in the CAM5.1 model. The observationally derived values encountered by other group members in a large number of field campaigns suggests that $1.0 > \alpha_c > 0.1$. The simulations with the CAM5 model show that this uncertainty range in α_c has only little impact on the simulated clouds in the GCM.

The results presented in this work contribute to the understanding of important issues encountered in the current representation of aerosol-cloud interactions in large scale models. Future directions of this research should focus on devising comprehensive evaluation methods to measure the impact of the modifications here proposed with available observational data. Concurrent satellite retrievals LWP, N_d, and effective radius can be utilized in such evaluation. If properly coupled with the full physics of a GCM column, the adjoint approach could be used to further improve the satellite retrievals of below-cloud aerosols and cloud droplet numbers.

APPENDIX A

THE LAGRANGIAN MODEL OF THE CLOUD FORMATION PROCESS

The 1-Dimensional cloud parcel model is among the simplest frameworks used to describe the process of cloud formation and evolution. In this framework, the state of a Lagrangian element of moist air is described by solving the mass an energy conservation equations for the system. Despite its simplicity, this type of model reproduces the most general features of the cloud formation process, and allows for a detailed description of the activation and subsequent growth by condensation of a population of droplets. Limitations of this approach include that any interaction of this fluid element with the surroundings (including the process of entrainment and mixing) has to be prescribed and assumed homogeneous. The latter stipulation is rooted in the fact that the Lagrangian element has no spatial extent so its properties are, by definition, homogeneous. However, the cloud parcel model has been a valuable tool in the development of aerosol activation parameterizations. The next pages contain a brief compilation of the one dimensional parcel model formulation as presented in *Pruppacher and Klett* [1997] and *Houze* [1994].

A.1 Mass and energy conservation equations

The state of a Lagrangian element of moist air is described here by its temperature T, pressure p, and the mixing ratios of water vapor and liquid water, q_v and q_l respectively. The total water mixing ratio in the parcel, q_t, is entirely given by the contributions from vapor and liquid water, i.e., $q_t = q_v + q_l$. We assume that the moist air in the parcel is an ideal gas, and that the atmospheric column is in hydrostatic equilibrium.

The general conservation equation for any intensive variable in the parcel, $\mathcal{A}$ (expressed as per unit mass of air), includes the contribution from sources and sinks within the parcel, as well as changes due to the transport of this property across parcel boundaries, i.e., due to entrainment and mixing. However, because of the one dimensional nature of the model, the amount of air exchanged with the surroundings has to be prescribed. We describe the rate at which the mixing process occurs by fixing an *entrainment rate*, μ, defined as the fractional entrained mass per unit meter of ascent, i.e.,

$$\mu \equiv \frac{1}{m}\frac{dm}{dz} \tag{74}$$

With this definition, the conservation equation for any intensive scalar variable in the parcel rising at a vertical speed w takes the form,

$$\frac{d\mathcal{A}}{dt} = \left(\frac{d\mathcal{A}}{dt}\right)_s + \mu w(\mathcal{A}' - \mathcal{A}) \tag{75}$$

where the first term is the source term of $\mathcal{A}$ that would be present even in the absence of mixing, while the second term represents the dilution of the quantity $\mathcal{A}$ due to entrainment of environmental air with a concentration equal to $\mathcal{A}'$.

To determine the rate equations dictating the temporal evolution of the parcel variables we apply equation (75) to the specific enthalpy of the parcel as well as to q_v and q_l. These equations are complemented with the ideal gas law,

$$\rho_a = pM_a/RT \tag{76}$$

and the Clausius-Clapeyron equation,

$$\frac{de_s}{dT} = \frac{e_s M_w L_v}{RT^2} \tag{77}$$

Application of equation (75) to the mixing ratios of vapor and liquid water provides the evolution equations for these variables. In this case, the only internal source/sink of vapor or liquid is the process of condensation or evaporation (denoted with a subscript 'c'). Since the environmental air is subsaturated, we will neglect any amount of condensed water, i.e., $q_l' = 0$. With this stipulation, the conservation equations for the different categories of water are

$$\frac{dq_v}{dt} = \left(\frac{dq_v}{dt}\right)_c + \mu w (q_v' - q_v) \tag{78a}$$

$$\frac{dq_l}{dt} = \left(\frac{dq_l}{dt}\right)_c - \mu w \, q_l, \tag{78b}$$

Furthermore, since liquid water and water vapor are transformed into each other by the process of condensation and evaporation, the sources of q_v and q_l associated with phase changes satisfy the relation

$$\left(\frac{dq_v}{dt}\right)_c = -\left(\frac{dq_l}{dt}\right)_c \tag{79}$$

this relation is valid as long as vapor and liquid are the only water categories present in the parcel. Equations (78) and (79) dictate the rate equation for total water,

$$\frac{dq_t}{dt} = \mu w (q_v' - q_v - q_l) \tag{80}$$

The change in the enthalpy content of the parcel (which for an ideal gas is proportional to the temperature change) is given by the contributions from adiabatic expansion, the heat released by condensation or evaporation of water, and the temperature decrease from the mixing, i.e.,

$$-\frac{dT}{dt} = \frac{gw}{c_p} + \frac{L_v}{c_p}\left(\frac{dq_v}{dt}\right)_c + \mu w(T - T') \tag{81}$$

The rate equation for the parcel pressure can be found by assuming hydrostatic balance and that the air behaves as an ideal gas. Doing this we get

$$\frac{dp}{dt} = -\frac{gM_a w}{RT}p \tag{82}$$

The set of equations (78)-(82) is not a closed system of equations, and it is still necessary to formulate an expression describing the condensation/evaporation term $(dq_l/dt)_c$ in order to close the system.

A.1.1 The supersaturation tendency equation

Before discussing the different alternatives to close this set of equations, we introduce here a new variable, the *supersaturation*, s, commonly used to describe the concentration of water vapor in the parcel. It is defined such that $(s + 1)$ is equal to the saturation ratio, e/e_s, i.e., $s \equiv e/e_s$. In terms of p, q_v, and T, it is given by

$$s = \frac{M_a}{M_w}\frac{p\,q_v}{e_s(T)} - 1 \tag{83}$$

When s is positive (negative) the parcel is said to be supersaturated (subsaturated). Saturation with respect to water is attained for $s = 0$. Introduction of this variable will prove useful in the description of the condensational growth of cloud droplets. The evolution equation for s can be found by straightforward differentiation of (83), and use of equations (77) and (82),

$$\frac{ds}{dt} = \frac{M_a p}{M_w e_s}\frac{dq_v}{dt} - (s+1)\left[\frac{gM_a w}{RT} + \frac{M_w L_v}{RT^2}\frac{dT}{dt}\right] \tag{84}$$

The governing equations can be written explicitly in terms of the parcel variables, the environmental air properties, and the condensation sink/source. Replacing equations (78), (79), and (81) into (84) gives,

$$\frac{ds}{dt} = (s+1)w\left(\frac{gL_vM_w}{c_pRT^2} - \frac{gM_a}{RT}\right) - \left(\frac{L_v^2M_w}{c_pRT^2} + (s+1)\frac{M_ap}{M_we_s}\right)\left(\frac{dq_l}{dt}\right)_c - \mu w(s+1)\left(\frac{q_v - q_v'}{q_v} - \frac{L_vM_w}{RT^2}(T-T')\right) \quad (85)$$

The first term, proportional to w, describes the increase of the supersaturation due to cooling associated with adiabatic expansion. The second term, proportional to the condensation rate, $(dq_l/dt)_c$, represents the water vapor depletion and the temperature increase associated to water phase changes (both effects leading to a decrease in the supersaturation tendency). The last term, proportional to μw, includes the impact of entrainment on s, i.e., a decrease in the supersaturation through dilution of the water vapor mixing ratio, and an increase in the supersaturation through the enhanced cooling from mixing. It can be shown that the dilution effect is always greater than the enhanced cooling effect. Equation (85) does not involve any approximation besides the neglect of liquid water in the environmental air.

A.1.2 Bulk description of condensation

The 'bulk' approach to the condensation problem is one alternative used to close the system of equations (78) – (82). In this scheme, it is assumed that the phase changes within the parcel are solely dictated by bulk thermodynamic equilibrium. More specifically, it is assumed that no condensation occurs before the parcel reaches saturation. After saturation is attained, any vapor in excess of saturation condenses and the water vapor in the parcel remains saturated, i.e., $q_v = q_{_{vs}}(T)$. By this method, we can calculate the vertical profiles of pressure, temperature and mixing ratios of water. However because it does not explicitly describe the process of condensation, the bulk approach does not provide information on the microphysics of the cloud droplets, or about the activation of aerosols into cloud droplets.

The assumption that $q_v = q_{vs}$ implies that the parcel supersaturation is identically zero, and remains like that at any time after saturation. Therefore, s and its first derivative, ds/dt, would be identically zero after saturation. This allows to recover a closed expression for the condensation term $(dq_l/dt)_c$ from (85). Defining the following quantities,

$$\alpha = \frac{gL_vM_w}{c_pRT^2} - \frac{gM_a}{RT} \tag{86a}$$

$$\gamma = \frac{L_v^2M_w}{c_pRT^2} + \frac{M_ap}{M_we_s(T)}, \tag{86b}$$

and setting $ds/dt = s = 0$ in (85) we get,

$$\left(\frac{dq_l}{dt}\right)_c = \frac{\alpha w}{\gamma}\left[1 - \frac{\mu}{\alpha}\left(\frac{q_{vs} - q_v'}{q_{vs}} - \frac{L_vM_w}{RT^2}(T - T')\right)\right] \tag{87}$$

This expression for the condensation term closes the system of equations in the 'Bulk' description of condensation. Equation (87) also helps in understanding the physical meaning of each of the terms in the left hand side (LHS) of this equation. Setting $\mu = 0$ in equation (87) shows that the adiabatic rate of condensation per unit meter, denoted $\Gamma_{l,ad}$, is simply given by (α/γ) (e.g., *Curry and Webster* [1999]). Similarly, it becomes clear that the role of the entrainment term in equation (87) is to reduce net the condensation rate. Defining the "critical entrainment rate" μ_c, as the value for entrainment rate such that there is no more net condensation in the parcel. Setting $(dq_l/dt)_c = 0$ and solving for μ we get,

$$\mu_c = \alpha\left(\frac{q_{vs} - q_v'}{q_{vs}} - \frac{L_vM_w}{RT^2}(T - T')\right)^{-1} \tag{88}$$

or expressed in terms of the relative humidity, RH, of the entrained air,

$$\mu_c = \frac{\alpha}{(1 - RH)\left(1 - \frac{L_vM_w}{RT^2}\Delta T\right)} \tag{89}$$

where this expression was found by noting noting that $q'_v/q_{vs} = RH(e_s(T')/e_s(T))$, and using the Clausius-Clapeyron equation (77), to compute the ratio between saturation vapor pressures. With these definitions, the condensation rate in the "bulk" approach can be written as

$$\left(\frac{dq_l}{dt}\right)_c = \frac{\alpha w}{\gamma}\left[1 - \frac{\mu}{\mu_c}\right] \tag{90}$$

Although adiabatic parcel model simulations (i.e., with no entrainment) qualitatively capture the basic physical features and characteristics of a forming convective cloud, they considerably overestimate the liquid water content as well as the temperature difference between the cloudy and the surrounding air when compared to observations. Both of this deficiencies arise in the neglect of mass exchange between the parcel and its surroundings.

A.1.3 Mechanistic description of condensation

The "bulk" description above relies on the assumption that after saturation, the water vapor in the air parcel remains saturated allowing for a closed description of the ascending parcel thermodynamic state. In actuality however, when cloud droplets are formed, condensation does not occurs instantaneously, but its limited by the mass transfer of water vapor to the population of growing droplets. A more realistic approach to the description of cloud formation must consider the mass transfer of water vapor between the moist air and a population of water droplets. In such approach, liquid water can be present even before saturation occurs (in the form of deliquesced aerosol particles), and the condensation into the particles is explicitly considered, therefore removing the constrain that the air should remain saturated (i.e., q_v is no longer forced to be q_{vs}), and a supersaturated gas phase is allowed to occur (for which equation (85) is particularly suited). For this type of approach, we consider the liquid water mixing ratio as the total mass contained in a given population of water droplets. If we discretize the droplet population in n_b size categories, with N_i droplets of diameter D_{pi} in the ith-category, q_l is given by,

$$q_l = \frac{\rho_w}{\rho_a}\frac{\pi}{6}\sum_i N_i D_{pi}^3 \tag{91}$$

The condensation sink/source can be expressed in terms of the growth rate of the droplets by straightforward differentiation of equation (91),

$$\left(\frac{dq_l}{dt}\right)_c = \frac{\pi}{2}\frac{\rho_w}{\rho_a}\sum_i N_i D_{pi}^2 \frac{dD_{pi}}{dt} \tag{92}$$

The explicit growth rate for the droplet can be obtained. First, by considering the steady-state diffusion equation for a spherically symmetric droplet, and by assuming that the concentration at the surface of the droplet is equal to the saturation vapor pressure. This expression can be shown to be (e.g., *Pruppacher and Klett* [1997]; *Seinfeld and Pandis* [2006]),

$$\frac{dD_{pi}}{dt} = \frac{G}{D_{pi}}(s - s_{eq}) \tag{93}$$

where s_{eq} is the equilibrium saturation vapor pressure, and G is the mass transfer coefficient for the condensation process. This expression has the advantage that it can represent both condensation and evaporation. If G is known, and we can describe the equilibrium supersaturation of the droplet, the growth rate equation (93) closes the system of equations, and allow us to express the condensation rate. If $s > s_{eq}$ the driving force for condensation will be positive, but when $s < s_{eq}$ the driving force is negative and the droplets will evaporate. The mass transfer coefficient G is given by,

$$G = 4\left(\frac{\rho_w RT}{e_s D_v' M_w} + \frac{L_v \rho_w}{k_a' T}\left(\frac{L_v M_w}{RT} - 1\right)\right)^{-1} \tag{94}$$

this coefficient accounts for the effects of mass transfer and for the heat released during the condensation process. In equation (94), D_v' and k_a' are the water vapor diffusivity and thermal conductivity of air respectively, both modified to account for non-continuum effects [*Fukuta and Walter*, 1970]. These are given by,

$$D_v' = D_v \left(1 + \frac{2D_v}{\alpha_c D_p}\left(\frac{2\pi M_w}{RT}\right)^{1/2}\right)^{-1} \tag{95}$$

and,

$$k_a' = k_a \left(1 + \frac{2k_a/\rho_a c_p}{\alpha_T D_p}\left(\frac{2\pi M_w}{RT}\right)^{1/2}\right)^{-1} \tag{96}$$

where α_c is the mass accommodation coefficient, and α_T is the thermal accommodation coefficient. The equilibrium supersaturation is given by the Köler equation [*Köhler*, 1936], i.e.,

$$s_{eq} = \frac{A}{D_p} - \kappa\frac{d_p^3}{D_p^3} \tag{97}$$

where A is related to the surface tension of water σ_w by $A = 4M_w\sigma_w/TR\rho_w$, and κ is the hygroscopicity parameter. The evolution of each droplet size, can be found by replacing equation (97) and (94), in the droplet growth equation. With this, is then possible to compute, mechanistically, the evolution of the liquid water in the parcel, namely

$$\left(\frac{dq_l}{dt}\right)_c = \frac{\pi}{2}\frac{\rho_w}{\rho_a}\sum_i^{n_b} n(D_p, d_p)G(D_p)D_p\left[s - s_{eq}(D_p, d_p)\right] \tag{98}$$

Equation (98), together with the n_b equations (93) closes the system of equations for the mechanistic description of condensation.

A.2 Application to Activation Parameterizations

Since the purpose of activation parameterizations is to determine the maximum supersaturation achieved in the parcel, equation (85) is considered only at the point of maximum supersaturation. For most atmospherically relevant conditions, supersaturation in liquid clouds rarely reach values higher than 1%, the approximation

$(s+1) \approx s$ introduces only minimal error. Using this approximation, the supersaturation tendency equation (85) reduces to,

$$\frac{ds}{dt} = \alpha w - \gamma \left(\frac{dq_l}{dt} \right)_c - \alpha w \frac{\mu}{\mu_c} \tag{99}$$

with α, γ, and μ_c as defined by equation (86a), (86b), and (89). An equation for the maximum supersaturation, s_{max} can be found by setting $ds/dt = 0$ in equation (99). The expression obtained is,

$$\left(\frac{dq_l}{dt} \right)_{c,s_{max}} = \frac{\alpha w}{\gamma} \left(1 - \frac{\mu}{\mu_c} \right) \tag{100}$$

In this expression, the left hand side is determined by the thermodynamic properties of the parcel and by the entrainment rate, and is assumed to be known. Furthermore, because of the approximation $(s+1) \approx 1$, the condensation rate in Equation (100) corresponds to the "bulk" condesnation given by Equation (90). Therefore, Equation (100) indicates that the condensation onto the growing droplets at the time of s_{max} is fixed by thermodynamic conditions, for instance, in the adiabatic case where $\mu = 0$, it will be equal to $\alpha w/\gamma$. However, the maximum supersaturation will depend on the details of the mass transfer of the water vapor to the droplet population, which is given by the left hand side of Equation (100). When applied to activation parameterization, $(dq_l/dt)_c$ must be expressed in terms of the droplet population. This is achieved by using Equations (92) and a simplified version of Equation (93) in which $s_{eq} = 0$ (neglecting solute and curvature effects), and the mass transfer coefficient G is considered to be size independent. Furthermore, parameterizations that account for non-continuum effects neglect the impact of thermal accommodation coefficient (i.e., using k_a instead of k'_a), and lump all the non continuum effect impacts on the accommodation coefficient α_c alone. With these simplifications applied to Equation (98), Equation (100) reads,

$$\frac{\pi}{2}\frac{\rho_w}{\rho_a}Gs_{max}\int n(D_p,t_{max})D_p\mathrm{d}D_p=\frac{\alpha w}{\gamma}\left(1-\frac{\mu}{\mu_c}\right) \tag{101}$$

or equivalently,

$$s_{max}\int n(D_p,t_{max})D_p\mathrm{d}D_p=\frac{2\rho_a\alpha w}{\pi\rho_w\gamma G}\left(1-\frac{\mu}{\mu_c}\right)\equiv\beta\left(1-\frac{\mu}{\mu_c}\right) \tag{102}$$

Other quantities commonly defined during the development of activation parameterizations [*Twomey*, 1959; *Abdul-Razzak and Ghan*, 2000] are,

$$\eta=\frac{4\rho_a}{\pi\gamma\rho_w}\left(\frac{\alpha w}{G}\right)^{3/2} \qquad \text{and} \qquad \zeta=\frac{2A}{3}\left(\frac{\alpha w}{G}\right)^{1/2} \tag{103}$$

in terms of these expression, $\beta=(3\eta/\zeta A)$.

A.2.1 Entrainment in activation parameterizations: Relation to Earlier Studies

The treatment of entrainment here is closely related to previous studies of the condensation problem. However, earlier parameterization of the entrainment process in a 1D model had only an incomplete treatment of the impacts of entrainment. For instance, the droplet activation parameterization of *Feingold and Heymsfield* [1992] proposed the to account for entrainment by adding (incorrectly) a term $E=\frac{1}{q_{vs}}\frac{dq_t}{dt}$ to the supersaturation equation. Their expression for E does not account for the temperature effects, but rather only by the dilution of total water in the parcel. Their formulation can be made consistent with Equation (99) if the entrainment term E is set equal to $E=-\alpha w(\mu/\mu_c)$. Similarly, *Brenguier* [1991], proposed a simple, integrable expression to account for the dilution due to continuous entrainment, but did not specify the impact of entrainment and mixing on the condensation rate as done in *Barahona et al.* [2010a], and expressed in equations (90) and (100).

APPENDIX B

CLOUD MICROPHYSICAL VARIABLES AS GENERALIZED GAMMA VARIATES

B.1 The generalized gamma distribution

Let X be a random variable whose frequency distribution is

$$f(x;\alpha,\beta,\gamma)=\frac{\gamma}{\beta\Gamma(\alpha)}\left(\frac{x}{\beta}\right)^{\alpha\gamma-1}e^{-\left(\frac{x}{\beta}\right)^{\gamma}} \tag{104}$$

for non-negative values of x, and positive values of the parameters α, β and γ. The variable X is said to follow a generalized gamma distribution [*Stacy*, 1962], denoted as $X\sim\Gamma(\alpha,\beta,\gamma)$. The r-th moment of the random variate X is,

$$E(X^r)=\frac{\beta^r\Gamma\left(\alpha+r/\gamma\right)}{\Gamma\left(\alpha\right)} \tag{105}$$

It can be shown that if X is a random variable with the corresponding p.d.f given by (104), then the variable $y=ax^b$ (with $a>0$ and $b>0$) is also a generalized gamma variate, such that $y\sim\Gamma(\alpha;a\beta^b,\gamma/\beta)$, this is,

$$f_Y(y)=f(y;\,\alpha,a\beta^b,\gamma/b) \tag{106}$$

The number of cloud droplets per unit volume of air, n, as well as the mass of liquid water per unit volume of air, q, are important parameters defining the microphysical state of a cloud. The variability of this quantities at scales unresolved by climate models are represented by assuming such variations follow certain probability distributions. For instance, in a forming cloud, n is a strong function of the updraft velocity of the cloudy element, w, which dictates the rate of cooling driving the condensation process. A good approximation for the dependence of n on w is a power law relation,

$$n(w) = \begin{cases} aw^b & x > 0 \\ 0 & x \leq 0 \end{cases} \tag{107}$$

with a and b positive constants. The velocity w is assumed to follow a normal distribution with zero mean, and a standard deviation given by some appropriate velocity scale, σ_w, i.e., $w \sim N(0, \sigma_w)$. The relation (107) then implies a probability distribution for n. Noticing that the support of n is $w > 0$ it can be shown that n is a generalized gamma variate [*Malik*, 1967], with parameters,

$$n \sim \Gamma\big(\frac{1}{2}, a(2\sigma_w)^{b/2}, \frac{2}{b}\big) \tag{108}$$

On the other hand, q is often found to follow a gamma distribution, characterized by its mean $\hat{q}$ and the inverse relative variance ν_q, i.e., is also a generalized gamma variate with parameters

$$q \sim \Gamma\big(\nu_q, \frac{\hat{q}}{\nu_q}, 1\big) \tag{109}$$

Of interest for climate modeling and satellite retrievals of cloud properties are certain functions of n and q of the form $y = q^{c_1}/n^{c_2}$ (such as droplet effective radius and autconversion rates), with c_1 and c_2 positive numbers. Since q and n are generalized gamma variates, its positive powers are also generalized gamma variates, and the problem of finding the distribution of y is reduced to finding the distribution of the ratio of two independent generalized gamma variates $A = Q/N$, with $Q \equiv q^{c_1}$ and $N \equiv n^{c_2}$, following the corresponding distribution, i.e.,

$$\begin{aligned} Q &\sim \Gamma\big(\,\nu_q,\,(\hat{q}/\nu_q)^{c_1},\frac{1}{c_1}\,\big) \\ N &\sim \Gamma\big(\,\frac{1}{2},\,\beta_n^{c_2},\frac{2}{bc_2}\big) \end{aligned} \tag{110}$$

where $\beta_n \equiv a(2\sigma_w)^{b/2}$. The r-th moment of the random variable A can be easily found by applying Equation (105),

$$E(A^r) = E(QN^{-1}) = E(q^{c_1})E(n^{-c_2}) \tag{111}$$

However, the expression for the p.d.f. of A cannot be found through the usual method used to obtain the expression of the p.d.f. of a ratio of two random variates from their joint distribution, since the integral that needs to be solved does not have an explicit solution. Nevertheless, applications that require only knowledge of the moments of such distribution can use Equation (111). Also, the distribution of A can be drawn from the ratio of variables generated with the distribution Q and N.

B.1.1 Numerical Examples

The effective radius of a cloud droplet population R_e (the ratio of the third and second moments of the droplet size distribution) depends on n and q with exponents $c_1 = c_2 = 1/3$. Similarly, the mass conversion rate of cloud water into precipitation, denoted A, also exhibit similar behavior, with exponents $c_1 = 2.47$ and $c_2 = 1.79$. Figure 33 shows the corresponding distribution for R_e and A for parameters values typical of stratocumulus clouds.

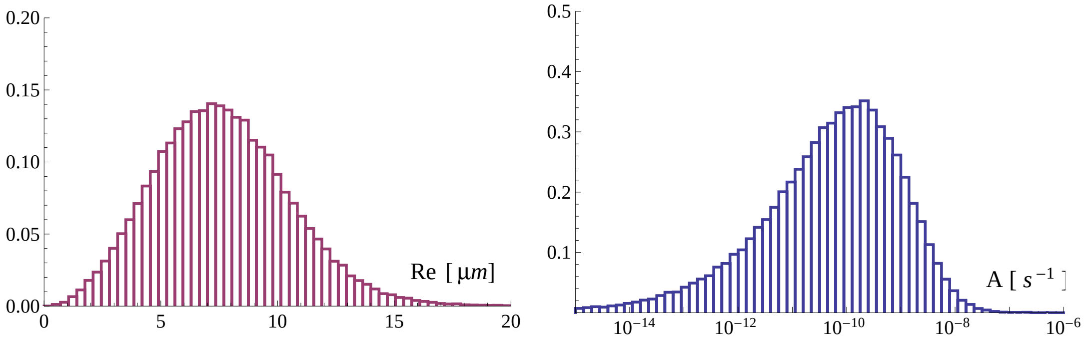

Figure 33: Probability distribution function for effective radius R_e (in μm) and Autoconversion rate (in units of inverse seconds) for the following parameters: $a = 240$, $b = 0.30$, $\sigma_w = 0.26\ \mathrm{ms}^{-1}$, $\hat{q} = 0.2\ \mathrm{gm}^{-3}$, $\nu_q = 1.05$.

REFERENCES

Abdul-Razzak, H., and S. Ghan (2000), A parameterization of aerosol activation: 2. Multiple aerosol types, *J. Geophys. Res.*, *105*, 6837–6844.

Abdul-Razzak, H., S. Ghan, and C. Rivera-Carpio (1998), A parameterization of aerosol activation: 1. Single aerosol type, *J. Geophys. Res.*, *103*, 6123–6131.

Adams, P. J., and J. H. Seinfeld (2003), Disproportionate impact of particulate emissions on global cloud condensation nuclei concentrations, *Geophys. Res. Lett.*, *30*(5), 1239, doi:10.1029/2002GL016303.

Albrecht, B. (1989), Aerosols, cloud microphysics, and fractional cloudines, *Science*, *245*, 1227–1230.

Anderson, B. E., W. B. Grant, G. . L. Gregory, E. V. Browell, J. E. Collins, G. W. Sachse, D. R. Bagwell, H. C.H., D. R. Blake, and N. J. Blake (1996), Aerososl from biomass burning over the tropical South Atlantic region: Distributions and impacts, *J. Geophys. Res.*, *101*(D19), 24,117–24,137.

Arabas, S., H. Pawloska, and W. Grabowski (2009), Effective radius and droplet spectral width from in-situ aircraft observations in trade-wind cumuli during RICO, *Geophys. Res. Lett.*, *36*, L11,803, doi:10.1029/2009GL038257.

Asa-Awuku, A., and A. Nenes (2007), Effect of solute dissolution kinetics on cloud droplet formation: Extended Köhler theory, *J. Geophys. Res.*, *112*, doi:10.1029/2005JD006934.

Baker, H. W. (1996), A Parameterization for Computing grid-averaged solar fluxes for inhomogeneous marine boundary layer clouds. Part I: Methodology and homogeneous biases, *J. Atmos. Sci.*, *53*(16), 2289–2303.

Baker, M., R. Corbin, and J. Latham (1980), The influence of entrainment on the evolution of cloud droplet spectra: I. A model of inhomogeneous mixing, *Q. J. R. Meteorol. Soc.*, *106*, 581–598.

Barahona, D. (2012), On the ice nucleation spectrum, *Atmos. Chem. Phys.*, *12*, 3733–3752, doi:10.5194/acp-12-3733-2012.

Barahona, D., and A. Nenes (2007), Parameterization of cloud droplet formation in large-scale models: Including effects of entrainment, *J. Geophys. Res.*, *112*, D16,206, doi:10.1029/2007JD008473.

Barahona, D., and A. Nenes (2008), Parameterization of cirrus cloud formation in large-scale models: Homogeneous nucleation, *J. Geophys. Res.*, *113*, D11211, doi:10.1029/2007JD009355.

BARAHONA, D., and A. NENES (2009a), Parameterizing the competition between homogeneous and heterogeneous freezing in cirrus cloud formation: monodisperse ice nuclei, *Atmos. Chem. Phys.*, *9*, 1–13.

BARAHONA, D., and A. NENES (2009b), Parameterizing the competition between homogeneous and heterogeneous freezing in cirrus cloud formation: polydisperse ice nuclei, *Atmos. Chem. Phys.*, *9*, 5933–5948.

BARAHONA, D., R. WEST, P. STIER, S. ROMAKKANIEMI, H. HOKKOLA, and A. NENES (2010a), Comprehensively accounting for the effect of giant CCN in cloud activation parameterizations, *Atmos. Chem. Phys.*, *10*, 2467–2473.

BARAHONA, D., J. RODRIGUEZ, and A. NENES (2010b), Sensitivity of the global distribution of cirrus ice crystal concentration to heterogeneous freezing, *J. Geophys. Res.*, *115*, D23213, doi:10.1029/2010JD014273.

BARAHONA, D., R. SOTIROPOULOU, and A. NENES (2011), Global distribution of cloud droplet number concentration, autoconversion rate and aerosol indirect effect under diabatic droplet activation, *J. Geophys. Res.*, *116*, D09,203, doi: 10.1029/2010JD015274.

BAUER, S. E., and S. MENON (2012), Aerosol direct, indirect, semidirect, and surface albedo effects from sector contributions based on the IPCC AR5 emissions for preindustrial and present-day conditions, *J. Geophys. Res.*, *117*, D01206, doi: 10.1029/2011JD016816.

BHATTACHARJEE, P. S., Y. C. SUD, X. LIU, G. K. WALKER, R. YANG, and J. WANG (2010), Importance of including ammonium sulfate ($(NH_4)_2SO_4$) aerosols for ice cloud parameterization in GCMs, *Ann. Geophys.*, *28*, 621–631.

BOUCHER, O., and U. LOHMANN (1995), The sulfate-ccn-cloud albedo effect, *Tellus*, *47B*, 281–300.

BOUGIATIOTI, A., C. FOUNTOUKIS, N. KALIVITIS, S. N. PANDIS, A. NENES, and N. MIHALOPOULOS (2009), Cloud condensation nuclei measurements in the marine boundary layer of the eastern mediterranean: Ccn closure and droplet growth kinetics, *Atmos. Chem. Phys.*, *9*(18), 7053–7066.

BOUGIATIOTI, A., A. NENES, C. FOUNTOUKIS, N. KALIVITIS, S. N. PANDIS, and N. MIHALOPOULOS (2011), Size-resolved CCN distributions and activation kinetics of aged continental and marine aerosol, *Atmos. Chem. Phys.*, *11*(16), 8791–8808.

BRENGUIER, J. L. (1991), Parameterization of the condensation process: A theoretical approach, *J. Atmos. Sci.*, *48*, 264–282.

BURNET, F., and J.-L. BRENGUIER (2006), Observational study of the entrainment-mixing process in warm convective clouds, *J. Atmos. Sci.*, *64*, 1995–2011, doi: 10.1175/JAS3928.1.

Cerully, K. M., T. Raatikainen, S. Lance, D. Tkacik, P. Tiitta, T. Petäjä, M. Ehn, M. Kulmala, D. R. Worsnop, A. Laaksonen, J. N. Smith, and A. Nenes (2011), Aerosol hygroscopicity and CCN activation kinetics in a boreal forest environment during the 2007 EUCAARI campaign, *Atmos. Chem. Phys.*, *11*(23), 12,369–12,386.

Charlson, R. J., S. E. Schwartz, J. Hales, R. D. Cess, J. A. Coakley, J. E. Hansen, and D. J. Hofmann (1992), Climate forcing by anthropogenic aerosols, *Science*, *255*(5043), 423–430, doi:10.1175/JAS3975.1.

Chen, W.-T., A. Nenes, H. Liao, P. J. Adams, J.-L. F. Li, and J. H. Seinfeld (), Global climate response to anthropogenic aerosol indirect effects: Present day and year 2100, *J. Geophys. Res.*, *115*(D12).

Cheng, A., and K. M. Xue (2009), A PDF-based microphysics parameterization for simulation of drizzling boundary layer clouds, *J. Atmos. Sci.*, *66*, 2317–2334, doi:101175/2009JAS2944.1.

Choi, Y.-S., R. S. Lindzen, C.-H. Ho, and J. Kim (2010), Space observations of cold-cloud phase change, *Proc. Nat. Acad. Sci.*, *107*(25), 11,211–11,216, doi: 10.1073/pnas.1006241107.

Chosson, F., J.-L. Brenguier, and L. Schüller (2006), Entrainment-mixing and radiative transfer simulation in boundary layer clouds, *J. Atmos. Sci.*, *64*, 2670–2682, doi:10.1175/JAS3975.1.

Chuang, P. Y. (), Measurement of the timescale of hygroscopic growth for atmospheric aerosols, *J. Geophys. Res.*, *108*(D9).

Chuang, P. Y., R. J. Charlson, and J. H. Seinfeld (1997), Kinetic limitations on droplet formation in clouds, *Nature*, *390*, 594–596.

Conant, W. C., T. M. VanReken, T. A. Rissman, V. Varutbangkul, H. H. Jonsson, A. Nenes, J. L. Jimenez, A. E. Delia, R. Bahreini, G. Roberts, R. Flagan, and J. H. Seinfeld (2004), Aerosol-cloud drop concentration closure in warm clouds, *J. Geophys. Res.*, *109*, D13,204, doi:10.1029/2003JD004324.

Connolly, P. J., O. Mohler, P. R. Field, H. Saathoff, R. Burgess, T. Choularton, and M. Gallagher (2009), Studies of heterogeneous freezing by three different desert dust samples, *Atmos. Chem. Phys.*, *9*, 2805–2824.

Curry, J. A. (1985), Interactions among turbulence, radiation and microphysics in arctic stratus clouds, *J. Atmos. Sci.*, *43*, 90–106.

Curry, J. A., and V. I. Khvorostyanov (2012), Assessment of some parameterizations of heterogeneous ice nucleation in cloud and climate models, *Atmos. Chem. Phys.*, *12*, 1151–1172, doi:10.5194/acp-12-1151-2012.

Curry, J. A., and P. J. Webster (1999), *Thermodynamics of Atmospheres and Oceans*, International Geophysics (Book 65), Academic Press.

D'Almeida, G. A. (1987), On the variability of desert aerosol radiative characteristics, *J. Geophys. Res.*, *92*, 3017–3026.

de Rooy, W. C., and P. Siebesma (1985), Analytical expressions for entrainment and detrainment in cumulus convection, *Q. J. R. Meteorol. Soc.*, *136*, 1216–1227, doi:10.1002/qj.640.

DelGenio, A., M. Yao, K. W., and K. Lo (1996), A prognostic cloud water parameterization for global climate models, *J. Climate*, *9*, 270–304.

Dentener, F., S. Kinne, T. Bond, O. Boucher, J. Cofala, S. Generoso, P. Ginoux, S. Gong, J. J. Hoelzemann, A. Ito, L. Marelli, J. E. Penner, J.-P. Putaud, C. Textor, M. Schulz, G. R. van der Werf, and J. Wilson (2006), Emissions of primary aerosol and precursor gases in the years 2000 and 1750 prescribed data-sets for AeroCom, *Atmos. Chem. Phys.*, *6*(12), 4321–4344.

Dentener, F., S. Kinne, T. Bond, O. Boucher, J. Cofala, S. Generoso, P. Ginoux, S. Gong, J. J. Hoelzemann, A. Ito, L. Marelli, J. E. Penner, J.-P. Putaud, C. Textor, M. Schulz, G. R. van der Werf, and J. Wilson (2011), The dynamical core, physical parameterizations, and basic simulation characteristics of the atmospheric component AM3 of the GFDL Global Coupled Model CM3, *J. Climate*, *24*(12), 3484–3519.

Feingold, G., and P. Y. Chuang (2002), Analysis of the influence of film-forming compounds on droplet growth: Implications for cloud microphysical processes and climate, *J. Aerosol Sci.*, *59*, doi:10.1175/1520-0469(2002)05.

Feingold, G., and A. Heymsfield (1992), Parameterizations of condensational growth of droplets for use in general circulation models, *J. Atmos. Sci.*, *49*, 2325–2342.

Fountoukis, C., and A. Nenes (2005), Continued development of a cloud droplet formation parameterization for global climate models, *J. Geophys. Res.*, *110*, D11212, doi:10.1029/2004JD005591.

Fountoukis, C., A. Nenes, N. Meskhidze, R. Bahreini, W. C. Conant, H. Jonsson, S. Murphy, A. Sorooshian, V. Varutbangkul, F. Brechtel, R. C. Flagan, and J. H. Seinfeld (2007), Aerosol – cloud drop concentration closure for clouds sampled during the International Consortium for Atmospheric Research on Transport and Transformation 2004 campaign, *J. Geophys. Res.*, *112*, D10S30, doi:10.1029/2006JD007272.

Fridlind, A. M., A. S. Ackerman, J.-P. Chaboureau, J. Fan, W. W. Grabowski, A. A. Hill, T. R. Jones, M. M. Khaiyer, G. Liu, P. Minnis,

H. Morrison, L. Nguyen, S. Park, J. C. Petch, J.-P. Pinty, C. Schumacher, B. J. Shipway, A. C. Varble, X. Wu, S. Xie, and M. Zhang (2012), A comparison of TWP-ICE observational data with cloud-resolving model results, *J. Geophys. Res.*, *117*, D05,204, doi:10.1029/2011JD016595.

Fukuta, N., and N. A. Walter (1970), Kinetics of hydrometeor growth from a vapor-spherical model, *J. Atmos. Sci.*, *27*, 1160–1172.

Gettelman, A., H. Morrison, C. R. Terai, and R. Wood (2013), Microphysical process rates and global aerosol-cloud interactions, *Atmos. Chem. Phys. Discuss.*, *13*(5), 11,789–11,825.

Ghan, S., C. Chuang, and J. Penner (1993), A parameterization of cloud droplet nucleation. Part I: Single aerosol type, *Atmos. Res.*, *30*, 198–221, doi:10.1016/0169-8095(93)90024-I.

Ghan, S., G. Guzman, and H. Abdul-Razzak (1998), Competition between sea salt and sulfate particles as cloud condensation nuclei, *J. Atmos. Sci.*, *55*, 3340–3347.

Ghan, S., H. Abdul-Razzak, A. Nenes, Y. Ming, X. Liu, M. Ovchinnikov, N. Meskhidze, J. Xu, and X. Shi (2011), Droplet nucleation: physically-based parameterization and comparative evaluation, *J. Adv. Model. Earth. Syst.*, *3*, D10S30, doi:10.1029/2011MS000074.

Ghan, S. J., X. Liu, R. C. Easter, R. Zaveri, P. J. Rasch, and J.-H. Yoon (2012), Toward a minimal representation of aerosols in climate models: Comparative decomposition of aerosol direct, semidirect, and indirect radiative forcing, *J. Climate*, *25*, 6461–6476, doi:10.1175/JCLI-D-11-00650.1.

Golaz, J.-C., V. E. Larson, and W. R. Cotton (2002), A PDF-based model for boundary layer clouds. Part I: Method and model description, *J. Atmos. Sci.*, *59*, 3540–3551, doi:10.1029/2011MS000074.

Guo, H., Y. Lin, P. H. Daum, G. I. Senum, and W.-K. Tao (2008), Characteristics of vertical velocity in marine stratocumulus: comparison of LES with observations, *J. Atmos. Sci.*, *3*, 045,020.

Hoose, C., and O. Möhler (2012), Heterogenous ice nucleation on atmospheric aerosols: a review of results from laboratory experiments, *Atmos. Chem. Phys. Discuss.*, *12*, 12,531–12,621, doi:10.5194/acpd-12-12531-2012.

Hoose, C., J. E. Kristjánsson, J.-P. Chen, and A. Hazra (2010), A classical-theory-based parameterization of heterogeneous ice nucleation by mineral dust, soot, and biological particles in a global climate model, *J. Atmos. Sci.*, *67*, 2483–2503, doi:10.1175/2010JAS3425.1.

Houze, R. (1994), *Cloud dynamics*, International geophysics series, Academic Press.

Hsieh, W., H. Jonsson, L.-P. Wang, G. Buzorius, R. Flagan, J. Seinfeld, and A. Nenes (2009a), On the representation of droplet coalescence and autoconversion: Evaluation using ambient cloud droplet size distributions, *J. Geophys. Res.*, *114*, D07,201, doi:10.1029/2008JD010502.

Hsieh, W., A. Nenes, R. Flagan, J. Seinfeld, G. Buzorius, and H. Jonsson (2009b), Parameterization of cloud droplet size distributions: comparison with parcel models and observations, *J. Geophys. Res.*, *114*, D11,205, doi: 10.1029/2008JD011387.

Intergovernmental Panel on Climate Change, . (2007), *Fourth Assessment Report: Climate Change 2007: Working Group I Report: The Physical Science Basis*, Geneva: IPCC.

Jensen, E. J., and O. B. Toon (1994), Ice nucleation in the upper troposphere: Sensitivity to aerosol number density, temperature, and cooling rate, *Geophys. Res. Lett.*, *21*, 2019–2022.

Jiang, H., H. Xue, G. Teller, A. Feingold, and Z. Levin (2006), Aerosol effects on the lifetime of shallow cumulus, *Geophys. Res. Lett.*, *33*(L14806), doi: 10.1029/2006GL026024.

Jimenez, J. L., M. R. Canagaratna, N. M. Donahue, A. S. H. Prevot, Q. Zhang, J. H. Kroll, P. F. DeCarlo, J. D. Allan, C. H., N. L. Ng, A. C. Aiken, K. S. Docherty, I. M. Ulbrich, A. P. Grieshop, A. L. Robinson, J. Duplissy, J. D. Smith, K. R. Wilson, V. A. Lanz, C. Hueglin, Y. L. Sun, J. Tian, A. Laaksonen, T. Raatikainen, J. Rautiainen, P. Vaattovaara, M. Ehn, M. Kulmala, J. M. Tomlinson, D. R. Collins, M. J. Cubison, E. J. Dunlea, J. A. Huffman, T. B. Onasch, M. R. Alfarra, P. I. Williams, K. Bower, Y. Kondo, J. Schneider, F. Drewnick, Borrmann, S. Weimer, K. Demerjian, D. Salcedo, L. Cottrell, R. Griffin, A. Takami, T. Miyoshi, S. Hatakeyama, A. Shimono, J. Y. Sun, Y. M. Zhang, K. Dzepina, J. R. Kimmel, D. Sueper, J. T. Jayne, S. C. Herndon, A. M. Trimborn, L. R. Williams, E. C. Wood, A. M. Middlebrook, C. E. Kolb, U. Baltensperger, and W. D. R. (2009), Evolution of organic aerosols in the atmosphere, *Science*, *326*(5959), 1525–1529.

Kärcher, B., and U. Lohmann (2002), A parameterization of cirrus cloud formation: Homogeneous freezing of supercooled aerosols, *J. Geophys. Res.*, *107*(D2), 4010, doi:10.1029/2001JD000470.

Kärcher, B., and U. Lohmann (2003), A parameterization of cirrus cloud formation: Heterogeneous freezing, *J. Geophys. Res.*, *108*(D14), 4402, doi: 10.1029/2002JD003220.

Kärcher, B., and J. Ström (2003), The roles of dynamical variability and aerosols in cirrus cloud formation, *Atmos. Chem. Phys.*, *3*, 823–838.

Karydis, V. A., S. L. Capps, R. H. Moore, A. G. Russell, D. K. Henze, and A. Nenes (2012a), Using a global aerosol model adjoint to unravel the footprint of spatially-distributed emissions on cloud droplet number and cloud albedo, *Geophys. Res. Lett.*, *39*(19), 9041–9055.

Karydis, V. A., S. L. Capps, A. G. Russell, and A. Nenes (2012b), Adjoint sensitivity of global cloud droplet number to aerosol and dynamical parameters, *Atmos. Chem. Phys.*, *12*(19), 9041–9055.

Khairoutdinov, M., and Y. Kogan (2000), A new cloud physics parameterization in a large-eddy simulation model of marine stratocumulus, *Monthly Weather Rev.*, *128*, 229–243.

Khvorostyanov, V. I., and J. A. Curry (2009), Critical humidities of homogeneous and heterogeneous ice nucleation: Inferences from extended classical nucleation theory, *J. Geophys. Res.*, *114*, D04207, doi:10.1029/2008JD011197.

Kim, B.-G., M. A. Miller, S. E. Schwartz, Y. Liu, and Q. Min (2008), The role of adiabaticity in the aerosol first indirect effect, *J. Geophys. Res.*, *113*, D05,210, doi:10.1029/2007JD008961.

Kinne, S., M. Schulz, C. Textor, S. Guibert, Y. Balkanski, S. E. Bauer, T. Berntsen, T. F. Berglen, O. Boucher, M. Chin, W. Collins, F. Dentener, T. Diehl, R. Easter, J. Feichter, D. Fillmore, S. Ghan, P. Ginoux, S. Gong, A. Grini, J. Hendricks, M. Herzog, L. Horowitz, I. Isaksen, T. Iversen, A. Kirkevåg, S. Kloster, D. Koch, J. E. Kristjansson, M. Krol, A. Lauer, J. F. Lamarque, G. Lesins, X. Liu, U. Lohmann, V. Montanaro, G. Myhre, J. Penner, G. Pitari, S. Reddy, O. Seland, P. Stier, T. Takemura, and X. Tie (2006), An AeroCom initial assessment – optical properties in aerosol component modules of global models, *Atmos. Chem. Phys.*, *6*(7), 1815–1834.

Kogan, Y. L. (2005), Large-eddy simulations of air parcels in stratocumulus clouds: Time scales and spatial variability, *J. Atmos. Sci.*, *63*, 952–967.

Köhler, H. (1936), The nucleus in and the growth of hygroscopic droplets, *Trans. Farad. Soc.*, *32*, 1152.

Kolb, C. E., R. A. Cox, J. P. D. Abbatt, M. Ammann, E. J. Davis, D. J. Donaldson, B. C. Garrett, C. George, P. T. Griffiths, D. R. Hanson, M. Kulmala, G. McFiggans, U. Pöschl, I. Riipinen, M. J. Rossi, Y. Rudich, P. E. Wagner, P. M. Winkler, D. R. Worsnop, and C. D. O' Dowd (2010), An overview of current issues in the uptake of atmospheric trace gases by aerosols and clouds, *Atmos. Chem. Phys.*, *10*(21), 10,561–10,605.

Koren, I., and G. Feingold (2011), Aerosol-cloud-precipitation system as a predator-prey problem, *Proc. Nat. Acad. Sci.*, doi:10.1073/pnas.1101777108.

Koren, I., Y. J. Kaufman, D. Rosenfeld, L. A. Remer, and Y. Rudich (), Aerosol invigoration and restructuring of atlantic convective clouds, *Geophys. Res. Lett.*, *32*(14).

Korolev, A. (2007), Limitations of the Wegener – Bergeron – Findeisen mechanism in the evolution of mixed-phase clouds, *J. Atmos. Sci.*, *64*, 3372–3375, doi: 10.1175/JAS4035.1.

Krueger, S., C.-W. Su, and P. McMurtry (1997), Modeling entrainment and finescale mixing in cumulus clouds, *J. Atmos. Sci.*, *54*, 2697–2712.

Kumar, P., I. N. Sokolik, and A. Nenes (2009), Parameterization of cloud droplet formation for global and regional models: including adsorption activation from insoluble CCN, *Atmos. Chem. Phys.*, *9*, 2517–2532.

Lamarque, J.-F., T. C. Bond, V. Eyring, C. Granier, A. Heil, Z. Klimont, D. Lee, C. Liousse, A. Mieville, B. Owen, M. G. Schultz, D. Shindell, S. J. Smith, E. Stehfest, J. Van Aardenne, O. R. Cooper, M. Kainuma, N. Mahowald, J. R. McConnell, V. Naik, K. Riahi, and D. P. van Vuuren (2010), Historical (1850-2000) gridded anthropogenic and biomass burning emissions of reactive gases and aerosols: methodology and application, *Atmos. Chem. Phys.*, *10*(15), 7017–7039.

Lance, S., A. Nenes, C. Mazzoleni, M. K. Dubey, H. Gates, V. Varutbangkul, T. A. Rissman, S. M. Murphy, A. Sorooshian, R. C. Flagan, J. H. Seinfeld, G. Feingold, and H. H. Jonsson (2009), Cloud condensation nuclei activity, closure, and droplet growth kinetics of houston aerosol during the gulf of mexico atmospheric composition and climate study (gomaccs), *J. Geophys. Res.*, *114*(D7).

Lance, S., T. Raatikainen, T. B. Onasch, D. R. Worsnop, X.-Y. Yu, M. L. Alexander, M. R. Stolzenburg, P. H. McMurry, J. N. Smith, and A. Nenes (2013), Aerosol mixing state, hygroscopic growth and cloud activation efficiency during mirage 2006, *Atmos. Chem. Phys.*, *13*(9), 5049–5062.

Larson, V. E., R. Wood, P. R. Field, J.-C. Golaz, T. H. Vonder Haar, and W. R. Cotton H. (2000), Systematic biases in the microphysics and thermodynamics of numerical models that ignore subgrid-scale variability, *J. Atmos. Sci.*, *58*, 1117–1128.

Lasher-Trapp, S., W. Cooper, and A. Blyth (2005), Broadening of droplet size distributions from entrainment and mixing in a cumulus cloud, *Q. J. R. Meteorol. Soc.*, *131*, 195–220, doi:10.1256/qj.03.199.

Latham, J., and R. Reed (1977), Laboratory studies of the effects of mixing on the evolution of cloud droplet spectra, *Q. J. R. Meteorol. Soc.*, *103*, 297–306.

Lathem, T. L., and A. Nenes (2011), Water vapor depletion in the DMT continuous-flow ccn chamber: Effects on supersaturation and droplet growth, *Aerosol Sci. Tech.*, *45*(5), 604–615.

Lathem, T. L., A. J. Beyersdorf, K. L. Thornhill, E. L. Winstead, M. J. Cubison, A. Hecobian, J. L. Jimenez, R. J. Weber, B. E. Anderson, and A. Nenes (2013), Analysis of CCN activity of Arctic aerosol and canadian biomass burning during summer 2008, *Atmos. Chem. Phys.*, *13*(5), 2735–2756.

Leaitch, W., C. M. Banic, G. A. Isaac, M. D. Couture, P. S. K. Lius, I. Gultepe, S. Li, L. Kleinman, P. Daum, and M. J.I. (1996), Physical and chemical observations in marine stratus during the 1993 north atlantic regional experiment: Factors controlling cloud droplet number concentrations, *J. Geophys. Res.*, *101*, 29,123–29,135.

Lee, L. A., K. S. Carslaw, K. J. Pringle, G. W. Mann, and D. V. Spracklen (2011), Emulation of a complex global aerosol model to quantify sensitivity to uncertain parameters, *Atmos. Chem. Phys.*, *11*(23), 12,253–12,273.

Lee, L. A., K. S. Carslaw, K. J. Pringle, and G. W. Mann (2012a), Mapping the uncertainty in global CCN using emulation, *Atmos. Chem. Phys.*, *12*(20), 9739–9751.

Lee, L. A., K. J. Pringle, C. L. Reddington, G. W. Mann, P. Stier, D. V. Spracklen, J. R. Pierce, and K. S. Carslaw (2013), The magnitude and causes of uncertainty in global model simulations of cloud condensation nuclei, *Atmos. Chem. Phys. Discuss.*, *13*(3), 6295–6378.

Lee, S. S., and L. J. Donner (2011), Effects of cloud parameterization on radiation and precipitation: A comparison between single-moment microphysics and double-moment microphysics, *Terr. Atmos. Ocean. Sci.*, *22*(4), 403–420, doi: 10.3319/TAO.2011.03.03.01(A).

Lee, Y. H., J.-F. Lamarque, M. G. Flanner, C. Jiao, D. T. Shindell, T. Berntsen, M. M. Bisiaux, J. Cao, W. J. Collins, M. Curran, R. Edwards, G. Faluvegi, S. Ghan, L. W. Horowitz, J. R. McConnell, G. Myhre, T. Nagashima, V. Naik, S. T. Rumbold, R. B. Skeie, K. Sudo, T. Takemura, and F. Thevenon (2012b), Evaluation of preindustrial to present-day black carbon and its albedo forcing from ACCMIP (Atmospheric Chemistry and Climate Model Intercomparison Project), *Atmos. Chem. Phys. Discuss.*, *12*(8), 21,713–21,778.

Lehmann, K., H. Siebert, and R. Shaw (2009), Homogeneous and inhomogeneous mixing in cumulus clouds: dependence on local turbulence structure, *J. Atmos. Sci.*, *66*, 3641–3659, doi:10.1175/2009JAS3012.1.

Li, Z., F. Niu, J. Fan, Y. Liu, D. Rosendfeld, and Y. Ding (2011), Long-term impacts of aerosols on the vertical development of clouds and precipitation, *Nature Geoscience*, *4*, 888–894, doi:10.1038/ngeo1313.

Lin, R.-F., D. O. Starr, P. J. DeMott, R. Cotton, K. Sassen, E. Jensen, B. Kärcher, and X. Liu (2002), Cirrus parcel model comparison project. Phase 1: The critical components to simulate cirrus initiation explicitly, *J. Atmos. Sci.*, *59*(15), 3641–3659, doi:2305–2338.

Liu, X., and J. E. Penner (2005), Ice nucleation parameterization for global models, *Meteo. Z.*, *14*(4), 499–514.

Liu, X., and J. Wang (2010), How important is organic aerosol hygroscopicity to aerosol indirect forcing?, *Environ. Res. Lett.*, *5*(4), doi:10.1088/1748-9326/5/4/044010.

Liu, X., J. E. Penner, S. J. Ghan, and M. Wang (2007), Inclusion of ice microphysics in the NCAR Community Atmospheric Model Version 3 (CAM3), *J. Climate*, *20*, 4526–4547, doi:10.1175/JCLI4264.1.

Liu, X., R. C. Easter, S. J. Ghan, R. Zaveri, P. Rasch, X. Shi, J.-F. Lamarque, A. Gettelman, H. Morrison, F. Vitt, A. Conley, S. Park, R. Neale, C. Hannay, A. M. L. Ekman, P. Hess, N. Mahowald, W. Collins, M. J. Iacono, C. S. Bretherton, M. G. Flanner, and D. Mitchell (2012), Toward a minimal representation of aerosols in climate models: Description and evaluation in the community atmosphere model CAM5, *Geosci. Model Dev.*, *5*(3), 709–739.

Liu, Y., and P. Daum (2004), Parameterization of the autoconversion process. part i: Analytical formulation of the kessler-type parameterizations, *J. Atmos. Sci.*, *61*, 1539–1548.

Liu, Y., and P. Daum (2005), Parameterization of the autoconversion process. part 1: Analytical formulation of the kessler-type parameterizations - reply, *J. Atmos. Sci.*, *62*, 3007–3008.

Liu, Y., P. Daum, R. McGraw, et al. (2006a), Parameterization of the autoconversion process. part ii: Generalization of Sundqvist-type parameterizations, *J. Atmos. Sci.*, *63*, 1103–1109.

Liu, Y., P. Daum, and S. S. Yum (2006b), Analytical expression for the relative dispersion of the cloud droplet size distribution, *Geophys. Res. Lett.*, *33*, L02,810, doi:101029/2005GL024052.

Liu, Y., P. Daum, H. Guo, and Y. Peng (2008), Dispersion bias, dispersion effect, and the aerosol-cloud conundrum, *Environ. Res. Lett.*, *3*, 045,021, doi:10.1088/1748-9326/3/4/045021.

Lohmann, U. (2002), Possible aerosol effects on ice clouds via contact nucleation, *J. Atmos. Sci.*, *59*, 647–656.

Lohmann, U. (2008), Global anthropogenic aerosol effects on convective clouds in ECHAM5-HAM, *Atmos. Chem. Phys.*, *8*, 2115–2131.

Lohmann, U., and K. Diehl (2005), Sensitivity studies of the importance of dust ice nuclei for the indirect aerosol effect on stratiform mixed-phase clouds, *J. Atmos. Sci.*, *63*, 968–982.

Lohmann, U., and J. Feichter (2005), Global indirect aerosol effects: A review, *Atmos. Chem. Phys.*, *5*, 715–737.

Lohmann, U., J. Feitcher, C. C. Chuang, and J. E. Penner (1999), Prediction of the number of cloud droplets in the ECHAM GCM, *J. Geophys. Res.*, *104*, 9169–9198.

Lohmann, U., P. Stier, C. Hoose, S. Ferrachat, S. Kloster, E. Roeckner, and J. Zhang (2007), Cloud microphysics and aerosol indirect effects in the global climate model ECHAM5-HAM, *Atmos. Chem. Phys.*, *7*, 3425–3446, doi: 10.5194/acp-7-3425-2007.

Lu, M.-L., W. Conant, H. H. Jonsson, V. Varutbangkul, R. Flagan, and J. H. Seinfeld (2007), The marine stratus/stratocumulus experiment (MASE): Aerosol-cloud relationships in marine stratocumulus, *J. Geophys. Res.*, *112*, D10,209, doi:10.1029/2006JD007985.

Lu, M.-L., G. Feingold, H. H. Jonsson, P. Y. Chuang, H. Gates, R. Flagan, and J. H. Seinfeld (2008), Aerosol-cloud relationships in continental shallow cumulus, *J. Geophys. Res.*, *113*, D15,201, doi:10.1029/2007JD009354.

Malik, H. H. (1967), Exact distribution of the quotient of independent generalized gamma variables, *Canad. Math. Bull.*, *10*, 463–465.

May, P. T., J. H. Mather, G. Vaughan, and C. Jakob (2008), Field research: Characterizing oceanic convective cloud systems, *Bull. Am. Meteorol.*, *89*, 153–155, doi:10.1175/BAMS-89-2-153.

McFiggans, G., P. Artaxo, U. Baltensperger, H. Coe, M. C. Facchini, G. Feingold, S. Fuzzi, M. Gysel, A. Laaksonen, U. Lohmann, T. F. Mentel, D. M. Murphy, C. D. O'Dowd, J. R. Snider, and E. Weingartner (2006), The effect of physical and chemical aerosol properties on warm cloud droplet activation, *Atmos. Chem. Phys.*, *6*(9), 2593–2649.

Medina, J., A. Nenes, R.-E. P. Sotiropoulou, L. D. Cottrell, L. D. Ziemba, P. J. Beckman, and R. J. Griffin (2007), Cloud condensation nuclei closure during the International Consortium for Atmospheric Research on Transport and Transformation 2004 campaign: Effects of size-resolved composition, *J. Geophys. Res.*, *112*(D10).

Meskhidze, N., A. Nenes, W. C. Conant, and J. H. Seinfeld (2005), Evaluation of a new cloud droplet activation parameterization with in situ data from CRYSTAL-FACE and CSTRIPE, *J. Geophys. Res.*, *110*, D16,202, doi: 10.1029/2004JD005703.

Meyers, M., P. J. DeMott, and W. R. Cotton (1992), New primary ice-nucleation parameterizations in an explicit cloud model, *J. Appl. Met.*, *31*, 708–721.

Ming, Y., V. Ramaswamy, L. J. Donner, and V. T. J. Phillips (2006), A new parameterization of cloud droplet activation applicable to general circulation models, *J. Atmos. Sci.*, *63*, 1348–1356.

Minikin, A., A. Petzold, J. Ström, R. Krejci, M. Seifert, P. Veltoven, H. Schlager, and U. Schumann (2003), Aircraft observations of the upper tropospheric fine particle aerosol in the Northern and Southern Hemispheres at midlatitudes, *Geophys. Res. Lett.*, *30*(10), 1503–1506, doi:10.1029/2002GL016458.

Moore, R. H., R. Bahreini, C. A. Brock, K. D. Froyd, J. Cozic, J. S. Holloway, A. M. Middlebrook, D. M. Murphy, and A. Nenes (2011), Hygroscopicity and composition of Alaskan Arctic CCN during April 2008, *Atmos. Chem. Phys.*, *11*(22), 11,807–11,825.

Moore, R. H., K. Cerully, R. Bahreini, C. A. Brock, A. M. Middlebrook, and A. Nenes (2012a), Hygroscopicity and composition of California CCN during summer 2010, *J. Geophys. Res.*, *117*(D21).

Moore, R. H., T. Raatikainen, J. M. Langridge, R. Bahreini, C. A. Brock, J. S. Holloway, D. A. Lack, A. M. Middlebrook, A. E. Perring, J. Schwarz, J. R. Spackman, and A. Nenes (2012b), CCN spectra, hygroscopicity, and droplet activation kinetics of secondary organic aerosol resulting from the 2010 Deepwater Horizon oil spill, *Environ. Sci. Technol.*, *46*(6), 3093–3100, doi:10.1021/es203362w.

Morales, R., and A. Nenes (2010), Characteristic updrafts for computing distribution-averaged cloud droplet number, autoconversion rate and effective radius, *J. Geophys. Res.*, *115*, D18,220, doi:10.1029/2009JD013233.

Morales, R., and A. Nenes (In preparation), Aerosol activation parameterization: the population splitting concept revisited, *Geosci. Model Dev.*

Morales, R., and A. Nenes (Submitted), Adjoint sensitivity study of aerosol activation parameterizations in a gcm, *Atmos. Chem. Phys. Discuss.*

Morales, R., A. Nenes, H. Jonsson, R. C. Flagan, and J. H. Seinfeld (2011), Evaluation of an entraining droplet activation parameterization using in situ cloud data, *J. Geophys. Res.*, *116*, D15205, doi:10.1029/2010JD015324.

Morales, R., D. Lee, L. Oreopoulos, Y. C. Sud, D. Barahona, and A. Nenes (2012), Sensitivity of cirrus and mixed-phase clouds to the ice nuclei spectra in McRAS-AC: single column model simulations, *Atmos. Chem. Phys.*, *12*, 10,679–10,692, doi:10.5194/acp-12-10679-2012.

Morrison, H., and A. Gettelman (2008), A new two-moment bulk stratiform cloud microphysics scheme in the Community Atmosphere Model, Version 3 (CAM3). Part I: Description and numerical tests, *J. Climate*, *21*, 3642–3659, doi:10.1175/2008JCLI2105.1.

Mozurkewich, M. (2008), Aerosol growth and the condensation coefficient for water: A review, *Aerosol Sci. Technol.*

Muhlbauer, A., and U. Lohmann (2009), Sensitivity studies of aerosol–cloud interactions in mixed-phase orographic precipitation, *J. Atmos. Sci.*, *66*, 2517–2538, doi:10.1175/2009JAS3001.1.

Myhre, G., B. H. Samset, M. Schulz, Y. Balkanski, S. Bauer, T. K. Berntsen, H. Bian, N. Bellouin, M. Chin, T. Diehl, R. C. Easter, J. Feichter, S. J. Ghan, D. Hauglustaine, T. Iversen, S. Kinne, A. Kirkevåg, J.-F. Lamarque, G. Lin, X. Liu, M. T. Lund, G. Luo, X. Ma, T. van Noije, J. E. Penner, P. J. Rasch, A. Ruiz, Ø. Seland, R. B. Skeie, P. Stier, T. Takemura, K. Tsigaridis, P. Wang, Z. Wang, L. Xu, H. Yu, F. Yu, J.-H. Yoon, K. Zhang, H. Zhang, and C. Zhou (2013), Radiative forcing of the direct aerosol effect from AeroCom Phase II simulations, *Atmos. Chem. Phys.*, *13*(4), 1853–1877.

Nenes, A., and J. H. Seinfeld (2003), Parameterization of cloud droplet formation in global climate models, *J. Geophys. Res.*, *108*(D14), 4415, doi:10.1029/2002JD002911.

Nenes, A., S. Ghan, H. Abdul-Razzak, P. Y. Chuang, and J. H. Seinfeld (2001), Kinetic limitations on cloud droplet formation and impact on cloud albedo, *Tellus*, *53B*, 133–149.

Niedermeier, D., S. Hartmann, R. A. Shaw, D. Covert, T. F. Mentel, J. Schneider, L. Poulain, P. Reitz, C. Spindler, T. Clauss, A. Kiselev, E. Hallbauer, H. Wex, K. Mildenberger, and F. Stratmann (2010), Heterogeneous freezing of droplets with immersed mineral dust particles – measurements and parameterization, *Atmos. Chem. Phys.*, *10*, 3601–3614.

Novakov, T., and J. E. Penner (1993), Large contribution of organic aerosols to cloud-condensation-nuclei concentrations, *Nature*, *365*(6449), 823–826, doi:10.1038/365823a0.

Padró, L. T., R. H. Moore, X. Zhang, N. Rastogi, R. J. Weber, and A. Nenes (2012), Mixing state and compositional effects on ccn activity and droplet growth kinetics of size-resolved ccn in an urban environment, *Atmos. Chem. Phys.*, *12*(21), 10,239–10,255.

Peng, Y., U. Lohmann, R. Leaitch, C. Banic, and M. Couture (2002), The cloud albedo-cloud droplet effective radius relationship for clean and polluted clouds from RACE and FIRE.ACE, *J. Geophys. Res.*, *107*, D114,106, doi: 10.1029/2000JD000281.

Peng, Y., U. Lohmann, and R. Leaitch (2005), Importance of vertical velocity variations in the cloud droplet nucleation process of marine stratus clouds, *J. Geophys. Res.*, *110*, D21,213, doi:10.1029/2004JD004922.

Penner, J. E., J. Quaas, T. Storelvmo, T. Takemura, O. Boucher, H. Guo, A. Kirkevag, J. E. Kristjánsson, and O. Seland (2006), Model intercomparison of indirect aerosol effects, *Atmos. Chem. Phys.*, *6*, 3391–3405.

Petters, M. D., and S. M. Kreidenweis (2007), A single parameter representation of hygroscopic growth and cloud condensation nucleus activity, *Atmos. Chem. Phys.*, *7*(8), 1961–1971.

Phillips, V. T. J., L. J. Donner, and S. T. Garner (2007), Nucleation processes in deep convection simulated by a cloud-system-resolving model with double-moment bulk microphysics, *J. Atmos. Sci.*, *64*, 738–761, doi:10.1175/JAS3869.1.

Phillips, V. T. J., P. J. DeMott, and C. Andronache (2008), An empirical parameterization of heterogeneous ice nucleation for multiple chemical species of aerosol, *J. Atmos. Sci.*, *65*, 2757–2783, doi:10.1175/2007JAS2546.1.

Pierce, J. R., and P. J. Adams (2009), Uncertainty in global ccn concentrations from uncertain aerosol nucleation and primary emission rates, *Atmospheric Chemistry and Physics*, *9*(4), 1339–1356.

Pierce, J. R., K. Chen, and P. J. Adams (2007), Contribution of primary carbonaceous aerosol to cloud condensation nuclei: processes and uncertainties evaluated with a global aerosol microphysics model, *Atmos. Chem. Phys.*, *7*(20), 5447–5466.

Pincus, R., and S. A. Klein (2000), Unresolved spatial variability and microphysical process rates in large-scale models, *J. Geophys. Res.*, *105*, 27,059 – 27,065.

Pincus, R., S. A. McFarlane, and S. A. Klein (1999), Albedo bias and the horizontal variability of clouds in subtropical marine boundary layers: Observations from ships and satellites, *J. Geophys. Res.*, *104*(D6), 6183–6191.

Pincus, R., H. W. Barker, and J.-J. Morcrette (2003), A fast, flexible, approximate technique for computing radiative transfer in inhomogeneous cloud fields, *J. Geophys. Res.*, *108*(D13), doi:10.1029/2002JD003322.

Pinsky, M., A. Khain, I. Mazin, and A. Korolev (2012), Analytical estimation of droplet concentration at cloud base, *J. Geophys. Res.*, *117*(D18), n/a–n/a, doi: 10.1029/2012JD017753.

Pringle, K. J., K. S. Carslaw, D. V. Spracklen, G. M. Mann, and M. P. Chipperfield (2009), The relationship between aerosol and cloud drop number concentrations in a global microphysics model, *Atmos. Chem. Phys.*, *9*, 4131–4144.

Pruppacher, H., and J. Klett (1997), *Microphysics of clouds and precipitation*, Atmospheric and oceanographic sciences library, 2nd rev, and enl ed., Kluwer Academic Publishers.

Pueschel, R. F., G. V. Ferry, K. G. Snetsinger, J. Goodman, J. E. Dye, D. Baumgardner, and B. W. Gandrud (1992), A case of Type I polar stratospheric cloud formation by heterogeneous nucleation, *J. Geophys. Res.*, *9*, 8105–8114, doi:10.1029/91JD02352.

Quaas, J., Y. Ming, S. Menon, T. Takemura, M. Wang, J. E. Penner, A. Gettelman, U. Lohmann, N. Bellouin, O. Boucher, A. M. Sayer, G. E. Thomas, A. McComiskey, G. Feingold, C. Hoose, J. E. Kristjánsson, X. Liu, Y. Balkanski, L. J. Donner, P. A. Ginoux, P. Stier, B. Grandey, J. Feichter, I. Sednev, S. E. Bauer, D. Koch, R. G. Grainger, A. Kirkevåring;g, T. Iversen, Ø. Seland, R. Easter, S. J. Ghan, P. J. Rasch, H. Morrison, J.-F. Lamarque, M. J. Iacono, S. Kinne, and M. Schulz (2009), Aerosol indirect effects – general circulation model intercomparison and evaluation with satellite data, *Atmospheric Chemistry and Physics*, *9*(22), 8697–8717.

Raatikainen, T., R. H. Moore, T. L. Lathem, and A. Nenes (2012), A coupled observation–modeling approach for studying activation kinetics from measurements of CCN activity, *Atmos. Chem. Phys.*, *12*(9), 4227–4243.

Raatikainen, T., A. Nenes, J. H. Seinfeld, R. Morales, R. H. Moore, T. L. Lathem, S. Lance, L. T. Padro, J. J. Lin, K. M. Cerully, A. Bougiatioti, J. Cozic, C. R. Ruehl, P. Y. Chuang, B. E. Anderson, R. C. Flagan, H. Jonsson, N. Mihalopoulos, and J. N. Smith (2013), Worldwide data sets constrain the water vapor uptake coefficient in cloud formation, *Proc. Nat. Acad. Sci.*, *110*, 3760–3764, doi:10.1073/pnas.1219591110.

Rasch, P. J., and J. E. Kristjánsson (1998), A comparison of the CCM3 model climate using diagnosed and predicted condensate parameterizations, *J. Climate*, *11*, 1587–1614.

Reutter, P., H. Su, J. Trentmann, M. Simmel, D. Rose, S. S. Gunthe, H. Wernli, M. O. Andreae, and U. Pöschl (2009), Aerosol- and updraft-limited regimes of cloud droplet formation: influence of particle number, size and hygroscopicity on the activation of cloud condensation nuclei (CCN), *Atmos. Chem. Phys.*, *9*(18), 7067–7080, doi:10.5194/acp-9-7067-2009.

Rissman, T. A., A. Nenes, and J. H. Seinfeld (2004), Chemical amplification (dampening) of the Twomey effect: Conditions derived from droplet activation, *J. Atmos. Sci.*, *61*, 919–930.

Rotstayn, L., B. Ryan, and J. Katzfey (2000), A scheme for calculation of the liquid fraction in mixed-phase stratiform clouds in large-scale models, *Monthly Weather Rev.*, *128*, 1070–1088.

Rotstayn, L. D. (1997), A physically based scheme for the treatment of stratiform precipitation in large-scale models. I: Description and evaluation of the microphysical processes, *Q. J. R. Meteorol. Soc.*, *123*, 1227–1282.

Rotstayn, L. D. (2000), On the “tuning” of autoconversion parameterizations in climate models, *J. Geophys. Res.*, *105*, 15,495–15,507.

Ruehl, C. R., P. Y. Chuang, and A. Nenes (), Distinct ccn activation kinetics above the marine boundary layer along the california coast, *Geophysical Research Letters*, *36*(15).

Ruehl, C. R., P. Y. Chuang, and A. Nenes (2008), How quickly do cloud droplets form on atmospheric particles?, *Atmos. Chem. Phys.*, *8*(4), 1043–1055.

Saide, P. E., G. R. Carmichael, S. N. Spak, P. Minnis, and J. K. Ayers (2012), Improving aerosol distributions below clouds by assimilating satellite-retrieved cloud droplet number, *Proc. Nat. Acad. Sci.*, doi: 10.1073/pnas.1205877109.

Salzmann, M., Y. Ming, J.-C. Golaz, P. A. Ginoux, H. Morrison, A. Gettelman, M. Kramer, and L. J. Donner (2010), Two-moment bulk stratiform cloud microphysics in the GFDL AM3 GCM: description, evaluation, and sensitivity tests, *Atmos. Chem. Phys.*, *10*, 8037–8064, doi:10.5194/acp-10-8037-2010.

Seifert, A., and K. D. Beheng (2001), A double-moment parameterization for simulating autoconversion, accretion and selfcollection, *Meteorol. Atmos. Phys.*, *59*, 265–281.

Seifert, A., and K. D. Beheng (2006), A two-moment cloud microphysics parameterization for mixed-phase clouds. Part 1: Model description, *Meteorol. Atmos. Phys.*, *92*, 45–66, doi:10.1007/s00703-005-0112-4.

Seinfeld, J., and S. Pandis (2006), *Atmospheric chemistry and physics: from air pollution to climate change*, A Wiley-Interscienciе publications, Wiley.

Shipway, B., and S. Abel (2010), Analytical estimation of cloud droplet nucleation based on an underlying aerosol population, *Atmospheric Research*, *96*(23), 344 – 355, doi:10.1016/j.atmosres.2009.10.005.

Small, J. D., P. Chuang, G. Feingold, and H. Jiang (2009), Can aerosol decrease cloud lifetime?, *Geophys. Res. Lett.*, *36*(L16806), doi: 10.1029/2009GL038888.

Sotiropoulou, R. E. P., A. Nenes, P. J. Adams, and J. H. Seinfeld (2007), Cloud condensation nuclei prediction error from application of Köhler theory: Importance for the aerosol indirect effect, *J. Geophys. Res.*, *112*, D12,202, doi: 10.1029/2006JD007834.

Stacy, E. W. (1962), A generalization of the gamma distribution, *Ann. Math. Stat.*, *33*(3), 1187–1192.

Stevens, B., and G. Feingold (2009), Untangling aerosol effects on clouds and precipitation in a buffered system, *Nature*, *461*, 607–613, doi:1038/nature08281.

Stier, P., J. Feichter, S. Kinne, S. Kloster, E. Vignati, J. Wilson, L. Ganzeveld, I. Tegen, M. Werner, Y. Balkanski, M. Schulz, O. Boucher, A. Minikin, and A. Petzold (2005), The aerosol-climate model ECHAM5-HAM, *Atmospheric Chemistry and Physics*, *5*(4), 1125–1156.

Storelvmo, T., J. E. Kristjánsson, and U. Lohmann (2008), Aerosol influence on mixed-phase clouds in CAM-Oslo, *J. Atmos. Sci.*, *65*, 3214–3230, doi: 10.1175/2008JAS2430.1.

Sud, Y. C., and D. Lee (2007), Parameterization of aerosol indirect effect to complement McRAS cloud scheme and its evaluation with the 3-year ARM-SGP analyzed data for single column models, *Atmos. Res.*, *86*, 105–125.

Sud, Y. C., and G. K. Walker (1999), Microphysics of clouds with the Relaxed Arakawa–Schubert scheme (McRAS). Part I: Design and evaluation with GATE phase III data, *J. Atmos. Sci.*, *56*, 3196–3220, doi:10.1029/2008GL036817.

Sundqvist, H. (1978), A parameterization scheme for non-convective condensation including prediction of cloud water content, *Q. J. R. Meteorol. Soc.*, *104*, 677–690.

Tiedtke, M. (1989), A comprehensive mass flux scheme for cumulus parameterization in large-scale models, *Monthly Weather Rev.*, *117*, 1779–1800.

Tompkins, A. M. (2001), A prognostic parameterization for the subgrid-scale variability of water vapor and clouds in large-scale models and its use to diagnose cloud cover, *J. Atmos. Sci.*, *59*(12), 1917–1942.

Tonttila, J., P. Räisänen, and H. Järvinen (2013), Monte carlo-based subgrid parameterization of vertical velocity and stratiform cloud microphysics in ECHAM5.5-HAM2, *Atmos. Chem. Phys.*, *13*(15), 7551–7565.

Trivitayanurak, W., and P. J. Adams (2013), Does the POA-SOA split matter for global ccn formation?, *Atmospheric Chemistry and Physics Discussions*, *13*(4), 10,561–10,601.

Twomey, S. (1959), The nuclei of natural cloud formation. part II: The supersaturation in natural clouds and the variation of cloud droplet concentration, *Geof. Pura Appl.*, *43*, 243–249.

Twomey, S. (1974), Pollution and the planetary albedo, *Atmos. Environ.*, *8*, 1251–1256.

Twomey, S. (1977), The influence of pollution on the shortwave cloud albedo of clouds, *J. Atmos. Sci.*, *34*, 1149–1152.

Twomey, S., and T. A. Wojciechowski (1968), Observations of the geographical variation of cloud nuclei, *J. Atmos. Sci.*, *26*, 684–688.

van Diedenhoven, B., A. Fridlind, A. Ackerman, and B. Cairns (2012), Evaluation of hydrometeor phase and ice properties in cloud-resolving model simulations of tropical deep convection using radiance and polarization measurements, *J. Atmos. Sci.*, *69*, 3290–3314, doi:10.1175/JAS-D-11-0314.1.

VanReken, T., T. A. Rissman, G. Roberts, V. Varutbangkul, H. Jonsson, R. Flagan, and J. Seinfeld (2003), Toward aerosol/cloud condensation nuclei (CCN) closure during CRYSTAL-FACE, *J. Geophys. Res.*, *108*(D20), 4633, doi:10.1029/2003JD003582.

Varble, A., A. M. Fridlind, E. J. Zipser, A. S. Ackerman, J.-P. Chaboureau, J. Fan, A. Hill, S. A. McFarlane, J.-P. Pinty, and B. Shipway (2011), Evaluation of cloud-resolving model intercomparison simulations using TWP - ICE observations: Precipitation and cloud structure, *J. Geophys. Res.*, *116*, D12206, doi:10.1029/2010JD015180.

Wang, M., S. Ghan, M. Ovchinnikov, X. Liu, R. Easter, E. Kassianov, Y. Qian, and H. Morrison (2011), Aerosol indirect effects in a multi-scale aerosol-climate model PNNL-MMF, *Atmos. Chem. Phys.*, *11*(11), 5431–5455, doi:10.5194/acp-11-5431-2011.

Wang, W., X. Liu, S. Xie, J. Boyle, and S. A. McFarlane (2009a), Testing ice microphysics parameterizations in the NCAR Community Atmospheric Model Version 3 using Tropical Warm Pool International Cloud Experiment data, *J. Geophys. Res.*, *114*, D14107, doi:10.1029/2008JD011220.

Wang, Y., C. Long, L. Leung, J. Dudhia, S. McFarlane, J. Mather, S. J. Ghan, and X. Liu (2009b), Evaluating regional cloud-permitting simulations of the WRF model for the Tropical Warm Pool International Cloud Experiment (TWP-ICE), Darwin, 2006, *J. Geophys. Res.*, *114*, D21203, doi:10.1029/2009JD012729.

Warner, J. (1970), On steady-state one-dimensional models of cumulus convection, *J. Atmos. Sci.*, *27*, 1035– 1040.

Warner, J. (1973), Microstructure of cumulus clouds: Part IV: The effect on the droplet spectrum of mixing between cloud and environment, *J. Atmos. Sci.*, *30*, 256–261.

West, R. E. L., P. Stier, A. Jones, C. E. Johnson, G. W. Mann, N. Bellouin, and Z. Kipling (2013), The importance of vertical velocity variability for estimates of the indirect aerosol effects, *Atmos. Chem. Phys. Discuss.*, *13*(10), 27,053–27,113.

Whitby, K. T. (1978), The physical characteristics of sulfur aerosols, *Atmos. Env.*, *12*, 135–139.

Whitby, K. T. (2005), Comments on “Parameterization of the autoconversion process. Part I: Analytical formulation of the Kessler-type parameterizations”, *J. Atmos. Sci.*, *62*, 3003–3006.

Y.G., L., and P. Daum (2005), Anthropogenic aerosols - indirect warming effect from dispersion forcing, *Nature*, *419*, 580–581.

Young, K. C. (1974), The role of contact nucleation in ice phase initiation in clouds, *J. Atmos. Sci.*, *31*, 768–776.

Yu, F., and G. Luo (2009), Simulation of particle size distribution with a global aerosol model: contribution of nucleation to aerosol and ccn number concentrations, *Atmos. Chem. Phys.*, *9*(20), 7691–7710.

Zhao, C., X. Liu, Y. Qian, J. Yoon, Z. Hou, G. Lin, S. McFarlane, H. Wang, B. Yang, P.-L. Ma, H. Yan, and J. Bao (2013), A sensitivity study of radiative fluxes at the top of atmosphere to cloud-microphysics and aerosol parameters in the Community Atmosphere Model CAM5, *Atmos. Chem. Phys. Discuss.*, *13*(5), 12,135–12,176.

Zhu, P., and P. Zuidema (2009), On the use of PDF schemes to parameterize sub-grid clouds, *Geophys. Res. Lett.*, *36*, L05,807, doi:10.1029/2008GL036817.